Proton-Coupled Electron Transfer Reactivity of Ruthenium Complexes with Separation Between the Proton and Electron Transfer Sites

Jessica M. Wittman

A dissertation submitted in partial fulfillment
of the requirements for the degree of

Doctor of Philosophy

University of Washington

2014

Program Authorized to Offer Degree: Department of Chemistry

University of Washington

Abstract

Proton-Coupled Electron Transfer Reactivity of Ruthenium Complexes with Separation Between the Proton and Electron Transfer Sites

Jessica M. Wittman

Chair of the Supervisory Committee:
Professor James M. Mayer
Chemistry

Proton-coupled electron transfer (PCET) events are essential to the function of many processes. In many cases, long-range electron transfers (ET) are coupled to short-range proton transfer (PT) events. Ruthenium bipyridine complexes with a distant carboxylic acid have been synthesized and characterized to study the effect of varying distances between the PT and ET sites on PCET reactions. In reactions with hydrogen atom acceptors, an electron is transferred from the ruthenium center while proton transfer occurs at the distant carboxylic acid. A phenyl spacer can be incorporated into the bipyridine ligand to provide further separation between the ET and PT sites. The results of kinetic experiments allow analysis of the effects of the distance between ET and PT sites on the PCET reactions.

TABLE OF CONTENTS

LIST OF FIGURES

LIST OF TABLES

ACKNOWLEDGEMENTS

First, I want to thank my advisor, Jim Mayer, for making me a better scientist and a stronger person. I also want to thank all the professor who helped me get to graduate school at the University of Washington, including Mary Cloninger, Steve Holmgren, Robert Szilagyi, Trevor Douglas, and Travis Bailey. I want to particularly thank Adam Veige who first introduced me to synthetic inorganic chemistry and recommended the inorganic division at University of Washington for graduate school. I also must thank my first high school chemistry teacher, Mr. Kusterer, for making chemistry so interesting. I hope I can teach like him someday! I have had the opportunity to work with some greatly intelligent and really cool PCET chemists while I've been here including Tristan Tronic, Jeff Warren, Elizabeth Mader, Todd Markle, and Ian Rhile.

I have so many friends to thank who have helped me get through this process, and I am excited to have more time to spend with them now that I have made it through. I learned so much from working with Alex and Colin in the dark side lab, but most importantly, I made two life long friends. My other dark side lab cohort was Carlos, and I'm glad I ended up getting to know him, as he was a great ally. I've also been lucky to have Miles around for most of my time in the Mayer lab, and he is always there to listen and help me get through everything. Thanks to Mike for providing a new perspective from a non-scientist when I needed it. Thanks to Sophia for being an endless source of entertainment, laughter, and good advice about chemistry and life. Thanks to Sarah for being a supportive friend and for all of the things she's doing to make graduate school a better place for everyone. Thanks to Marie for always being nearby at school and for letting me use her equipment when my lab was packed up. I'm so glad I entered grad school with Carrie, Megan, and Sam. Thanks to Bradley for sticking through the worst times, especially the very worst weekend near the end of the whole process. What a fine crew to have through this whole process! Thank you forever and ever to Alesha for moving out here and keeping me grounded. I don't know what I would have done without her. Also thanks for convincing me to get a cat and driving me to pick up my dearest Bill Furray. Finally, thank you to my family, who always said I could quit any time, but also gave me the necessary support and encouragement to finish.

DEDICATION

For the other doctor in my family, Dr. Beat.

Chapter 1

Introduction to Proton-Coupled Electron Transfer with Distance Dependence

1.1 Introduction to Proton-Coupled Electron Transfer

Proton-coupled electron transfers (PCET) are essential and fundamental steps in many important reactions, from industrial scale chemical transformations to chemical processes occurring in biological systems.[1] These PCET reactions are often the energetically favored mechanism because they avoid the formation of high-energy, charge-separated intermediates. The oxidation of water, for example, requires the loss of 4 electrons (e^-) and 4 protons (H^+) to form oxygen (Scheme 1.1). In order to achieve efficient oxidation of water, sequential PCET steps that avoid charge separation are essential. Plants accomplish this through photosynthesis, and PCET reactions have been identified as many of the elementary steps involved in the water oxidation pathway in photosynthesis.[2-4]

1.2 Sequential Versus Concerted PCET Mechanisms

The transfer of a single proton and a single electron from one molecule to another can proceed by one of three pathways (Scheme 1.2). There are two stepwise PCET pathways involving the sequential transfer of the proton and the electron. A mechanism in which a proton transfer is

Scheme 1.1. Oxidation of water to form oxygen.

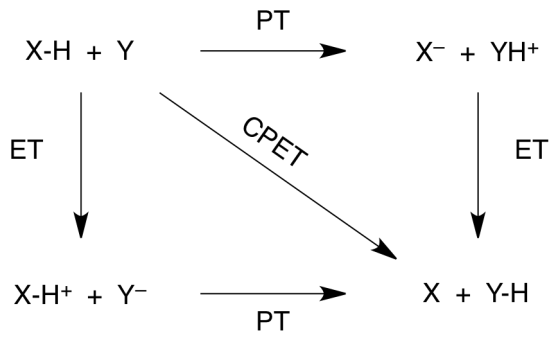

Scheme 1.2. Possible PCET pathways for the transfer of one proton and one electron from X to Y.

followed by an electron transfer will be referred to as initial PT, and a mechanism in which an electron transfer is followed by a proton transfer will be referred to as initial ET. Alternatively, the proton and an electron can also transfer in a single kinetic step. This PCET mechanism is often called concerted proton-electron transfer (CPET), and will be referred to as such herein.[5] The CPET mechanism avoids formation of the charged intermediates that are present in the initial PT and initial ET mechanisms.

1.3 PT and ET Site Distance Dependence

Another important dimension of PCET mechanisms is the distance between the sites at which PT and ET occur. Electron transfers can occur over a wide range of distances, while protons transfer over much shorter distances.[6-11] This leads to large variations in the distance between the PT and ET sites. PCET reactions involving hydrogen atom ($H^{\bullet} \equiv H^{+} + e^{-}$) donors and acceptors with a wide range of distances between the PT and ET sites have been studied.[12-17] A simple example with no separation can be seen in the reaction between methane and methyl radical depicted in Scheme 1.3, where PT and ET occur at the same site on the donor and acceptor molecules, and a "hydrogen atom" is formally transferred. Alternatively, in a number of PCET

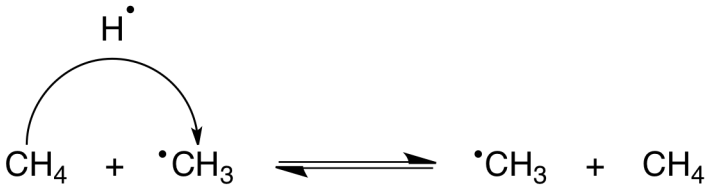

Scheme 1.3. Self-exchange PCET reaction of methane and methyl radical.

reactions, the long-distance ET is coupled to short-distance PT. For example, the ability of proteins to regulate proton transfer (PT) in conjunction with long-range electron transfer (ET) may be important in ribonucleotide reductase[18,19] and photosystem II.[2-4] In photosystem II, an electron is transferred over a distance of 14 Å from a tyrosine residue to the chlorophyll radical cation $P_{680}^{\bullet+}$, while a proton is transferred from the tyrosine to a nearby histidine residue.[3,20]

While CPET mechanisms have been studied extensively with organic systems, where the proton and electron transfer in a single kinetic step, many metal complexes show CPET reactivity as well.[21-26] In CPET reactions with metal complexes, the electron transfer often occurs to or from the metal center, while the proton transfer occurs to or from a ligand with an acid/base site. This introduces separation between the PT and ET sites that varies for complexes with

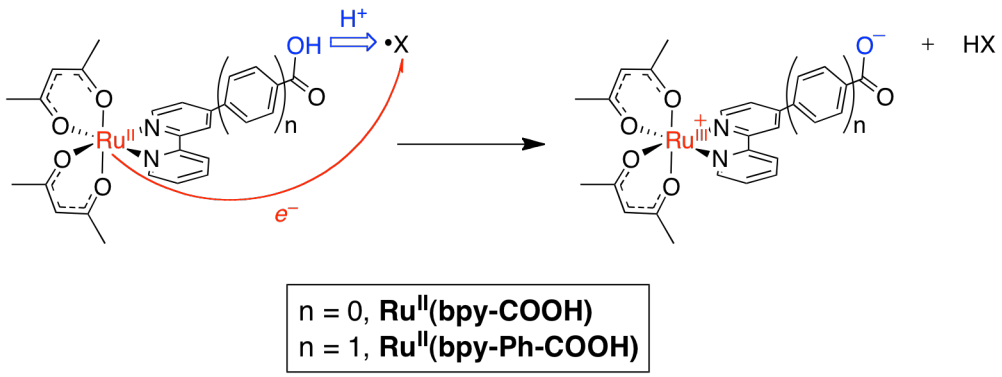

Figure 1.1. PCET reaction of $Ru^{II}(acac)_2$(bpy-COOH) or $Ru^{II}(acac)_2$(bpy-Ph-COOH) with a hydrogen atom acceptor, $X^{\bullet}$.

different ligand environments. The ruthenium bipyridine-carboxylate complexes shown in Figure 1.1 were synthesized to study the effect of this separation on PCET reactivity. In the reaction in Figure 1.1, a hydrogen atom acceptor ($X^{\bullet}$) accepts an electron from the ruthenium center and a proton from the carboxylic acid group of the bipyridine ligand. Variation in the separation between the ET and PT sites was achieved by incorporating a phenyl spacer into the bipyridine-carboxylate ligand. The synthesis, characterization, and PCET reactivity of these complexes are described in Chapters 2 and 3.

Notes to Chapter 1

(1) (a) "Free Radicals," Kochi, J. K., Ed.; Wiley: New York: 1973. (b) Hydrogen-Transfer Reactions Hynes, J. T.; Klinman, J. P.; Limbach, H.-H., Schowen, R. L., Eds.; Wiley–VCH: Weinheim: 2007. (c) Mayer, J. M. *Annu. Rev. Phys. Chem.* **2004**, *55*, 363–390. (d) Huynh, M. H. V.; Meyer, T. J. *Chem. Rev.* **2007**, *107*, 5004-5064. (e) Mayer, J. M. *Acc. Chem. Res.* **1998**, *31*, 441-450.

(2) Meyer, T. J.; Huynh, M. H. V.; Thorp, H. H. *Angew Chem Int Edit* **2007**, *46*, 5284-5304.

(3) Keough, J. M.; Jenson, D. L.; Zuniga, A. N.; Barry, B. A. *J. Am. Chem. Soc.* **2011**, *133*, 11084-11087.

(4) Dempsey, J. L.; Winkler, J. R.; Gray, H. B. *Chem. Rev.* **2010**, *110*, 7024-7039.

(5) Costentin, C.; Evans, D.; Robert, M.; Saveant, J.; Singh, P. *J. Am. Chem. Soc.* **2005**, *127*, 12490-12491.

(6) Closs, G. L.; Miller, J. R. *Science* **1988**, *240*, 440-447.

(7) Mclendon, G. *Acc. Chem. Res.* **1988**, *21*, 160-167.

(8) Gray, H. B. *Abstr. Pap. Am. Chem. Soc.* **1988**, *195*, 274.

(9) Gray, H. B.; Winkler, J. R. *Annu. Rev. Biochem.* **1996**, *65*, 537-561.

(10) Edwards, P. P.; Gray, H. B.; Lodge, M. T. J.; Williams, R. J. P. *Angewandte Chemie-International Edition* **2008**, *47*, 6758-6765.

(11) Bell, R. P. *The Proton in Chemistry*; 2nd ed.; Chapman and Hall: London, 1973.

(12) Manner, V. W.; DiPasquale, A. G.; Mayer, J. M. *J. Am. Chem. Soc.* **2008**, *130*, 7210-7211.

(13) Manner, V. W.; Mayer, J. M. *J. Am. Chem. Soc.* **2009**, *131*, 9874-9875.

(14) Markle, T. F.; Rhile, I. J.; Mayer, J. M. *J. Am. Chem. Soc.* **2011**, *133*, 17341-17352.

(15) Waidmann, C. R.; DiPasquale, A. G.; Mayer, J. M. *Inorg. Chem.* **2010**, *49*, 2383-2391.

(16) Wu, A.; Mayer, J. M. *J. Am. Chem. Soc.* **2008**, *130*, 14745-14754.

(17) Warren, J. J.; Mayer, J. M. *J. Am. Chem. Soc.* **2011**, *133*, 8544-8551.

(18) Stubbe, J.; Nocera, D.; Yee, C.; Chang, M. *Chem. Rev.* **2003**, *103*, 2167-2201.

(19) Yokoyama, K.; Smith, A. A.; Corzilius, B.; Griffin, R. G.; Stubbe, J. *J. Am. Chem. Soc.* **2011**, *133*, 18420-18432.

(20) Umena, Y.; Kawakami, K.; Shen, J. R.; Kamiya, N. *Nature* **2011**, *473*, 55-65.

(21) Mader, E.; Larsen, A.; Mayer, J. *J. Am. Chem. Soc.* **2004**, *126*, 8066-8067.

(22) Mader, E. A.; Davidson, E. R.; Mayer, J. M. *J. Am. Chem. Soc.* **2007**, *129*, 5153-5166.

(23) Roth, J.; Lovell, S.; Mayer, J. *J. Am. Chem. Soc.* **2000**, *122*, 5486-5498.

(24) Roth, J.; Mayer, J. *Inorg. Chem.* **1999**, *38*, 2760-2761.

(25) Warren, J. J.; Mayer, J. M. *J. Am. Chem. Soc.* **2008**, *130*, 2774-2776.

(26) Wu, A.; Masland, J.; Swartz, R. D.; Kaminsky, W.; Mayer, J. M. *Inorg. Chem.* **2007**, *46*, 11190-11201.

Chapter 2

Proton-Coupled Electron Transfer Thermochemistry of Ruthenium-Bipyridine Complexes with Distant Carboxylic Acids

2.1 Introduction

The importance and versatility of proton-coupled electron transfer (PCET) reactions has been described in Chapter 1. In order for proton transfer and electron transfer to be coupled, the reactivity of the proton and electron must be dependent on each other to some extent. For example, the first step in the mechanism of water oxidation by the single-site ruthenium catalyst, *cis*-$Ru^{II}(bpy)_2(py)(OH_2)^{2+}$, has been proposed to be the loss of one electron and one proton to give *cis*-$Ru^{III}(bpy)_2(py)(OH)^{2+}$. The oxidation of Ru(II) to Ru(III) results in a change in the pK_a of the aquo proton by 9.75 pK_a units, from 10.6 to 0.85, respectively.[1] Thus, with loss of the electron from *cis*-$Ru^{II}(bpy)_2(py)(OH_2)^{2+}$, the aquo proton becomes highly acidic, and is released in a single kinetic step along with the electron. Mechanisms of this type will be referred to as concerted proton-electron transfer (CPET) in this text.[2]

The proximity of redox and acid/base sites is an important factor in the PCET reactivity of both organic and inorganic systems. Phenols are commonly found to be involved in biological PCET reactions as tyrosine residues. Phenols lose one electron and one proton from the same O-H bond to form phenoxyl radicals. The sequential loss of a proton or electron is highly unfavorable since the loss of one has a large effect on the reactivity of the other due to their close proximity to each other. Loss of an electron gives phenoxyl radical cation with a pK_a of -2 (12 pK_a units more negative than the pK_a of phenol), and loss of a proton gives phenoxide, which has an $E(RO^{\bullet/-})$ of

0.79 (0.71 V more negative than $E(ROH^{\bullet+/0})$).[3] In the ruthenium water oxidation catalyst, *cis*-$Ru^{II}(bpy)_2(py)(OH_2)^{2+}$, the electron is formally lost from the ruthenium center and the proton is lost from the oxygen of the aquo ligand. This separation of redox and acid/base sites corresponds to a smaller shift in pK_a upon oxidation than for phenol (9.75 pK_a units as opposed to 12).[1] These differences in redox potentials and pK_a values provide a quantitative measure of the thermochemical coupling between the redox and acid/base sites.

Manner et al. synthesized and characterized ruthenium-terpyridine complexes with even further separation between the redox and acid/base sites (Figure 2.1).[4-6] The terpyridine ligand places a carboxylic acid at a distance of 6.9 Å from the ruthenium center, and addition of a phenyl spacer to the ligand architecture further increases the distance to 11 Å. For the ruthenium complexes with 11 Å separation between the redox and acid/base sites, the $E(Ru^{III/II})$ shifted by only 2 ± 19 mV upon deprotonation of the distant carboxylic acid. Thus, the thermochemical coupling between the ruthenium center and the carboxylic acid is very small. These complexes were highly reactive in the Ru(III) oxidation state, and difficulties with decomposition were an issue in these studies.[4-6]

Herein, new ruthenium complexes with a carboxylic acid are described in order to study the effects of a distant, labile proton on the electronic properties of the ruthenium center (Figure 2.2).

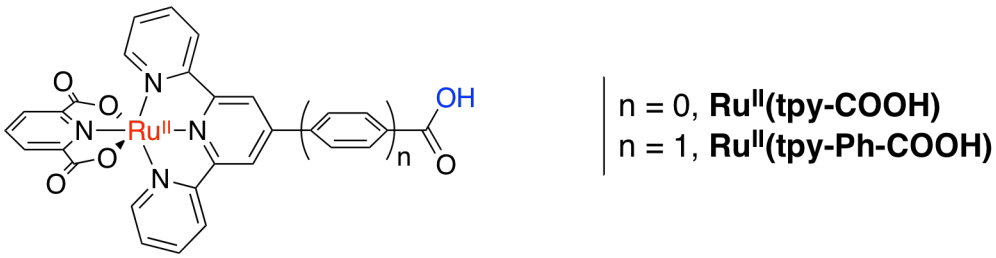

Figure 2.1. Ruthenium-terpyridine complexes with a distant carboxylic acid.[4-6]

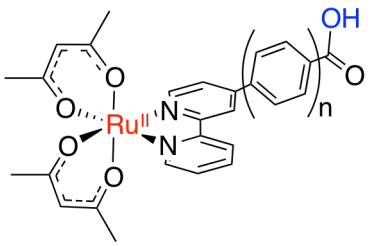

n = 0, **Ru^{II}(bpy-COOH)**
n = 1, **Ru^{II}(bpy-Ph-COOH)**

Figure 2.2. Ruthenium-bipyridine complexes with a distant carboxylic acid.

These complexes have low reduction potentials (providing relatively stable Ru(II) and Ru(III) oxidation states), and a single proton transfer site. To further separate the proton transfer site from the ruthenium, a phenyl group is inserted between a pyridine ring and the carboxylic acid.

2.2 Results

2.2.1 Synthesis of Ru^{II}(bpy-COOH) and Ru^{II}(bpy-Ph-COOH). The ruthenium complexes were prepared followed a similar procedure for ruthenium bis(*β*-diketonato) pyridine-imidazole complexes (Scheme 2.1).[7] Ruthenium (II) bis(acetonitrile) bis(acetylacetonate) ($Ru^{II}(acac)_2(MeCN)_2$) was treated with one equivalent of the bipyridine ligand of interest in DMF. The orange mixture was heated to 40 °C overnight, forming a dark green solution.

The **bpy-COOH** ligand was purchased from HetCat and used as received. Conversely, the **bpy-Ph-COOH** ligand was previously unreported and was synthesized by modified literature procedures. The synthetic procedure consists of two consecutive C-C couplings (Scheme 2.2). First, a pyridine is attached to a methyl benzoate group through a Suzuki coupling reaction using 2-chloropyridine-4-boronic acid pinacol ester, 1.2 equivalents of methyl 4-iodobenzoate, and $Pd(dppf)Cl_2•CH_2Cl_2$ as the catalyst. Next, a second pyridine group is attached to the Suzuki coupling product through a Stille coupling reaction using 1.4 equivalents of 2-(tributylstannyl)pyridine and $Pd(PPh_3)_2Cl_2$ as the catalyst. Purification of the deprotected

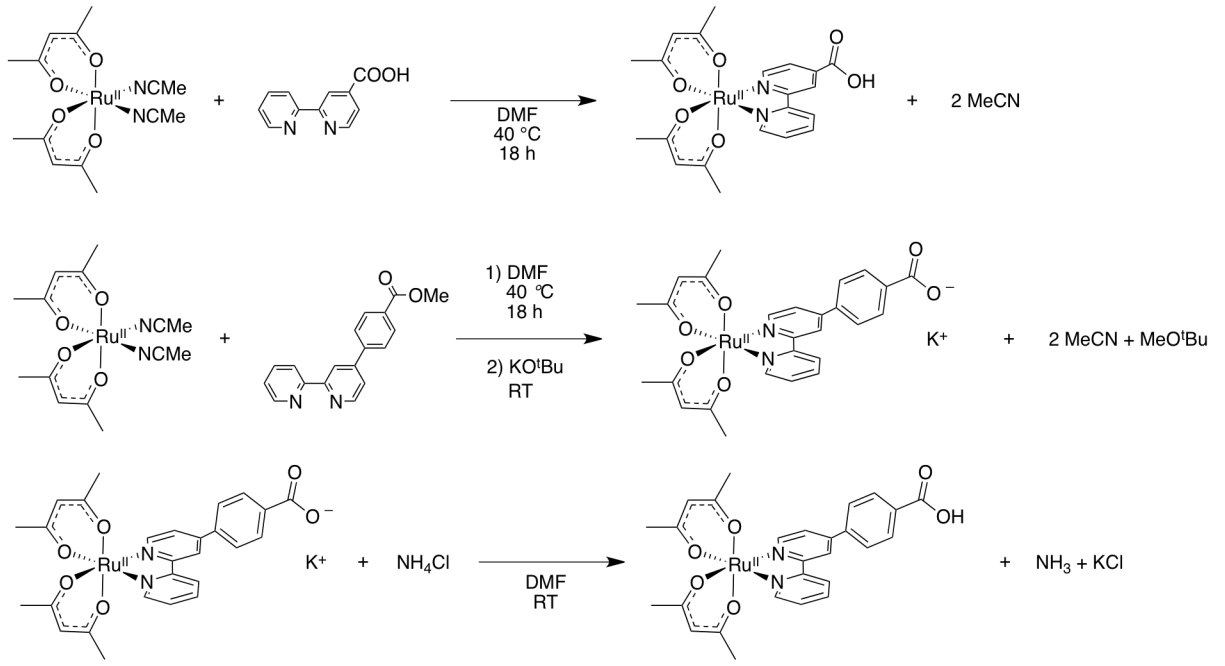

Scheme 2.1. Synthesis procedures for ruthenium complexes **Ru^{II}(bpy-COOH)** and **Ru^{II}(bpy-Ph-COOH)**.

product, **bpy-Ph-COOH**, proved to be difficult, leading to problems in the synthesis of **Ru^{II}(bpy-Ph-COOH)**. Therefore, $Ru^{II}(acac)_2(MeCN)_2$ was treated with one equivalent of **bpy-Ph-COOMe**, and the methyl ester was subsequently deprotected by addition of one equivalent of potassium *tert*-butoxide at room temperature. The carboxylate was then protonated by addition of excess ammonium chloride.

2.2.2 Synthesis of [Bu$_4$N$^+$][Ru^{II}(bpy-COO$^-$)]. One equivalent of tetrabutylammonium hydroxide (40 wt. % solution in methanol) was added to **Ru^{II}(bpy-COOH)**, resulting in a slight color change from orange to blue-green. The **[Bu$_4$N$^+$][Ru^{II}(bpy-COO$^-$)]** product was recrystallized from THF/pentane, affording dark green crystals, from which an X-ray crystal structure was determined.

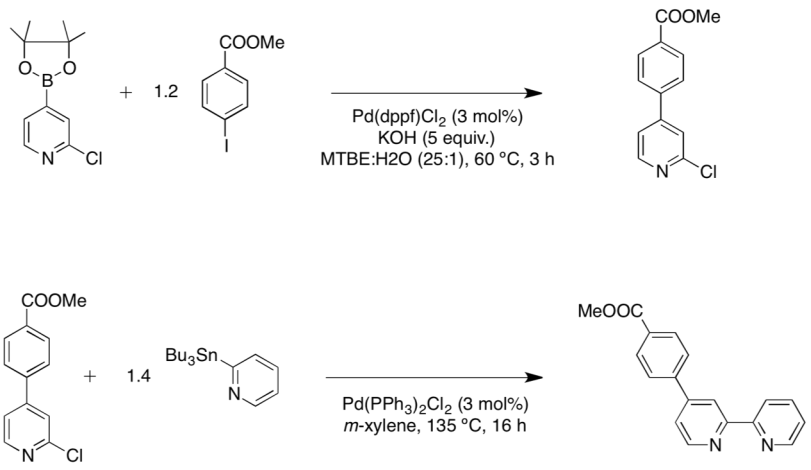

Scheme 2.2. Synthesis procedure for bipyridine ligand with phenyl spacer (**bpy-Ph-COOMe**).

2.2.3 X-ray Crystal Structure. The X-ray crystal structure of **$[Bu_4N^+][Ru^{II}(bpy\text{-}COO^-)]$** was solved and the ORTEP drawing is shown in Figure 2.3 (with 50% probability ellipsoids). Two THF molecules cocrystallized with **$[Bu_4N^+][Ru^{II}(bpy\text{-}COO^-)]$**, and both THF molecules and the tetrabutylammonium cation are hidden for clarity. The crystallographic and metric data are given in Table 2.1 and Table 2.2. The complex has a distorted octahedral geometry with trans angles >174°. The bipyridine ligand has the smallest bite angle at 79.72(15)°. The Ru−O bond lengths are in the range of 2.046(3) - 2.064(3) Å, and the Ru−N bond lengths are 1.991(3) Å and 2.002(4) Å, consistent with similar Ru(II) complexes.[10] The C−O bond lengths of the carboxylate group are consistent with a deprotonated, resonance-stabilized carboxylate group. The 0.012 Å difference in C−O bond lengths may be attributed to the closer proximity of one carboxylate oxygen to the nitrogen of the tetabutylammonium cation. The carboxylate group is rotated out of the plane of the bipyridine ring by only 2°, indicating that some conjugation between the carboxylate and the bipyridine is occurring. The distance between the ruthenium

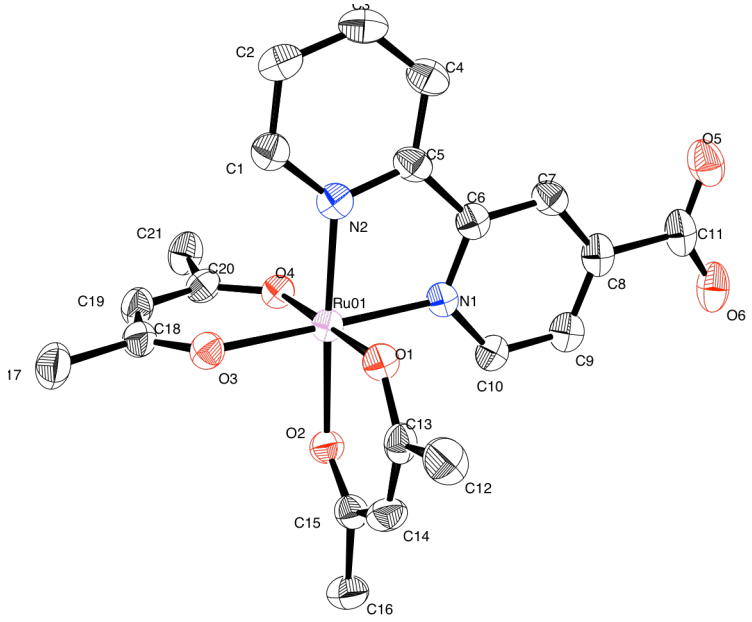

Figure 2.3. ORTEP of **[Ru^{II}(bpy-COO^{-})]**.

center and each carboxylate oxygen is 7.0 Å, similar to the previously studied ruthenium terpyridine complex.[5]

Table 2.1. Crystal data and structure refinement for **[Bu$_4$N$^+$][Ru^{II}(bpy-COO^{-})]•2THF**.

Empirical formula	$C_{45}H_{73}N_3O_8Ru$	
Formula weight	885.13	
Temperature (K)	100(2)	
Wavelength (Å)	0.71073	
Crystal description/color	black conglomerate	
Crystal system, space group	Triclinic, P $\bar{1}$	
Unit cell dimensions (Å, °)	a = 10.3681(6)	α = 100.379(5)
	b = 12.7110(9)	β = 99.851(3)
	c = 19.3552(10)	γ = 111.985(3)
Volume (Å^3)	2245.6(2)	

Z, Calculated density (Mg/m^3)	2, 1.309
Absorption coefficient (mm^{-1})	0.403
F(000)	944
Crystal size (mm^3)	0.08 x 0.07 x 0.05
Theta range for data collection (°)	1.79 to 26.42
Index ranges	$-12 \leq h \leq 12$, $-15 \leq k \leq 15$, $0 \leq l \leq 24$
Reflections collected / unique	9187 / 9187 [$R_{int} = 0.0956$]
Completeness to theta = 25.00°	100.0 %
Max. and min. transmission	0.9801 and 0.9685
Refinement method	Full-matrix least-squares on F^2
Data / restraints / parameters	9187 / 74 / 522
Goodness-of-fit on F^2	$S = 1.060$
Final R indices [I>2sigma(I)]	$R1 = 0.0622$, $wR2 = 0.1458$
R indices (all data)	$R1 = 0.0934$, $wR2 = 0.1576$
Largest diff. peak and hole ($e/Å^{-3}$)	1.252 and -0.694

Table 2.2. Selected bond lengths and angles for **[Bu_4N^+][Ru^{II}(bpy-COO^-)]**.

	Length (Å)
Ru−N1	1.991(3)
Ru−N2	2.002(4)
Ru−O1	2.046(3)
Ru−O2	2.064(3)
Ru−O3	2.061(3)
Ru−O4	2.047(3)
C11−O5	1.241(6)
C11−O6	1.253(6)
	Angle (°)
N1−Ru−N2	79.72(15)
O1−Ru−O2	92.15(12)
O3−Ru−O4	92.29(12)
N1−Ru−O3	174.36(13)
N2−Ru−O2	174.68(13)
O1−Ru−O4	179.09(12)
O5−C11−O6	128.4(5)

2.2.4 Spectroscopic Characterizations. The ^{1}H-NMR spectra of diamagnetic **Ru^{II}(bpy-COOH)** and **Ru^{II}(bpy-Ph-COOH)** are both consistent with complexes of C_1 symmetry. For **Ru^{II}(bpy-COOH)**, seven proton signals for the bipyridine ligand are seen between δ 7.44 and 9.13 ppm. Two methyne proton signals and four methyl proton signals are observed for the two inequivalent acac ligands, although two of the methyl proton signals are accidentally degenerate. Additionally, there is a broad singlet at 13.96 ppm which corresponds to the carboxylic proton. Upon deprotonation to form **Ru^{II}(bpy-COO^-)**, the two accidentally degenerate acac methyl

proton signals are resolved into two distinct singlets and the signal for the carboxylic proton is lost.

For **Ru^{II}(bpy-Ph-COOH)**, seven signals for the bipyridine protons are seen between δ 8.88 ppm and 7.20 ppm. Two doublets are observed at δ 7.90 and 8.04 ppm for the four phenyl protons, indicating that the phenyl group is freely rotating. Two methyne proton signals and four methyl proton signals are observed for the two inequivalent acac ligands. A broad singlet at 9.5 ppm corresponds to the carboxylic proton.

The UV-visible spectra of both **Ru^{II}(bpy-COOH)** and **Ru^{II}(bpy-Ph-COOH)** show MLCT bands in the visible region with large extinction coefficients (~ 8000 – 10,000 M^{-1} cm^{-1}, Figure 2.4). Deprotonation of **Ru^{II}(bpy-COOH)** to give **Ru^{II}(bpy-COO^-)** results in significant differences in the UV-vis spectrum. The energies of the two major MLCT bands of deprotonated **Ru^{II}(bpy-COO^-)** shift slightly, and the extinction coefficient of the higher energy band increases from 9600 ± 300 M^{-1} cm^{-1} to 13,000 ± 400 M^{-1} cm^{-1}. The spectrum of **Ru^{II}(bpy-Ph-COOH)** exhibits similar changes upon deprotonation to **Ru^{II}(bpy-Ph-COO^-).** The energies of two major MLCT bands shift very little, and the extinction coefficient of the higher energy band increases

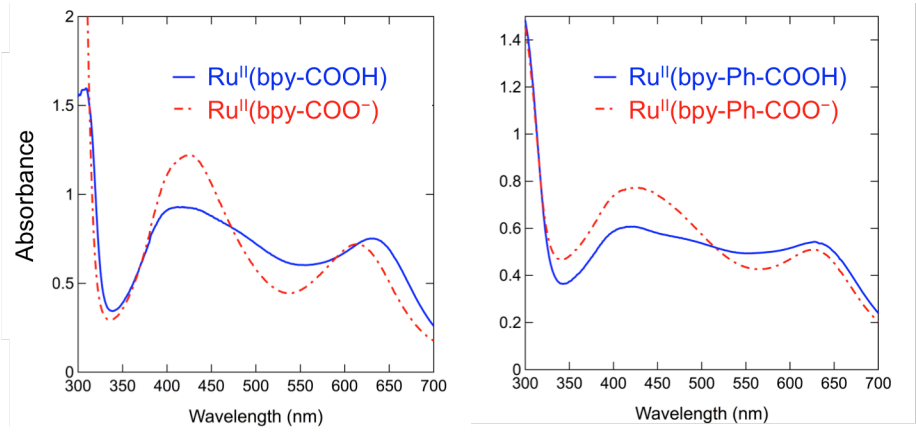

Figure 2.4. UV-vis spectra of **Ru^{II}(bpy-COOH)**, **Ru^{II}(bpy-COO^-)**, **Ru^{II}(bpy-Ph-COOH)**, and **Ru^{II}(bpy-Ph-COO^-)**.

from 8600 ± 300 M^{-1} cm^{-1} to 11,000 ± 400 M^{-1} cm^{-1}. These changes are reversible and the original spectra are observed upon reprotonation.

2.2.5 Thermochemical Measurements. The pK_a of **Ru^{II}(bpy-COOH)** was measured in MeCN by titrating **Ru^{II}(bpy-COOH)** with 4-dimethylaminopyridine (DMAP, p$K_{a,DMAPH^+}$ = 17.95 ± 0.03[8]), forming [$DMAPH^+$][**Ru^{II}(bpy-COO^-)**] in equilibrium. Changes in the optical spectra were monitored at 410 nm, and used to determine the concentrations of **Ru^{II}(bpy-COOH)** and **Ru^{II}(bpy-COO^-)**. **Ru^{II}(bpy-COOH)** was regenerated quantitatively by back-titrating with trifluoroacetic acid. Assuming that [**Ru^{II}(bpy-COO^-)**] is equal to [$DMAPH^+$], K_{eq} is calculated to be 0.11 ± 0.01 from the slope of the plot: [**Ru^{II}(bpy-COO^-)**]^2/[**Ru^{II}(bpy-COOH)**] vs. [DMAP]. This K_{eq} and the pK_a of $DMAPH^+$ give pK_a(**Ru^{II}(bpy-COOH)**) = 18.9 ± 0.4. Using the same procedure and sodium *p*-nitrobenzoate as the base (p$K_{a,p\text{-nitro-PhCOOH}}$ = 18.7 ± 0.1[8]), the pK_a of **Ru^{II}(bpy-Ph-COOH)** was determined to be 20.9 ± 0.2.

Cyclic voltammograms (CVs) of both complexes show chemically reversible waves corresponding to the $Ru^{III/II}$ couple, and the data are summarized in Table 2.3. The solutions were titrated with base followed by acid to accurately determine the shift in $Ru^{III/II}$ reduction potential of the **Ru(bpy-Ph-COOH)** complex upon deprotonation. A CV was taken of a 1 mM solution of **Ru^{II}(bpy-Ph-COOH)**, then excess base (tetrabutylammonium *p*-nitrobenzoate) was added until the wave stopped shifting to more negative potentials. Excess benzoic acid was then added until the wave returned to the initial potential (Figure 2.5).

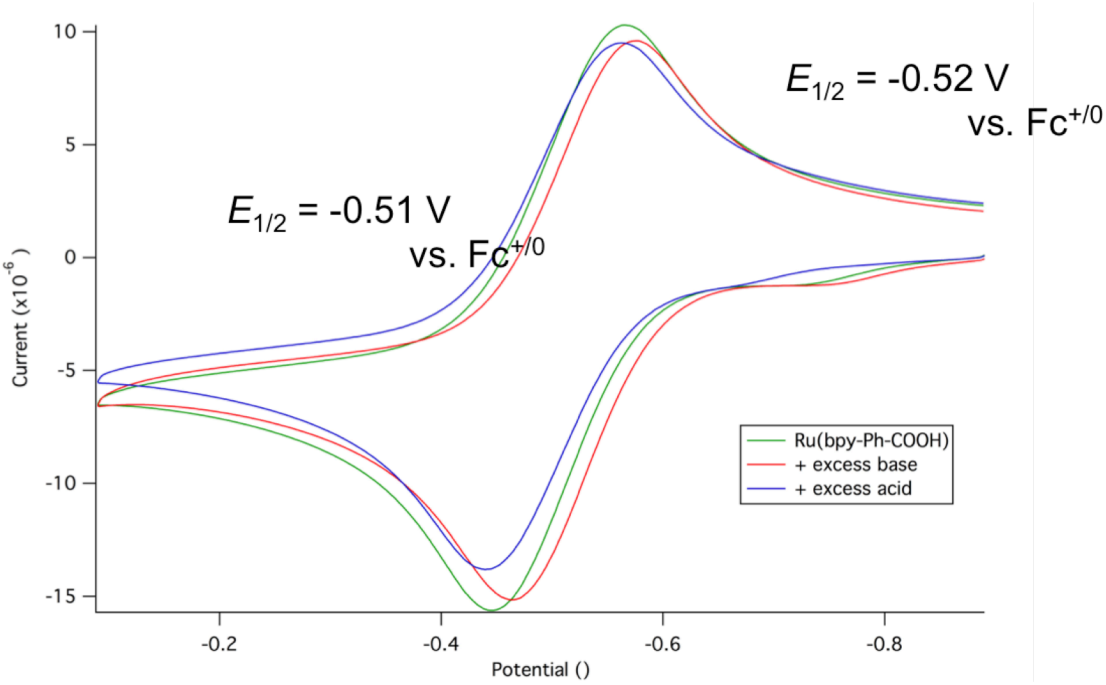

Figure 2.5. Cyclic voltammogram of **Ru^{II}(bpy-Ph-COOH)** with excess base and excess acid.

Table 2.3. Cyclic voltammetry for **Ru(bpy-COOH)**, **Ru(bpy-COO^-)**, **Ru(bpy-Ph-COOH)**, and **Ru(bpy-Ph-COO^-)** in MeCN.[a, b]

	$E_{1/2}$ (V)	$\Delta E_{1/2}$ (V)
$Ru^{III/II}$(bpy-COOH)	-0.39 ± 0.02	0.10 ± 0.028
$Ru^{III/II}$(bpy-COO^-)	-0.49 ± 0.02	
$Ru^{III/II}$(bpy-Ph-COOH)	-0.46 ± 0.02	0.03 ± 0.028
$Ru^{III/II}$(bpy-Ph-COO^-)	-0.49 ± 0.02	

[a] $E_{1/2}$ values in V vs. $Cp_2Fe^{+/0}$. [b] $\Delta E_{1/2} = E_{1/2}$(**Ru^{II}~COOH**) – $E_{1/2}$(**Ru^{II}~COO^-**).

2.3 Discussion

2.3.1 Thermochemical Coupling. The shift of the pK_a values of the ruthenium complexes from the pK_a of benzoic acid is defined as the thermochemical coupling between the ruthenium center and the carboxylic acid site. The trend of the pK_a values of **Ru^{II}(bpy-COOH)** and **Ru^{II}(bpy-Ph-COOH)** agrees with the relative distances between the ruthenium center and the carboxylic acid. In **Ru^{II}(bpy-COOH)** where the carboxylic acid is closer to the ruthenium center, the pK_a is 2 units lower than the pK_a of **Ru^{II}(bpy-Ph-COOH)**. This is likely a result of the donation of electron density from the bipyridine ligand to the metal center, making the carboxylic acid closer to the metal more acidic. The pK_a of **Ru^{II}(bpy-Ph-COOH)** is 20.9 and is only 0.2 pK_a units higher than the pK_a of benzoic acid. The phenyl spacer further separates the carboxylic acid from the ruthenium such that the acidity of the carboxylic acid is not greatly affected by the metal center.

The deprotonated **Ru^{II}(bpy-COO^-)** is easier to oxidize than **Ru^{II}(bpy-COOH)** as indicated by the lower potential of the Ru(III/II) redox couple of **Ru^{II}(bpy-COO^-)**. This difference in potential provides another measure of the thermochemical coupling between the ruthenium center and the carboxylic acid site. The difference in potential of the Ru(III/II) redox couples of **Ru^{II}(bpy-COOH)** and **Ru^{II}(bpy-COO^-)** is 0.10 ± 0.028 V, and is similar in magnitude to the ruthenium terpyridine complexes with comparable separation between the metal center and a carboxylic acid.[5] For **Ru^{II}(bpy-Ph-COOH)**, the potential of the redox couple shifts by only 30 ± 28 mV upon deprotonation. Thus, the ruthenium center is affected only slightly by the protonation state, so there is very little thermochemical coupling between the ruthenium center and the carboxylic acid. This small coupling of 30 ± 28 mV agrees with the small

thermochemical coupling found in ruthenium and iron complexes with similar separation between the metal center and a distant carboxylic acid.[6,9]

Surprisingly, the UV-vis spectra of **Ru^{II}(bpy-COOH)** and **Ru^{II}(bpy-COO^-)** do not differ significantly from the corresponding spectra of **Ru^{II}(bpy-Ph-COOH)** and **Ru^{II}(bpy-Ph-COO^-)**. The spectrum of **Ru^{II}(bpy-Ph-COOH)** exhibits similar changes upon deprotonation to **Ru^{II}(bpy-COOH)**, despite the acidic proton being separated from the metal center by an additional 4 bonds. This is in contrast to previous results reported by Manner et al with related ruthenium-terpyridine complexes.[4-6] For the ruthenium-terpyridine complex for which the acidic proton is separated from the metal center by 7.0 Å, changes in the UV-vis spectrum upon deprotonation are similar to those observed for **Ru^{II}(bpy-COOH)**. However, for the ruthenium-terpyridine complex for which the acidic proton is 11.2 Å separated from the metal center, there is very little change in the UV-vis spectrum upon deprotonation. This difference could possibly be due to the different supporting ligands of **Ru^{II}(bpy-COOH)** and **Ru^{II}(bpy-Ph-COOH)** versus the ruthenium-terpyridine complexes. The MLCT transitions of polypyridyl ruthenium (II) complexes often involve relatively low-lying pyridine ligand LUMOs. In **Ru^{II}(bpy-COOH)** and **Ru^{II}(bpy-Ph-COOH)**, there are two pyridine rings, one of which is directly attached to the acidic carboxylic acid or benzoic acid group. In contrast, the ruthenium-terpyridine complexes each have four pyridine rings, only one of which is directly attached to a carboxylic acid or benzoic acid group. Thus, for the ruthenium-terpyridine complexes there are more pyridine rings farther away from the acidic proton whose LUMOs could be involved in the major MLCT bands. Perhaps the LUMOs of major MLCT bands in the ruthenium-terpyridine complexes are primarily comprised of orbitals on the pyridine ligand that is located trans to the carboxylic acid or benzoic acid group. The LUMOs of the major MLCT bands of **Ru^{II}(bpy-COOH)** and

Ru^{II}(bpy-Ph-COOH) are more likely to be comprised of orbitals on the bipyridine ligand with an acidic proton.

2.4 Conclusion

In **Ru^{II}(bpy-COOH)**, there is noticeable thermochemical coupling and the ruthenium and carboxylic acid are close enough to mediate the reactivity of the other. The pK_a of the carboxylic acid separated by 7.0 Å from the ruthenium center is more acidic than the pK_a of benzoic acid and the potential of the Ru(III/II) redox couple shifts upon deprotonation. The **Ru^{II}(bpy-Ph-COOH)** conversely exhibits very little thermochemical coupling, and the ruthenium center and carboxylic acid behave nearly independently without affecting the pK_a or the Ru(III/II) redox couple of the other site. Considering this lack of thermochemical coupling between the sites, it is surprising that the UV-vis spectra **Ru^{II}(bpy-Ph-COOH)** and **Ru^{II}(bpy-Ph-COO^-)** are significantly different.

2.5 Experimental Section

2.5.1 General Considerations. All manipulations were carried out under nitrogen using glove-box/vacuum line techniques unless otherwise noted. Chemicals were purchased from Aldrich, Alfa-Aesar, EMD, Macron, or Fisher and used as received unless otherwise noted. 2,2′-bipyridine-4-carboxylic acid (bpy-COOH) was purchased from HetCat. 2-chloropyridine-4-boronic acid was purchased from Frontier Scientific. 2-chloropyridine-4-boronic acid pinacol ester and tetrabutylammonium *p*-nitrobenzoate were synthesized following literature procedures.[17,18] Solvents used in the glove-box (dimethylformamide (DMF), dichloromethane (DCM), tetrahydrofuran (THF), and pentane) were purchased from Fischer Scientific and were dried using a Seca Solvent System installed by Glass Contour. These solvents were subsequently stored over 4 Å molecular sieves. Anhydrous acetonitrile (MeCN; <10 ppm H_2O) was purchased from Honeywell Burdick & Jackson, sparged with argon, and plumbed from a steel keg directly into a glovebox. Deuterated CD_3CN was purchased from Cambridge Isotope Laboratories, dried over CaH_2, vacuum transferred to P_2O_5, then vacuum transferred to fresh CaH_2 and finally into an empty vessel. Sealed ampules of deuterated DMF-d_7 were purchased from Cambridge Isotope Laboratories and used as received. All other solvents were purchased from Fisher Scientific or EMD Chemicals and used as received. Elemental analysis was performed by Complete Analysis Laboratories, Inc.

2.5.2 Spectroscopic Measurements. All samples were prepared under N_2, unless otherwise noted. ^{1}H-NMR spectra were obtained on Bruker Avance spectrometers (Avance-500, DRX-499, Avance-300, and Avance-301), referenced to a residual solvent peak, and reported as δ (number of protons). UV-visible spectra were obtained with a Hewlett-Packard 8453 diode-array

spectrophotometer. Electrochemical measurements were obtained with a CH Instruments Model 600D potentiostat.

2.5.3 Synthetic Procedures.

2.5.3.1 Synthesis of $Ru^{II}(acac)_2$(bpy-COOH) (Ru^{II}(bpy-COOH)). $Ru^{II}(acac)_2(MeCN)_2$ (0.20 g, 0.52 mmol) in 8 mL of DMF was treated with 1.4 equivalents (0.15 g, 0.75 mmol) of 2,2′-bipyridine-4-carboxylic acid (bpy-COOH). The orange mixture was sonicated, then stirred at 40 ºC for 18 hours, resulting in a dark green mixture. The green mixture was filtered through Celite. The DMF was removed in vacuo at 40 ºC to give a dark green residue. Yield: 0.23 g (0.46 mmol), 86%. ^{1}H-NMR (DMF-d_7) δ: 1.54 (s, 6H, acac-CH_3), 2.08 (s, 3H, acac-CH_3), 2.14 (s, 3H, acac-CH_3), 5.33 (s, 1H, acac-CH), 5.38 (s, 1H, acac-CH), 7.44 (t, 1H, bpy-$H_{4'/5'}$, $^3J_{HH}$ = 6.0 Hz), 7.71 (dd, 1H, bpy-H_5, $^3J_{HH}$ = 6.0 Hz, $^4J_{HH}$ = 1.5 Hz), 7.76 (t, 1H, bpy-$H_{4'/5'}$, $^3J_{HH}$ = 9.0 Hz), 8.69 (d, 1H, bpy-$H_{3'/6'}$, $^3J_{HH}$ = 9.0 Hz), 8.77 (d, 1H, bpy-H_3, $^4J_{HH}$ = 1.5 Hz), 8.80 (d, 1H, bpy-$H_{3'/6'}$, $^3J_{HH}$ = 6.0 Hz), 9.13 (d, 1H, bpy-H_6, $^3J_{HH}$ = 6.0 Hz), 13.96 (broad s, 1H, bpy-COOH). UV-vis (MeCN): 410 (9600), 630 (8600). Anal. Calcd (Found) for $C_{21}H_{22}N_2O_6Ru\bullet H_2O$: C, 48.74 (48.36); H, 4.67 (4.98); N, 5.41 (5.29).

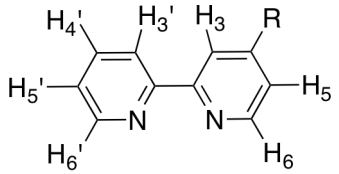

R = COOH, PhCOOH, PhCOOMe

Scheme 2.3. Labels for bipyridine protons.

2.5.3.2 Synthesis of $Ru^{II}(acac)_2(bpy\text{-}COO^-)$ ($Ru^{II}(bpy\text{-}COO^-)$). A solution of **$Ru^{II}(bpy\text{-}COOH)$** (0.23 g, 0.46 mmol) in 10 mL of DCM was treated with 309 mg of tetrabutylammonium hydroxide solution (40 wt.% in methanol, 1.0 equiv.). A slight color change from green to blue-green was observed. The DCM was removed in vacuo. The product was recrystallized from THF and pentane to give dark green x-ray quality crystals. Yield: 0.25 g (0.34 mmol), 73%. ^{1}H-NMR (CD_2Cl_2) δ: 1.00 (t, 12H, NBu-CH_3, $^3J_{HH}$ = 7.5 Hz), 1.43 (m, 8H, NBu-CH_2, $^3J_{HH}$ = 7.5 Hz), 1.58 (s, 3H, acac-CH_3), 1.60 (s, 3H, acac-CH_3), 1.67 (m, 8H, NBu-CH_2, $^3J_{HH}$ = 7.5 Hz, $^3J_{HH}$ = 8.5 Hz), 2.14 (s, 3H, acac-CH_3), 2.15 (s, 3H, acac-CH_3), 3.32 (t, 8H, NBu-CH_2, $^3J_{HH}$ = 8.5 Hz), 5.33 (s, 2H, acac-CH), 7.12 (t, 1H, bpy-$H_{4'/5'}$, $^3J_{HH}$ = 6.2 Hz), 7.49 (t, 1H, bpy-$H_{4'/5'}$, $^3J_{HH}$ = 8.0 Hz), 7.73 (d, 1H, bpy-$H_{5/6}$, $^3J_{HH}$ = 5.5 Hz), 8.16 (d, 1H, bpy-$H_{3'/6'}$, $^3J_{HH}$ = 8.0 Hz), 8.66 (s, 1H, bpy-H_3), 8.70 (d, 1H, bpy-$H_{3'/6'}$, $^3J_{HH}$ = 6.2 Hz), 8.77 (d, 1H, bpy-$H_{5/6}$, $^3J_{HH}$ = 5.5 Hz). UV-vis (MeCN): 426 (13000), 613 (7800).

2.5.3.3 Synthesis of Methyl *p*-(2-chloro-4-pyridyl)benzoate. Methyl 4-(2-chloro-4-pyridinyl)-benzoate was synthesized following a similar procedure to that of methyl 4-(2,6-dichloro-4-pyridinyl)-benzoate.[10] Methyl 4-iodobenzoate (5.0 g, 19 mmol, 1.2 equiv.), 2-chloropyridine-4-boronic acid pinacol ester (3.8 g, 15 mmol), Pd(dppf)Cl_2•CH_2Cl_2 (0.39 g, 0.48 mmol, 3 mol%), MTBE (400 mL), and KOH (aq) (5 M, 16 mL) were combined in a 1000 mL round bottom flask. The reaction mixture was heated to 60 ºC for 3 hours. The reaction was cooled and the aqueous layer was removed. The MTBE was removed under vacuum. The resulting solids were dissolved in DCM and filtered in air. The filtrate was loaded onto a silica gel column and eluted with DCM to afford the product. The product was characterized in air. Yield: 1.5 g (6.0 mmol), 38%. ^{1}H-NMR ($CDCl_3$) δ: 3.95 (s, 3H, $COOCH_3$), 7.45 (dd, 1H, pyr-H_5, $^3J_{HH}$ = 5.0 Hz, $^4J_{HH}$ = 1.5 Hz),

7.56 (d, 1H, pyr-H_3, $^4J_{HH}$ = 1.5 Hz), 7.67 (d, 2H, Ph-H, $^3J_{HH}$ = 8.5 Hz), 8.15 (d, 2H, Ph-H, $^3J_{HH}$ = 8.5 Hz), 8.46 (d, 1H, pyr-H_6, $^3J_{HH}$ = 5.0 Hz). Anal. Calcd (Found) for $C_{13}H_{10}NO_2Cl$: C, 63.04 (63.15); H, 4.07 (3.97); N, 5.66 (5.71).

2.5.3.4 Synthesis of Methyl *p*-(2,2′-bipyridyl-4-yl)benzoate (bpy-Ph-COOMe). Methyl 4-(4-2,2′-bipyridinyl)-benzoate was synthesized following a modified literature procedure for methyl 2,2'-bipyridine-4-carboxylate.[11] Methyl 4-(2-chloro-4-pyridinyl)-benzoate (1.0 g, 4.0 mmol), $Pd(PPh_3)_2Cl_2$ (0.14 g, 0.20 mmol, 3.3 mol%), and anhydrous *m*-xylene (30 mL) were added to a 50-mL round bottom flask. 2-(tributylstannyl)pyridine (2.0 g, 5.4 mmol, 1.4 equiv.) was added to the reaction flask by syringe. The reaction mixture was heated to 135 ºC for 16 hours. The reaction mixture was cooled and the *m*-xylene was removed under vacuum. 150 mL of DCM was added and the resulting slurry was filtered through Celite in air. The filtrate was extracted with 6 M aqueous HCl (3x40 mL). The aqueous layer was washed with 50 mL of DCM, then the water and HCl were removed under vacuum. 50 mL of water was added to the resulting orange solids and concentrated aqueous ammonium hydroxide was added until the pH of the solution was 9. The resulting blue-gray slurry was extracted with DCM (2x75 mL) and the DCM was removed from the organic layer under vacuum to give a gray residue. The product was isolated by recrystallization from DCM/hexanes. The product was characterized in air. Yield: 0.20 g (0.69 mmol), 17%. ^{1}H-NMR ($CDCl_3$) δ: 3.96 (s, 3H, $COOCH_3$), 7.34 (td, 1H, pyr-$H_{4'}$, $^3J_{HH}$ = 7.8 Hz, $^3J_{HH}$ = 4.9 Hz), 7.56 (dd, 1H, pyr-H_5, $^3J_{HH}$ = 5.2 Hz, $^4J_{HH}$ = 1.7 Hz), 7.88 (d, 2H Ph-H, $^3J_{HH}$ = 8.5 Hz), 7.92 (td, 1H, pyr-$H_{5'}$, $^3J_{HH}$ = 7.8 Hz, $^4J_{HH}$ = 1.8 Hz), 8.16 (d, 2H, Ph-H, $^3J_{HH}$ = 8.5 Hz), 8.46 (d, 1H, pyr-$H_{6'}$, $^3J_{HH}$ = 7.8 Hz), 8.69 (dd, 1H, pyr-$H_{3'}$, $^3J_{HH}$ = 4.9 Hz, $^4J_{HH}$ = 1.8 Hz), 8.72 (d, 1H,

pyr-H_3, $^4J_{HH}$ = 1.7 Hz), 8.76 (dd, 1H, pyr-H_6, $^3J_{HH}$ = 5.2 Hz). Anal. Calcd (Found) for $C_{18}H_{14}N_2O_2$: C, 74.47 (74.26); H, 4.86 (4.68); N, 9.65 (9.58).

2.5.3.5 Synthesis of $Ru^{II}(acac)_2$(bpy-Ph-COOH) (Ru^{II}(bpy-Ph-COOH)). A solution of $Ru^{II}(acac)_2(MeCN)_2$ (0.14 g, 0.36 mmol) in 16 mL of DMF was treated with 0.11 g (0.39 mmol, 1.1 equivalents) of methyl 4-(4-2,2′-bipyridinyl)-benzoate (bpy-Ph-COOMe). The orange mixture was stirred at 40 ºC for 18 hours, resulting in a black-green mixture. One equivalent of potassium *tert*-butoxide was added to the reaction mixture and an immediate color change to a more vibrant green was observed. Excess NH_4Cl was added to the solution of **Ru^{II}(bpy-Ph-COO^-)** and a color change to dark blue-green was observed. 25% yield. ^{1}H-NMR (DMF-d_7) δ: 1.58 (s, 3H, acac-CH_3), 1.59 (s, 3H, acac-CH_3), 2.13 (s, 3H, acac-CH_3), 2.16 (s, 3H, acac-CH_3), 5.30 (s, 1H, acac-CH), 5.32 (s, 1H, acac-CH), 7.20 (t, 1H, pyr-$H_{4'/5'}$, $^3J_{HH}$ = 6.4 Hz), 7.40 (t, 1H pyr-$H_{4'/5'}$, $^3J_{HH}$ = 8.0 Hz), 7.54 (d, 1H, pyr-$H_{5/6}$, $^3J_{HH}$ = 6.0 Hz), 7.90 (d, 2H, Ph-H, $^3J_{HH}$ = 7.9 Hz), 8.04 (d, 2H, Ph-H, $^3J_{HH}$ = 7.9 Hz), 8.13 (d, 1H, pyr-$H_{3'/6'}$, $^3J_{HH}$ = 8.0 Hz), 8.22 (d, 1H, pyr-$H_{3'/6'}$, $^3J_{HH}$ = 6.4 Hz), 8.72 (s, 1H, pyr-H_3), 8.88 (d, 1H, pyr-$H_{5/6}$, $^3J_{HH}$ = 6.0 Hz), 9.5 (broad s, 1H, COOH). UV-vis (MeCN): 410 (8600), 630 (7800). Anal. Calcd (Found) for $C_{27}H_{26}N_2O_6Ru{\bullet}NH_4Cl$: C, 51.55 (52.54); H, 4.81 (4.22); N, 6.68 (6.32).

2.5.3.6 Independently Generated Ru^{III}(bpy-COO). Potassium 2,2′-bipyridine-4-carboxylate (bpy-COO^-K^+) was synthesized by combining 63 mg (0.32 mmol) of 2,2′-bipyridine-4-carboxylic acid in 5 mL of DMF with 20 mg (0.50 mmol, 1.6 equiv.) of potassium hydride and stirring for 2 hours. The solution was filtered to remove unreacted potassium hydride and the DMF was removed in vacuo.

3 mg of bpy-COO^-K^+, 6 mg of $[Ru^{III}(acac)_2(MeCN)_2][OTf]$, and 5 μL of a 0.3 M standard solution of HMDSO in CD_2Cl_2 were combined with 0.5 mL of CD_2Cl_2 in a J. Young tube.[12] The reaction mixture was heated to 40 ºC for 12 hours. A ^{1}H-NMR spectrum of the reaction mixture showed formation of a signal for free acetonitrile and the paramagnetic signals for $[Ru^{III}(acac)_2(MeCN)_2][OTf]$ had shifted. Additionally, a dark maroon precipitate formed in the tube. The CD_2Cl_2 solution was removed and the solids were dissolved in MeCN. A portion of this solution was diluted and a UV-vis spectrum was obtained, which revealed a peak at 524 nm. The MeCN was removed in vacuo and the resulting solids were redissolved in DMF-d_7. A ^{1}H-NMR spectrum of the DMF-d_7 solution showed a signal at -22 ppm.

2.5.4 X-ray Crystal Structure of $[Bu_4N^+][Ru^{II}(bpy\text{-}COO^-)]$•2THF. X-ray crystallography was performed by Michael K. Coggins and Werner Kaminsky at the Chemistry X-ray Diffraction Facility. A black conglomerate, measuring 0.08 x 0.07 x 0.05 mm^3 was mounted on a glass capillary with oil. Data was collected at -173 ^oC on a Bruker APEX II single crystal X-ray diffractometer, Mo-radiation. Crystal-to-detector distance was 40 mm and exposure time was 60 seconds per frame for all sets. The scan width was 0.5^o. Data collection was 100% complete to 25^o in ϑ. After unfolding the diffraction pattern two individual crystals where found cell now[13], the diffraction of which was merged with twinabs to yield a total of 9187 unique reflections were collected covering the indices, h = -12 to 12, k = -15 to 15, l = 0 to 24 and the R_{int} = 0.0956 indicated that the untwined data was of slightly less than average quality (0.07). Indexing and unit cell refinement indicated a triclinic lattice. The space group was found to be P $\bar{1}$ (No.2). The data was integrated and scaled using SAINT within the APEX2 software package by Bruker.[14] Solution by direct methods (SIR92[15]) produced a complete heavy atom phasing model

consistent with the proposed structure. The structure was completed by difference Fourier synthesis with SHELXL97.[13,16] Scattering factors are from Waasmair and Kirfel.[17] Hydrogen atoms were placed in geometrically idealised positions and constrained to ride on their parent atoms with C---H distances in the range 0.95-1.00 Angstrom. Isotropic thermal parameters U_{eq} were fixed such that they were $1.2U_{eq}$ of their parent atom Ueq for CH's and $1.5U_{eq}$ of their parent atom U_{eq} in case of methyl groups. All non-hydrogen atoms were refined anisotropically by full-matrix least-squares. The Ru complex is accompanied by two disordered THF solvent molecules and a slightly disordered tetrabutylamine cation.

2.5.5 Thermochemical Measurements.

2.5.5.1 Titrations of Ru^{II}(bpy-COOH) with strong base and strong acid. The carboxylic proton of **Ru^{II}(bpy-COOH)** can be reversibly deprotonated and protonated with sufficiently strong bases and acids. 2 μL aliquots of a 4.8 mM solution of 1,8-diazabicycloundec-7-ene (DBU) were added to 2 mL of a 34 μM solution of **Ru^{II}(bpy-COOH)** until a total of 1.1 equivalents had been added. Changes in the UV-vis spectrum were monitored after each addition, and the spectrum stopped changing after 1.0 equivalents of DBU had been added. Addition of 16 μL of a 4.8 mM solution of malonic acid (1.1 equivalents) to the [$DBUH^+$][**Ru^{II}(bpy-COO^-)**] solution regenerated **Ru^{II}(bpy-COOH)** in 99 ± 1% yield by UV-vis spectroscopy.

2.5.5.2 pK_a Determination for Ru^{II}(bpy-COOH). Titrating **Ru^{II}(bpy-COOH)** with dimethylaminopyridine results in formation of [$DMAPH^+$][**Ru^{II}(bpy-COO^-)**] in equilibrium. 5 μL aliquots of a 40 mM solution of DMAP were added to a solution of 2 mL of 81 μM **Ru^{II}(bpy-COOH)** up to a total of 15 equivalents. Changes in the UV-vis spectrum were monitored after each addition at 410 nm (Figure 2.6A). The absorbance values were corrected for volume additions. The concentrations of **Ru^{II}(bpy-COOH)** and [**Ru^{II}(bpy-COO^-)**] were calculated using the equations below, where *A* is the volume-corrected absorbance at 410 nm and *b* is the pathlength of the cell (1 cm).

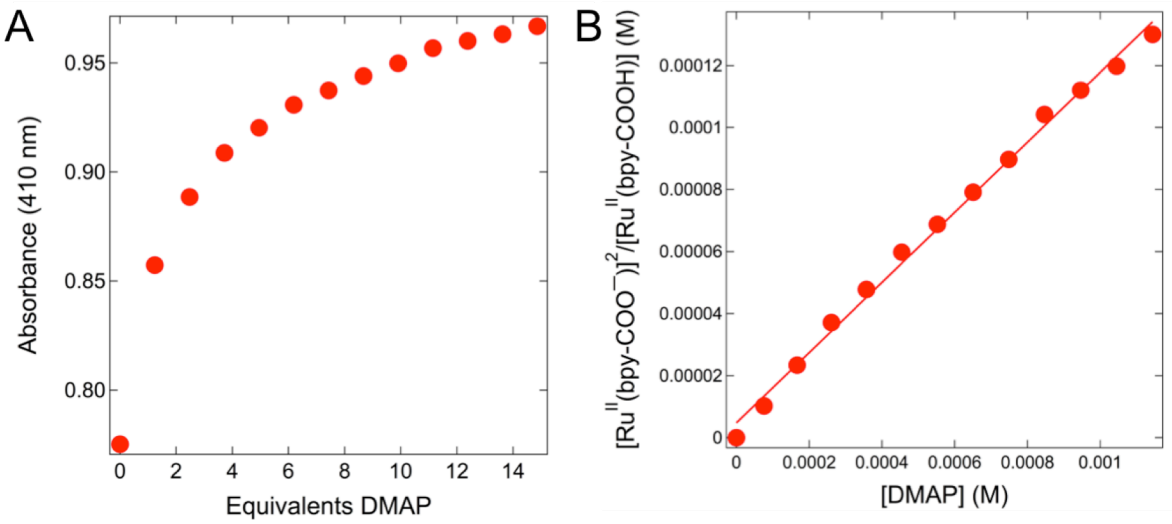

Figure 2.6A. Change in UV-vis absorbance at 410 nm upon addition of DMAP to Ru^{II}(bpy-COOH). **Figure 2.6B.** Plot of [**Ru^{II}(bpy-COO^-)**]^2/[**Ru^{II}(bpy-COOH)**] vs. [DMAP].

$$A_{410\text{ nm}} = \varepsilon_{Ru^{II}(bpy\text{-}COOH)} b[Ru^{II}(bpy\text{-}COOH)] + \varepsilon_{Ru^{II}(bpy\text{-}COO^-)} b[Ru^{II}(bpy\text{-}COO^-)]$$

$$+[Ru^{II}]_{TOTAL} = [Ru^{II}(bpy\text{-}COOH)] + [Ru^{II}(bpy\text{-}COO^-)]$$

$$[Ru^{II}(bpy\text{-}COOH)] = \frac{A_{410\text{ nm}} - \varepsilon_{Ru^{II}(bpy\text{-}COO^-)}[Ru^{II}]_{TOTAL}}{\varepsilon_{Ru^{II}(bpy\text{-}COOH)} - \varepsilon_{Ru^{II}(bpy\text{-}COO^-)}}$$

$$[Ru^{II}(bpy\text{-}COO^-)] = \frac{A_{410\text{ nm}} - \varepsilon_{Ru^{II}(bpy\text{-}COOH)}[Ru^{II}]_{TOTAL}}{\varepsilon_{Ru^{II}(bpy\text{-}COO^-)} - \varepsilon_{Ru^{II}(bpy\text{-}COOH)}}$$

$$K_{eq} = \frac{[DMAPH^+][Ru^{II}(bpy\text{-}COO^-)]}{[Ru^{II}(bpy\text{-}COOH)][DMAP]}$$

$$pK_{a,Ru^{II}(bpy\text{-}COOH)} = pK_{a,DMAPH^+} - \log(K_{eq})$$

The concentration of [$DMAPH^+$] is equal to [**Ru^{II}(bpy-COO^-)**], thus, plotting [DMAP] vs. [**Ru^{II}(bpy-COO^-)**]^2/[**Ru^{II}(bpy-COOH)**] gives a plot with a slope equal to the equilibrium constant, K_{eq} = 0.11 ± 0.1 (Figure 2.6B). The pK_a of **Ru^{II}(bpy-COOH)** can be determined using equation above and the known pK_a of $DMAPH^+$ (DMAP, $pK_{a,DMAPH^+}$ = 17.95 ± 0.03[15]). The pK_a of **Ru^{II}(bpy-COOH)** is therefore equal to 18.9 ± 0.4.[18]

2.5.5.3 pK_a Determination for Ru^{II}(bpy-Ph-COOH). **Ru^{II}(bpy-Ph-COOH)** was titrated with tetrabutylammonium (Bu_4N^+) *p*-nitrobenzoate, resulting in formation of [Bu_4N^+][**Ru^{II}(bpy-Ph-COO^-)**] and *p*-nitrobenzoic acid in equilibrium. 1- to 5- μL aliquots of a 0.51 M solution of [Bu_4N^+][*p*-nitrobenzoate] were added to a solution of 2 mL of 64 μM **Ru^{II}(bpy-Ph-COOH)** up to a total of 97 equivalents. Changes in the UV-vis spectrum were monitored after each addition at 630 nm (Figure 2.7A). The absorbance values were corrected for volume additions. The concentrations of **Ru^{II}(bpy-Ph-COOH)** and [**Ru^{II}(bpy-Ph-COO^-)**] were calculated using the equations analogous to those used in the **Ru^{II}(bpy-COOH)** titration. The concentration of *p*-

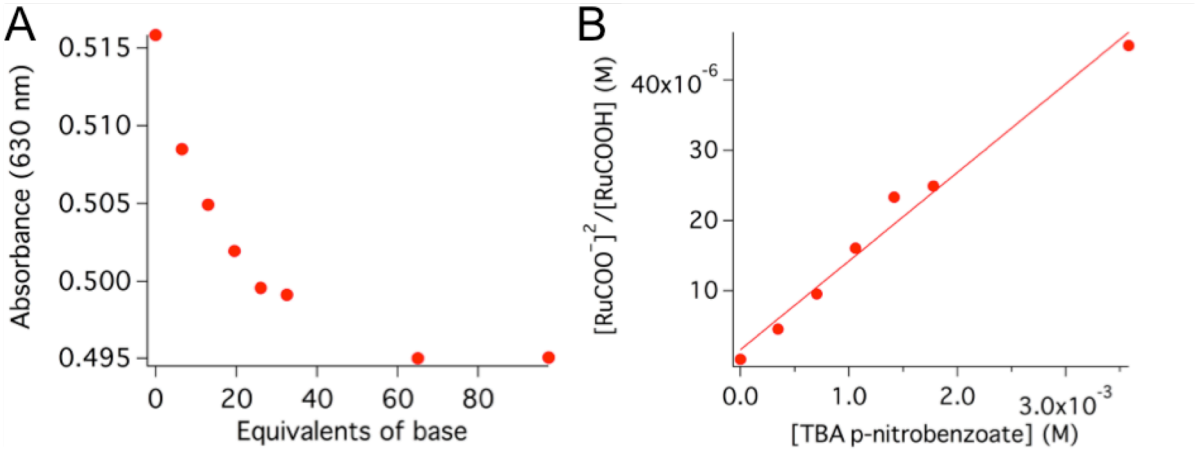

Figure 2.7A. Change in UV-vis absorbance at 630 nm upon addition of $[Bu_4N^+][p$-nitrobenzoate] to **Ru^{II}(bpy-Ph-COOH)**. **Figure 2.7B.** Plot of [**Ru^{II}(bpy-Ph-COO^-)**$]^2$/[**Ru^{II}(bpy-Ph-COOH)**] vs. $[[Bu_4N^+][p$-nitrobenzoate]].

nitrobenzoic acid is equal to $[Bu_4N^+]$[**Ru^{II}(bpy-COO^-)**], thus, plotting $[Bu_4N^+][p$-nitrobenzoate] vs. [**Ru^{II}(bpy-Ph-COO^-)**$]^2$/[**Ru^{II}(bpy-Ph-COOH)**] gives a plot with a slope equal to the equilibrium constant, K_{eq} = 0.013 ± 0.007 (Figure 2.7B). The pK_a of **Ru^{II}(bpy-Ph-COOH)** can be determined using equation above and the known pK_a of *p*-nitrobenzoic acid (pK_a = 19.0 ± 0.1[15]). The pK_a of **Ru^{II}(bpy-Ph-COOH)** is therefore equal to 20.9 ± 0.2.

2.5.5.4 Electrochemical Measurements. All cyclic voltamograms (CVs) were collected in MeCN using 0.1 M tetrabutylammonium hexafluorophosphate as the supporting electrolyte. CVs were collected using a 3 mm diameter glassy carbon working electrode, a platinum wire auxiliary electrode, and a $Ag/AgNO_3$ (0.01 M in acetonitrile) reference electrode. CVs of ferrocene (Fc) provided calibration of the $Ag/AgNO_3$ electrode and potentials are reported vs. $Fc^{+/0}$.

Notes to Chapter 2

(1) Weinberg, D. R.; Gagliardi, C. J.; Hull, J. F.; Murphy, C. F.; Kent, C. A.; Westlake, B. C.; Paul, A.; Ess, D. H.; McCafferty, D. G.; Meyer, T. J. *Chem. Rev.* **2012**, *112*, 4016-4093.

(2) Costentin, C.; Evans, D.; Robert, M.; Saveant, J.; Singh, P. *J. Am. Chem. Soc.* **2005**, *127*, 12490-12491.

(3) Warren, J. J.; Tronic, T. A.; Mayer, J. M. *Chem. Rev.* **2010**, *110*, 6961-7001.

(4) Manner, V. W. Concerted Proton-Electron Transfer Reactions of Ruthenium and Cobalt Complexes: Studies on Distance Dependence and Spin Effects. PhD, University of Washington, Seattle, WA, 2009.

(5) Manner, V. W.; DiPasquale, A. G.; Mayer, J. M. *J. Am. Chem. Soc.* **2008**, *130*, 7210-7211.

(6) Manner, V. W.; Mayer, J. M. *J. Am. Chem. Soc.* **2009**, *131*, 9874-9875.

(7) Wu, A.; Masland, J.; Swartz, R. D.; Kaminsky, W.; Mayer, J. M. *Inorg. Chem.* **2007**, *46*, 11190-11201.

(8) Izutsu, K.; International Union of Pure and Applied Chemistry. Commission on Electroanalytical Chemistry. *Acid-base dissociation constants in dipolar aprotic solvents*; Blackwell Scientific Publications; Distributors, USA, Publishers' Business Services: Oxford; Boston Brookline Village, Mass., 1990.

(9) Warren, J. J.; Menzeleev, A. R.; Kretchmer, J. S.; Miller, T. F.; Gray, H. B.; Mayer, J. M. *J. Phys. Chem. Lett.* **2013**, *4*, 519-523.

(10) Harrisson, P.; Morris, J.; Steel, P. G.; Marder, T. B. *Synlett* **2009**, 147-150.

(11) Panetta, C.; Kumpaty, H.; Heimer, N.; Leavy, M.; Hussey, C. *J. Org. Chem.* **1999**, *64*, 1015-1021.

(12) In a control experiment in which [Ru(III)(acac)$_2$(MeCN)$_2$][OTf] was heated to 40 degrees Celsius in DMF-d_7, coordination of DMF-d_7 to the Ru(III) was observed. Therefore, the non-coordinating solvent CD_2Cl_2 was used for reactions with the Ru(III) starting material.

(13) Sheldrick, G. M. SHELXL-97: Program for the Refinement of Crystal Structures 1997 University of Gottingen, Germany.

(14) Bruker (2007) APEX2 (Version 2.1-4), SAINT (version 7.34A), SADABS (version 2007/4), BrukerAXS Inc, Madison, Wisconsin, USA.

(15) (a) Altomare, A.; Burla, C.; Camalli M.; Cascarano L.; Giacovazzo C.; Guagliardi A.; Moliterni A.G.G.; Polidori G.; Spagna R. *J. Appl. Cryst.* **1999**, *32*, 115-119; (b) Altomare, A., Cascarano, G., Giacovazzo, C., Guagliardi, A., *J. Appl. Cryst.* **1993**, *26*, 343.

(16) Mackay, S.; Edwards, C.; Henderson, A.; Gilmore, C.; Stewart, N.; Shankland, K.; Donald, A.; MaXus: a computer program for the solution and refinement of crystal structures from diffraction data. University of Glasgow, Scotland, 1997.

(17) Waasmaier, D.; Kirfel, A. *Acta Crystallographica Section A* **1995**, *51*, 416-431.

(18) The estimated uncertainty is based on differences in experimentally determined p*K*a values from titrations on different days.

Chapter 3

Proton-Coupled Electron Transfer Reactivity of Ruthenium-Bipyridine Complexes with Distant Carboxylic Acids

3.1 Introduction

Long distance electron transfer (ET) events are essential to the function of many photochemical charge-separation devices as well as biological systems, and they have been studied extensively.[1-5] Short distance proton transfer (PT) events have been shown in some cases to have a significant effect on the rates of long distance ET steps.[6-21] ET occurring over > 10 Å distances can be coupled to short-distance proton transfers in biological systems including ribonucleotide reductase[6,7] and photosystem II.[8-10] In photosystem II, the oxidation of tyrosine Z by a photo-oxidized chlorophyll, $P680^{\bullet+}$, occurs over 14 Å, and is coupled to a proton transfer from tyrosine Z to a nearby hydrogen-bonded histidine. A variety of models for this type of bidirectional proton-coupled phenol oxidation have been studied using different ligand frameworks to vary the distance and type of molecular bridge between the phenol (electron donor) and the photo-oxidant (electron acceptor).[11-14]

Long distance ET through hydrogen bonded interfaces has also been well studied.[15,16] For example, aminidinium-carboxylate salt bridges in Nocera's ruthenium bipyridine system can significantly mediate intramolecular electron transfers.[16] More recently, the effect of hydrogen-bonded interfaces on ET in dye-sensitized solar cells (DSSCs) has been investigated.[17-21] Ruthenium complexes have been studied extensively as photosensitizers for DSSCs and have shown some of the best photovoltaic properties.[22] Many of these complexes have polypyridine

ligands with carboxylate groups in the 4′-position, which can be anchored to TiO_2 surfaces through the carboxylate groups.[22] In some of these systems, the electron injection yields have been shown to be dependent on the pH, the protonation state of the carboxylate groups in the 4′-position, or protonation of the TiO_2 surface.[17-21]

In these PCET reactions, the ET distance is much larger than the PT distance. Consequently, the electron transfers to a distant site (at least several bonds away) from the proton, or alternatively the electron transfers to the vicinity of the proton from a distant site. The PT site could also be positioned at some point along the ET pathway, as is the case for ET through hydrogen bonded interfaces and proton content at the interface of ruthenium dyes and TiO_2 in DSSCs. The interaction or communication between the PT and ET sites is referred to herein as thermochemical coupling.[23] The PCET studies referenced above suggest that the electron and proton have some thermochemical coupling despite being separated by long distances.

The synthesis and characterization of the ruthenium bipyridine complexes, **Ru^{II}(bpy-COOH)** and **Ru^{II}(bpy-Ph-COOH)**, were described in Chapter 2. In reactions with hydrogen atom acceptors, the ruthenium complexes lose one electron from the ruthenium center to form Ru(III) and lose one proton from the distant carboxylic acid (Scheme 3.1). In order to study the effect of the separation of the electron and proton transfer sites on PCET reactivity, the reactions of **Ru^{II}(bpy-COOH)** and **Ru^{II}(bpy-Ph-COOH)** with various hydrogen atom acceptors were investigated. The deprotonated complex, **[Bu_4N^+][Ru^{II}(bpy-COO^-)]**, which was characterized by X-ray crystallography, has a distance between the ruthenium center and either of the

$$\mathbf{BDFE(O\text{-}H) = 1.37p}K_a \mathbf{+ 23.06}E_{1/2} + C_G \qquad \mathbf{(3.1)}$$

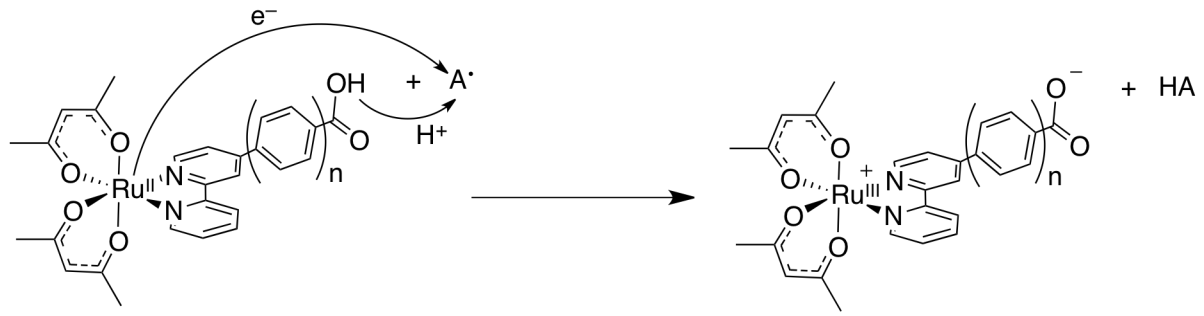

Scheme 3.1. Reaction of **Ru^{II}(bpy-COOH)** (n = 0) and **Ru^{II}(bpy-Ph-COOH)** (n = 1) with hydrogen atom acceptor (A$^{\bullet}$).

carboxylate oxygen atoms of 7.0 Å. For **Ru^{II}(bpy-Ph-COOH)**, this distance is approximately 11 Å, based on the structure of a similar complex, $Ru^{II}(tpy\text{-}Ph\text{-}COO^{-})_2$.[24]

3.2 Results

3.2.1 Calculated Bond Dissociation Free Energies of Ruthenium Complexes. The effective O-H bond dissociation energy (BDFE(O-H)) of **Ru^{II}(bpy-COOH)** and **Ru^{II}(bpy-Ph-COOH)**, where the electron is lost from the ruthenium center and the proton is lost from the carboxylic acid, can be determined from the carboxylic acid pK_a and the $Ru^{III/II}$ $E_{1/2}$ of the deprotonated complex according to Equation 3.1 (also see Scheme 3.2).[23] C_G is the $H^+/H^{\bullet}$ standard reduction potential in the solvent of interest, in this case acetonitrile (C_G = 54.9 kcal mol^{-1}).[23] The pK_a values of the carboxylic acid of **Ru^{II}(bpy-COOH)** and **Ru^{II}(bpy-Ph-COOH)** were determined by titrating the ruthenium complex with an appropriate base and monitoring the changes in the UV-vis spectra. The pK_a values in acetonitrile for **Ru^{II}(bpy-COOH)** and **Ru^{II}(bpy-Ph-COOH)** were found to be 18.9 ± 0.4 and 20.9 ± 0.2, respectively. The $E_{1/2}$ values of the $Ru^{III/II}$ couple for each of the deprotonated complexes was determined by cyclic voltammetry. In acetonitrile, the $E_{1/2}$ values are -0.49 ± 0.02 V vs. $Cp_2Fe^{+/0}$ for both **Ru^{II}(bpy-COO^{-})** and **Ru^{II}(bpy-Ph-COO^{-})**.

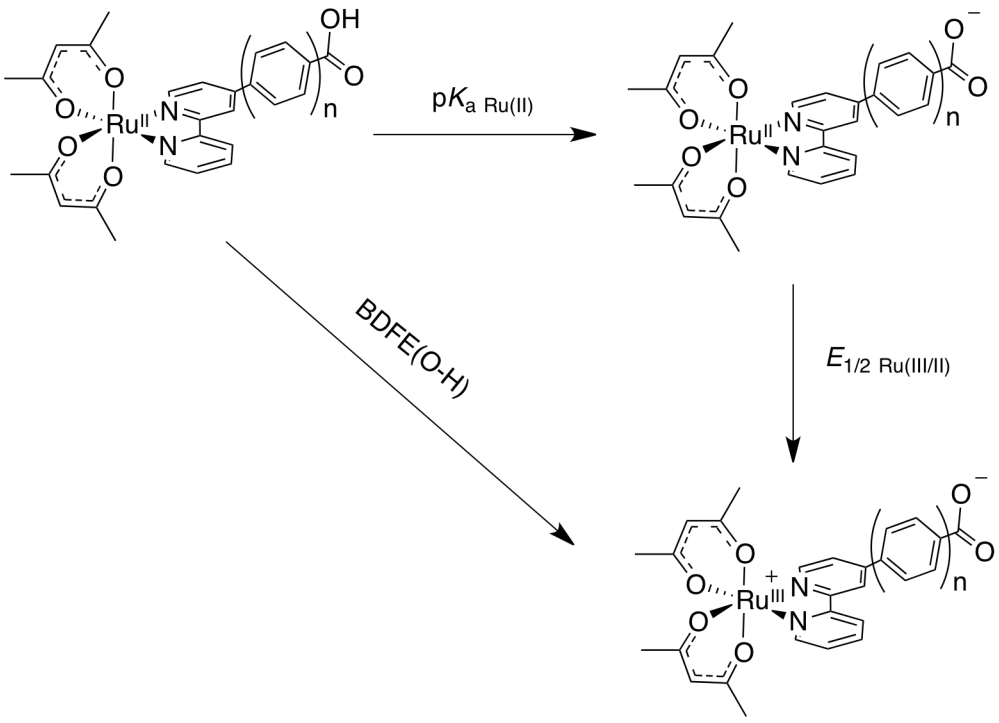

Scheme 3.2. Components of the effective BDFE(O-H) of **Ru^{II}(bpy-COOH)** (n = 0) and **Ru^{II}(bpy-Ph-COOH)** (n = 1).

Using Equation 3.1, the effective BDFE(O-H) values in acetonitrile for **Ru^{II}(bpy-COOH)** and **Ru^{II}(bpy-Ph-COOH)** are 69.5 ± 1.0 kcal mol^{-1} and 72.2 ± 1.0 kcal mol^{-1}, respectively. The larger pK_a of the carboxylic acid in the more separated **Ru^{II}(bpy-Ph-COOH)** results in a 2.7 ± 1.4 kcal mol^{-1} increase in the BDFE(O-H) compared to **Ru^{II}(bpy-COOH)**.

3.2.2 Calculated PCET Driving Forces of Reactions of Ruthenium Complexes (Ru~COOH) with Hydrogen Atom Acceptors. As described below, ^{t}Bu$_3$ArO$^{\bullet}$ removes one electron and one proton from **Ru^{II}~COOH** to give tri-*tert*-butylphenol (^{t}Bu$_3$ArOH) and the zwitterionic neutral complex, **Ru^{III}~COO^{-}** (Scheme 3.3, R = ^{t}Bu). ^{t}Bu$_3$ArO$^{\bullet}$ is a hydrogen atom acceptor with a BDFE(O-H) in acetonitrile of 77.1 kcal mol^{-1}.[23] Based on the BDFE(O-H) values of **Ru^{II}(bpy-**

COOH), Ru^{II}(bpy-COOH) and $^{t}Bu_3ArOH$, the free energy (ΔG^{o}_{PCET}) of the reaction of **Ru^{II}(bpy-COOH)** and $^{t}Bu_3ArO^{\bullet}$ is -7.6 ± 1 kcal mol^{-1}, and the ΔG^{o}_{PCET} of the reaction of **Ru^{II}(bpy-Ph-COOH)** and $^{t}Bu_3ArO^{\bullet}$ is -4.9 ± 1 kcal mol^{-1}.

$^{t}Bu_2OMeArO^{\bullet}$ reacts with the **Ru^{II}~COOH** complexes in a reaction analogous to that with $^{t}Bu_3ArO^{\bullet}$ (Scheme 3.3, R = OMe). $^{t}Bu_2OMeArO^{\bullet}$ is a weaker hydrogen atom abstractor than $^{t}Bu_3ArO^{\bullet}$ and the BDFE(O-H) of $^{t}Bu_2OMeArO^{\bullet}$ in acetonitrile is 74.4 kcal mol^{-1}.[23] Based on this BDFE(O-H) value, ΔG^{o}_{PCET} = -4.9 ± 1 kcal mol^{-1} for the reaction of **Ru^{II}(bpy-COOH)** with $^{t}Bu_2OMeArO^{\bullet}$. The BDFE(O-H) of $^{t}Bu_2OMeArOH$ is larger than the BDFE(O-H) of **Ru^{II}(bpy-Ph-COOH)** by only 2.2 kcal mol^{-1}, so the reaction of **Ru^{II}(bpy-Ph-COOH)** with $^{t}Bu_2OMeArO^{\bullet}$ approaches equilibrium. The ΔG^{o}_{PCET} can be determined from the experimentally measured equilibrium constant for this reaction (see Sections 3.2.3.2 and 3.2.4.2).

TEMPOH is a good hydrogen atom donor with a relatively weak BDFE(O-H) of 66.5 kcal mol^{-1}.[23] The reactions of **Ru^{II}(bpy-COOH)** and **Ru^{II}(bpy-Ph-COOH)** with $TEMPO^{\bullet}$ are both uphill (ΔG^{o}_{PCET} = +3.0 ± 1 kcal mol^{-1} and +5.7 ± 1 kcal mol^{-1}, respectively, calculated from BDFE(O-H)). The ΔG^{o}_{PCET} values for these reactions can be determined from the experimentally measured equilibrium constants if a large excess of $TEMPO^{\bullet}$ is used (see Section 3.2.6).

3.2.3 Monitoring Reactions of Ruthenium Complexes (Ru^{II}~COOH) with Phenoxyl Radicals using ^{1}H-NMR Spectroscopy. The reactions of **Ru^{II}(bpy-COOH)** and **Ru^{II}(bpy-Ph-COOH)** with 2,4,6-tri-*tert*-butylphenoxyl radical (Scheme 3.3, R = ^{t}Bu) and 2,6-di-*tert*-butyl-4-methoxyphenoxyl radical (Scheme 3.3, R = OMe) were monitored by ^{1}H-NMR spectroscopy. A ^{1}H-NMR spectrum of a solution of either **Ru^{II}(bpy-COOH)** or **Ru^{II}(bpy-Ph-COOH)** in MeCN-d_3 under dry nitrogen was obtained. Solutions of either phenoxyl radical were added to the

ruthenium complex solution in MeCN-d_3 under dry nitrogen, and the resulting changes in the ^{1}H-NMR spectrum were analyzed. The yields of the reactions were determined by integrating the phenol product signals versus an internal standard.

3.2.3.1 Reactions of Ru^{II}~COOH with $^tBu_3ArO^\bullet$. Addition of $^tBu_3ArO^\bullet$ to a solution of **Ru^{II}(bpy-COOH)** in MeCN-d_3 results in an immediate color change from green to pink. The ^{1}H-NMR spectrum of the reaction products shows the loss of the diamagnetic **Ru^{II}(bpy-COOH)** signals and formation of a broad, paramagnetic signal for **Ru^{III}(bpy-COO)** upfield at -22 ppm.[25,26] This agrees with the ^{1}H-NMR spectrum of independently synthesized **Ru^{III}(bpy-COO)** (see Section 2.5.3.6 for details). $^tBu_3ArOH$ is formed in 100% yield. Similar results were observed for the analogous reaction of **Ru^{II}(bpy-Ph-COOH)** with $^tBu_3ArO^\bullet$. Upon addition of $^tBu_3ArO^\bullet$, the color changes from dark blue-green to orange. The ^{1}H-NMR spectrum reveals the loss of the diamagnetic signals for **Ru^{II}(bpy-Ph-COOH)** and formation of a broad, paramagnetic signal for **Ru^{III}(bpy-Ph-COO)** at -21 ppm. $^tBu_3ArOH$ is formed in 100% yield. The ΔG^o_{PCET} of the reactions of **Ru^{II}(bpy-COOH)** and **Ru^{II}(bpy-Ph-COOH)** with $^tBu_3ArO^\bullet$ are -7.6 ± 1 kcal mol^{-1} and -4.9 ± 1 kcal mol^{-1}, respectively (as calculated from the BDFE(O-H) values, see Section 3.2.2). These ΔG^o_{PCET} values agree with the measured 100% yields of the reactions, given the reaction conditions (see Section 3.5.4).

3.2.3.2 Reactions of Ru^{II}~COOH with $^tBu_2OMeArO^\bullet$. The ^{1}H-NMR spectra show changes similar to those observed for the $^tBu_3ArO^\bullet$ reactions. The diamagnetic Ru(II) signals are lost and a broad paramagnetic signal is formed upfield for Ru(III). The yields of $^tBu_2OMeArOH$ for the reactions of **Ru^{II}(bpy-COOH)** and **Ru^{II}(bpy-Ph-COOH)** are 100% and 80% as indicated by

integrations of the ^{t}Bu$_2$OMeArOH ^{1}H-NMR signals. Considering the ΔG^{o}_{PCET} = -4.9 ± 1 kcal mol^{-1} for the reaction of **Ru^{II}(bpy-COOH)** with ^{t}Bu$_2$OMeArO$^{\bullet}$ (as calculated from the BDFE(O-H) values, see Section 3.2.2), the reaction conditions are sufficient to achieve a 100% yield of products (see Section 3.5.4). The reaction of **Ru^{II}(bpy-Ph-COOH)** with ^{t}Bu$_2$OMeArO$^{\bullet}$ approaches equilibrium (ΔG^{o}_{PCET} = -2.2 ± 1 kcal mol^{-1}, as calculated from the BDFE(O-H) values), and the 3.4 equivalents of ^{t}Bu$_2$OMeArO$^{\bullet}$ added to the **Ru^{II}(bpy-Ph-COOH)** are therefore not sufficient to achieve 100% yields. The equilibrium constant of this reaction calculated from the initial concentrations of reactants and the final yield of products is K_{eq} = 1.2 ± 0.7 (using a mass balance assumption where [^{t}Bu$_2$OMeArOH] = [**Ru^{III}(bpy-Ph-COO)**], see Section 3.5.4.4 for details). The equilibrium constant was also determined by measuring the changes in the UV-vis spectrum upon titration of **Ru^{II}(bpy-Ph-COOH)** with ^{t}Bu$_2$OMeArO$^{\bullet}$ (see Section 3.2.4.2). These techniques will be compared and discussed in Section 3.2.4.2.

3.2.4 Monitoring Reactions of Ruthenium Complexes (Ru^{II}~COOH) with Phenoxyl Radicals using UV-vis Spectroscopy.

3.2.4.1 Reactions of Ru^{II}~COOH with ^{t}Bu$_3$ArO$^{\bullet}$. Ru^{II}(bpy-COOH) was titrated with ^{t}Bu$_3$ArO$^{\bullet}$ and the changes in the UV-vis spectra were monitored (Figure 3.1A). Addition of ^{t}Bu$_3$ArO$^{\bullet}$ results in a loss of the MLCT bands of **Ru^{II}(bpy-COOH)** at 410 nm and 630 nm and formation of a new band at 524 nm. A band at 524 nm is also observed in the UV-vis spectrum of **Ru^{III}(bpy-COO)** independently synthesized from [Ru^{III}(acac)$_2$(MeCN)$_2$][OTf] and bpy-COO^{-}K^{+} (see Section 2.5.3.6). A plot of the measured absorbance at 635 nm versus equivalents of ^{t}Bu$_3$ArO$^{\bullet}$ added shows that the reaction of **Ru^{II}(bpy-COOH)** with ^{t}Bu$_3$ArO$^{\bullet}$ occurs quantitatively, in agreement with the large negative ΔG^{o}_{PCET} (Figure 3.1B). A titration of

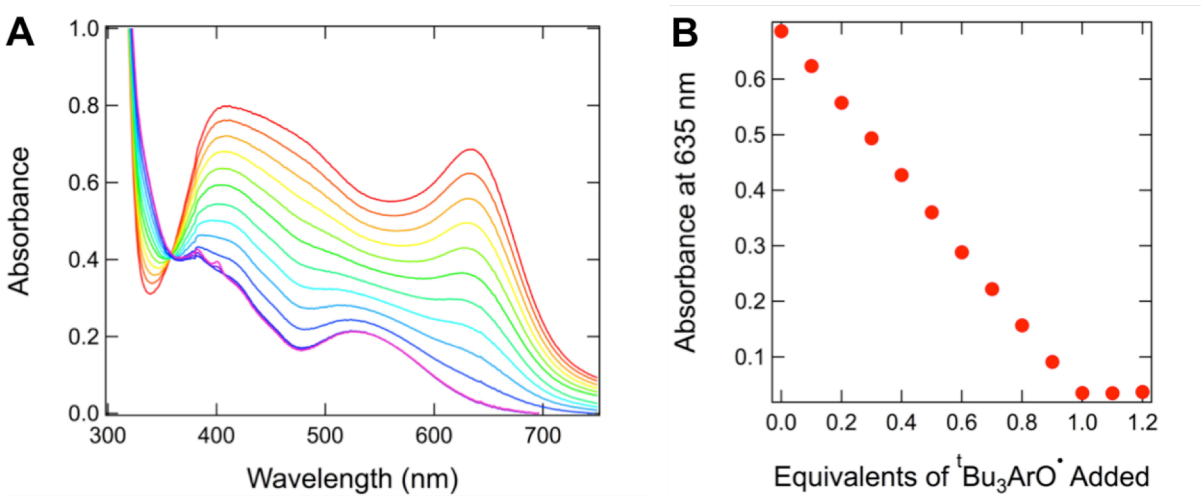

Figure 3.1A. UV-vis spectra of titration of **Ru^{II}(bpy-COOH)** with ^{t}Bu$_3$ArO$^{\bullet}$. **Figure 3.1B.** Plot of absorbance measured at 635 nm versus equivalents of ^{t}Bu$_3$ArO$^{\bullet}$ added.

Ru^{II}(bpy-Ph-COOH) with ^{t}Bu$_3$ArO$^{\bullet}$ was also monitored by UV-vis spectroscopy, and similar results were observed (Figure 3.2). The major transition of the **Ru^{III}(bpy-Ph-COO)** product occurs at a higher wavelength than that of **Ru^{III}(bpy-COO)**.

3.2.4.2 Reactions of Ru^{II}~COOH with ^{t}Bu$_2$OMeArO$^{\bullet}$. Ru^{II}(bpy-COOH) was titrated with ^{t}Bu$_2$OMeArO$^{\bullet}$ and the changes in the UV-vis spectra were monitored (Figure 3.3A). The spectral changes are very similar to those observed for the reaction of **Ru^{II}(bpy-COOH)** and ^{t}Bu$_3$ArO$^{\bullet}$. A plot of the absorbance at 635 nm versus the equivalents of ^{t}Bu$_2$OMeArO$^{\bullet}$ added shows that the reaction of **Ru^{II}(bpy-COOH)** and ^{t}Bu$_2$OMeArO$^{\bullet}$ is quantitative, in agreement with the ΔG^{o}_{PCET} of -4.9 kcal mol^{-1} (Figure 3.3B).

A titration of **Ru^{II}(bpy-Ph-COOH)** with ^{t}Bu$_2$OMeArO$^{\bullet}$ was also performed and the spectral changes were monitored by UV-vis spectroscopy. The absorbance decreases as **Ru^{II}(bpy-Ph-COOH)** is converted to **Ru^{III}(bpy-Ph-COO)** and it continues to decrease as more than one equivalent of ^{t}Bu$_2$OMeArO$^{\bullet}$ is added, as shown by a plot of the absorbance at 630 nm versus the equivalents of ^{t}Bu$_2$OMeArO$^{\bullet}$ (Figure 3.4). Two possible sources of this result are that either the

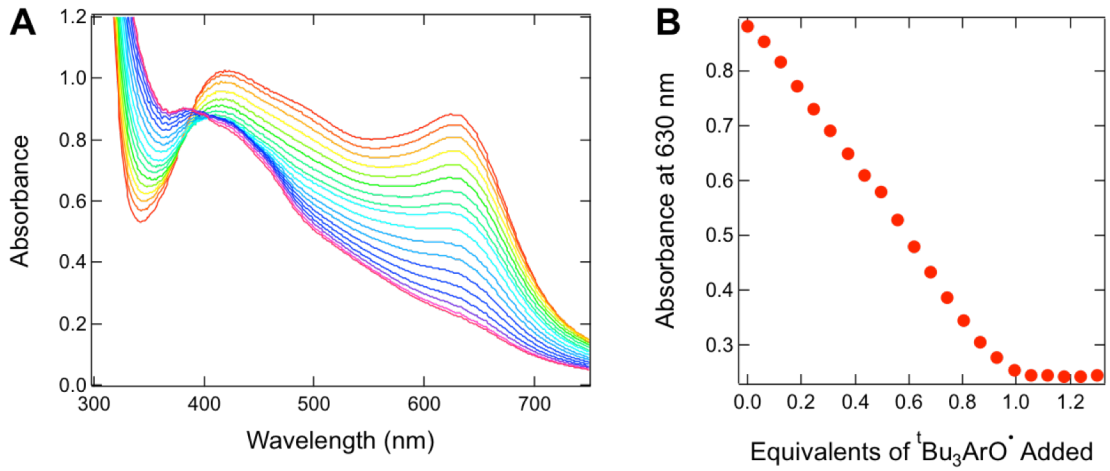

Figure 3.2A. UV-vis spectra of titration of **Ru^{II}(bpy-Ph-COOH)** with ^{t}Bu$_3$ArO$^{\bullet}$. **Figure 3.2B.** Plot of absorbance measured at 630 nm versus equivalents of ^{t}Bu$_3$ArO$^{\bullet}$ added.

reaction of **Ru^{II}(bpy-Ph-COOH)** with ^{t}Bu$_2$OMeArO$^{\bullet}$ approaches equilibrium or some of the ^{t}Bu$_2$OMeArO$^{\bullet}$ is being consumed by a side reaction. Fitting the reaction to the equilibrium equation (Equation 3.10, Figure 3.14A) does not give a linear trend, but instead suggests that some of the ^{t}Bu$_2$OMeArO$^{\bullet}$ is consumed by another route (due to the small changes in concentration with added ^{t}Bu$_2$OMeArO$^{\bullet}$ at the beginning of the titration). The equilibrium constant from this fit is K_{eq} = 4.5 ± 0.5. Alternatively, by assuming the first 20 μL of ^{t}Bu$_2$OMeArO$^{\bullet}$ added is consumed by another route, such as oxygen that has leaked into the cuvette, and adjusting the concentration of ^{t}Bu$_2$OMeArO$^{\bullet}$ to account for this, a linear fit to the equilibrium equation can be obtained (Figure 3.14B). A K_{eq} of 3.1 ± 0.2 was determined from a linear fit to this plot. Accounting for the initial reaction of ^{t}Bu$_2$OMeArO$^{\bullet}$, possibly with oxygen, results in an experimental equilibrium constant in better agreement with the equilibrium constant determined by ^{1}H-NMR spectroscopy. Taking the average of the equilibrium constants determined from the ^{1}H-NMR (K_{eq} = 1.2) and UV-vis spectroscopy, K_{eq} = 2.9 ± 1.7 (ΔG^{o}_{PCET} = −0.63 ± 0.5 kcal mol^{-1}) for the reaction of **Ru^{II}(bpy-Ph-COOH)** with ^{t}Bu$_2$OMeArO$^{\bullet}$.

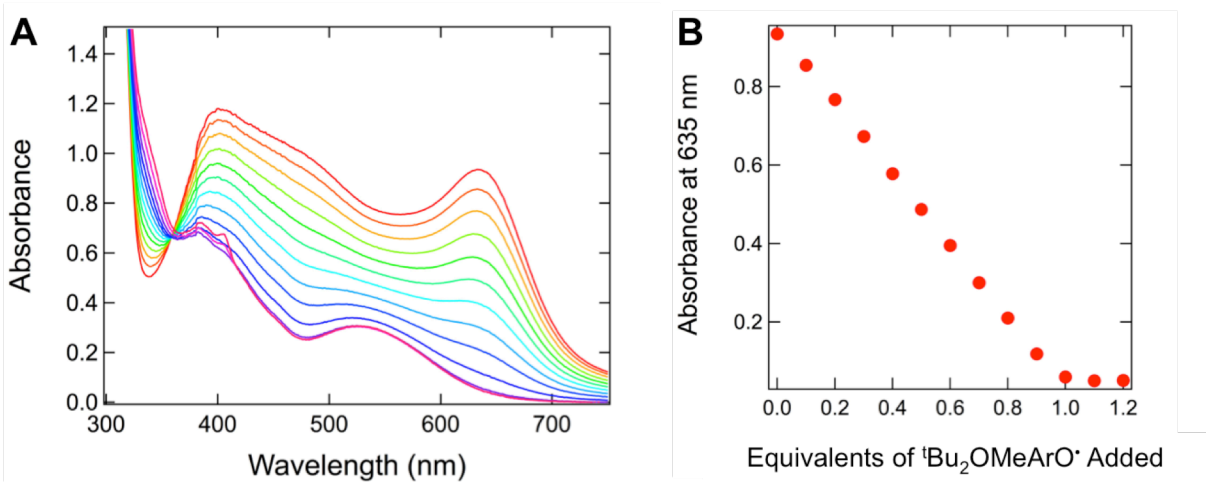

Figure 3.3A. UV-vis spectra of titration of **Ru^{II}(bpy-COOH)** with $^{t}Bu_2OMeArO^{\bullet}$. **Figure 3.3B.** Plot of absorbance measured at 635 nm versus equivalents of $^{t}Bu_2OMeArO^{\bullet}$ added.

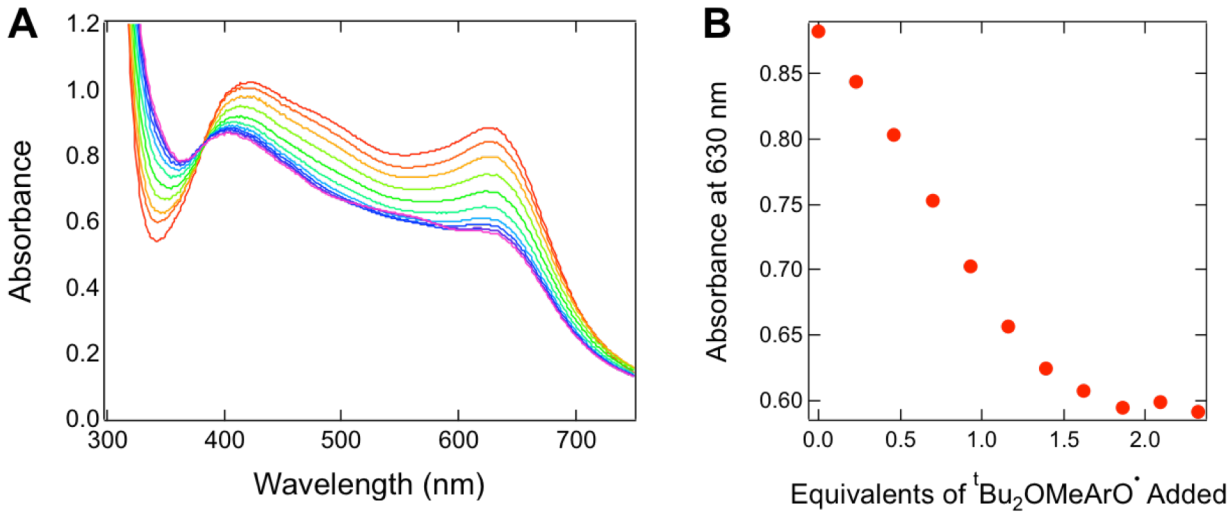

Figure 3.4A. UV-vis spectra of titration of **Ru^{II}(bpy-Ph-COOH)** with $^{t}Bu_2OMeArO^{\bullet}$. **Figure 3.4B.** Plot of absorbance measured at 630 nm versus equivalents of $^{t}Bu_2OMeArO^{\bullet}$ added.

3.2.5 Monitoring Reactions of Ru^{II}~COOH with Phenoxyl Radicals using Stopped-Flow Spectrophotometry. Reactions of **Ru^{II}(bpy-COOH)** and **Ru^{II}(bpy-Ph-COOH)** with phenoxyl radicals were monitored by rapid-scanning stopped-flow spectrophotometry at 25 ºC (unless otherwise specified). Reaction rate constants were determined by fitting the spectral changes to either a first-order, second-order, or second-order equilibrium reaction model using Specfit™ global fitting software.

3.2.5.1 Pseudo-First Order Kinetics of Reactions of Ru^{II}~COOH with Phenoxyl Radicals. Reactions of **Ru^{II}(bpy-COOH)** and **Ru^{II}(bpy-Ph-COOH)** with phenoxyl radicals were monitored under pseudo-first order conditions with varying concentrations of phenoxyl radical in greater than 10-fold excess. Plots of the pseudo first-order rate constants versus the concentration of phenoxyl radical show linear correlations, indicating that the reactions are first order in

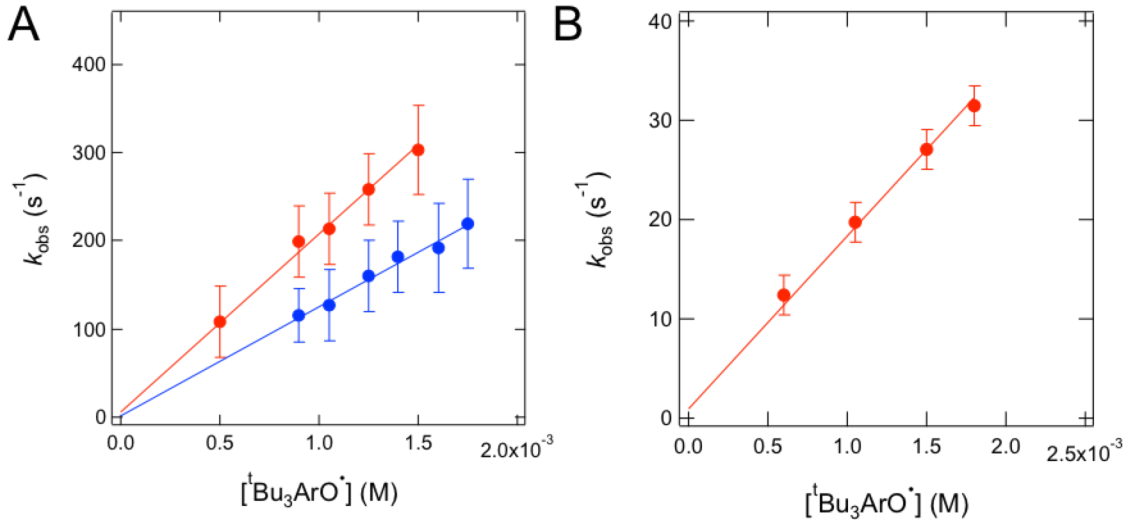

Figure 3.5A. Pseudo first-order rate constants, k_{obs}, of the reaction of **Ru^{II}(bpy-COOH)** in acetonitrile with no added methanol (red dots) and **Ru^{II}(bpy-COOD)** in acetonitrile with 0.2% MeOD (blue dots) with $^tBu_3ArO^\bullet$ versus concentration of $^tBu_3ArO^\bullet$. **Figure 3.5B.** Pseudo first-order rate constants, k_{obs}, of the reaction of **Ru^{II}(bpy-Ph-COOH)** with $^tBu_3ArO^\bullet$ versus concentration of $^tBu_3ArO^\bullet$.

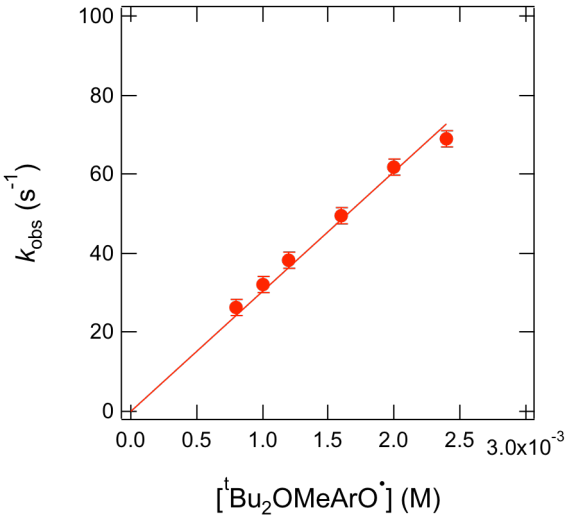

Figure 3.6. Pseudo first-order rate constants, k_{obs}, of the reaction of **Ru^{II}(bpy-COOH)** with ^{t}Bu$_2$OMeArO$^\bullet$ versus concentration of ^{t}Bu$_2$OMeArO$^\bullet$.

phenoxyl radical (Figures 3.5, 3.6). The second order rate constant for each reaction was determined from the slope of a linear fit (y = mx + b) of the pseudo first-order rate constants versus the phenoxyl radical concentration and are reported in Table 3.1. Control experiments were performed to determine whether any of the reactants undergo first-order decay reactions (see Section 3.5.6.1). All reactants were stable on the time-scale of the experiments, so a (0, 0) point (at [^{t}Bu$_3$ArO$^\bullet$] = 0 where k_{obs} = 0) was included in each pseudo first-order data set. The y-intercepts (b) were between 1 and 5 s^{-1}; see Table 3.11. The reported error includes second-order rate constants determined by fitting to y = mx + b with and without the (0, 0) point, as well as fitting to y = mx.

3.2.5.2 Pseudo-First Order Kinetics of the Reaction of Ru^{II}(bpy-COOD) with ^{t}Bu$_3$ArO$^\bullet$. To measure the rate constant of the reaction of **Ru^{II}(bpy-COOD)** with ^{t}Bu$_3$ArO$^\bullet$, acetonitrile with 0.2% MeOD was used as the solvent. This concentration of MeOD is sufficient to exchange all

of the carboxylic acid protons of **Ru^{II}(bpy-COOH)**, as confirmed by the loss of the carboxylic acid proton signals in the ^{1}H-NMR spectrum of **Ru^{II}(bpy-COOH)** in MeCN-d_3 with 0.2% MeOD-d_4. A kinetic isotope effect (KIE) of 1.7 ± 0.6 was determined from the second-order rate constants for the reactions of **Ru^{II}(bpy-COOH)** and **Ru^{II}(bpy-COOD)** with ^{t}Bu$_3$ArO$^\bullet$ (Table 3.1, Figure 3.5A). This small normal KIE indicates that proton transfer is involved in the rate determining step (RDS). The large error associated with the rate constants results in large part from variations in the experimentally determined rate constant from one day to another. Therefore, to directly test the effect of replacing a proton with deuterium, the reactions were run under identical conditions on the same day in acetonitrile with or without 0.2% MeOD (see Section 3.2.5.3). This is particularly important for determining KIE for reactions with **Ru^{II}(bpy-Ph-COOH)**, which has very similar rate constants for the reactions involving either a carboxylic acid proton or deuterium.

Table 3.1. Second-order rate constants for reactions of **Ru^{II}~(COOH)** with phenoxyl radicals determined from plots of pseudo first-order rate constants versus phenoxyl radical concentration (Figures 3.5, 3.6).

Reaction	**Rate Constant, k_2 (M^{-1} s^{-1})**	**Activation Energy, $\Delta G^{\ddagger}$ (kcal mol^{-1})**
Ru^{II}(bpy-COOH) + ^{t}Bu$_3$ArO$^\bullet$	2.0 ± 0.4 × 10^5	10.2 ± 0.2
Ru^{II}(bpy-COOD) + ^{t}Bu$_3$ArO$^\bullet$	1.2 ± 0.4 × 10^5	10.5 ± 0.2
Ru^{II}(bpy-Ph-COOH) + ^{t}Bu$_3$ArO$^\bullet$	1.7 ± 0.4 × 10^4	11.7 ± 0.2
Ru^{II}(bpy-COOH) + ^{t}Bu$_2$OMeArO$^\bullet$	2.9 ± 1.0 × 10^4	11.4 ± 0.2

3.2.5.3 Determination of Kinetic Isotope Effects of Reactions of Ru^{II}~COOH with Phenoxyl Radicals. Reactions of **Ru^{II}(bpy-COOH)** and **Ru^{II}(bpy-Ph-COOH)** with phenoxyl radicals were monitored under second-order conditions. To measure the KIE of **Ru^{II}(bpy-COOH)** reactions, acetonitrile with or without 0.2% MeOD was used as the solvent. Additionally, reactions were monitored in 0.2% MeOH to determine whether methanol has an effect on the rate constants. The reactions of **Ru^{II}(bpy-Ph-COOH)** with phenoxyl radicals in acetonitrile without added methanol, with 0.2% MeOH, and with 0.2% MeOD have very similar rate constants. To directly measure these small differences in rate constants, reactions in acetonitrile without added methanol, with 0.2% MeOH, and with 0.2% MeOD were all monitored on the same day in that order. Second-order rate constants were determined by fitting spectral traces to a second-order reaction model, with the exception of the reaction of **Ru^{II}(bpy-Ph-COOH)** with $^{t}Bu_2OMeArO^{\bullet}$ which approaches equilibrium (Table 3.2). For this reaction, the spectral changes were fit to a second-order equilibrium reaction model where the ratio of the forward and reverse reactions, k_2/k_{-2}, was set to the experimentally measured equilibrium constant, K_{eq} = 2.9 (see Section 3.2.4.2 above). The second-order rate constants for each reaction in acetonitrile with no added methanol or 0.2% MeOH are the same within the large estimated uncertainty. There is no general trend between the rate constants of the reactions in acetonitrile with no added methanol or in acetonitrile with 0.2% MeOH.

Kinetic isotope effects (KIEs) were determined from the rate constants of the reactions with either 0.2% MeOH or 0.2% MeOD (Table 3.2). Reactions of **Ru^{II}(bpy-COOH)** with phenoxyl radicals give KIEs greater than 1. Additionally, comparison of the spectral changes at a given wavelength show a clear difference in reaction rate between reactions of **Ru^{II}(bpy-COOH)** (in acetonitrile with no added methanol) and **Ru^{II}(bpy-COOD)** (0.2% MeOD, Figure 3.7 and 3.8).

To compare the reactions of **Ru^{II}(bpy-COOH)** in acetonitrile with no added methanol and acetonitrile with 0.2% MeOH, which were performed on different days, the normalized absorbance was calculated and plotted in Figure 3.15, 3.16 (see Sections 3.5.6.2.1, 3.5.6.2.3 for details). The rate constants for reaction of **Ru^{II}(bpy-Ph-COOH)** and **Ru^{II}(bpy-Ph-COOD)** with either phenoxyl radical are the same within the large estimated uncertainty, and thus, the KIEs are 1.1 ± 0.4 and 1.1 ± 0.3 for reactions with $^{t}Bu_3ArO^{\bullet}$ and $^{t}Bu_2OMeArO^{\bullet}$, respectively. The stacked spectral changes at a given wavelength are very similar, and clearly show that there is very little difference in rate constants between the reactions of **Ru^{II}(bpy-Ph-COOH)** in either acetonitrile with no added methanol, acetonitrile with 0.2% MeOH, or acetonitrile with 0.2% MeOD (Figures 3.9 and 3.10).

Table 3.2. Second-order rate constants for reactions of **Ru^{II}~(COOH)** with phenoxyl radicals in second-order conditions using acetonitrile with 0.2% MeOH or 0.2% MeOD as the solvent (Figures 3.7-3.10).

Reaction	**Rate Constant, (no MeOH) k_2 (M^{-1} s^{-1})**	**Rate Constant (0.2% MeOH), $k_{2,MeOH}$ (M^{-1} s^{-1})**	**Rate Constant (0.2% MeOD), $k_{2,MeOD}$ (M^{-1} s^{-1})**	**Kinetic Isotope Effect[c], $k_{2,MeOH}/k_{2,MeOD}$**
Ru^{II}(bpy-COOH) + $^{t}Bu_3ArO^{\bullet}$ [a]	$2.5 \pm 0.4 \times 10^5$	$2.8 \pm 1.1 \times 10^5$	$1.6 \pm 0.4 \times 10^5$	1.8 ± 0.7
Ru^{II}(bpy-Ph-COOH) + $^{t}Bu_3ArO^{\bullet}$ [b]	$5.8 \pm 2.0 \times 10^4$	$5.8 \pm 2.0 \times 10^4$	$5.4 \pm 2.0 \times 10^4$	1.1 ± 0.4
Ru^{II}(bpy-COOH) + $^{t}Bu_2OMeArO^{\bullet}$ [a]	$4.2 \pm 1.5 \times 10^4$	$4.0 \pm 1.4 \times 10^4$	$1.7 \pm 0.4 \times 10^4$	2.4 ± 0.8
Ru^{II}(bpy-Ph-COOH) + $^{t}Bu_2OMeArO^{\bullet}$ [b]	$6.5 \pm 2.0 \times 10^2$	$7.2 \pm 1.7 \times 10^2$	$6.3 \pm 1.5 \times 10^2$	1.1 ± 0.3

[a]0.2% MeOH reactions were performed under identical conditions on the different days. [b]0.2% MeOH reactions were performed under identical conditions on the same day.

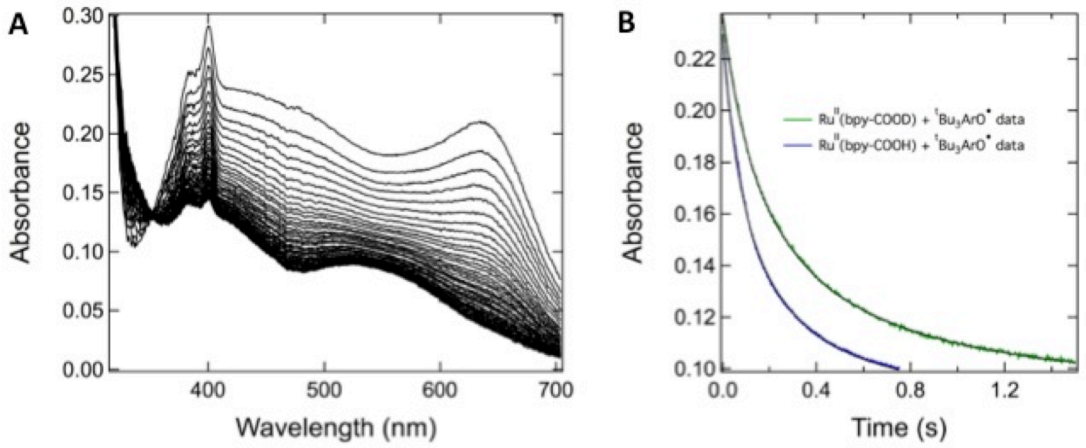

Figure 3.7A. Stacked optical spectra of the reaction of **Ru^{II}(bpy-COOH)** with ^{t}Bu$_3$ArO$^{\bullet}$ in acetonitrile. **Figure 3.7B.** Absorbance at 450 nm versus time of the reactions of **Ru^{II}(bpy-COOH)** with ^{t}Bu$_3$ArO$^{\bullet}$ in acetonitrile (blue line) and **Ru^{II}(bpy-COOD)** with ^{t}Bu$_3$ArO$^{\bullet}$ in acetonitrile with 0.2% MeOD (green line), each superimposed with the second-order fit (black line).

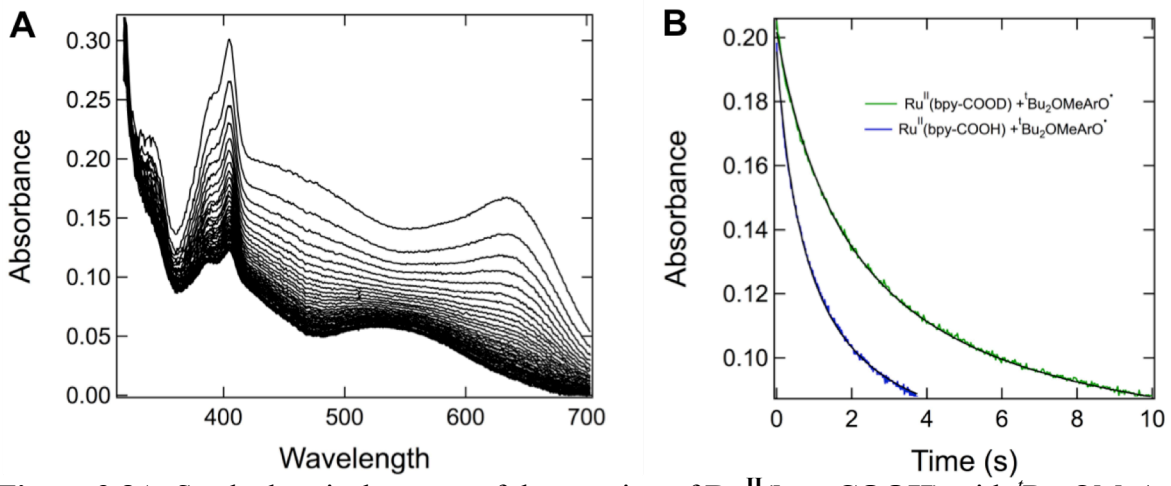

Figure 3.8A. Stacked optical spectra of the reaction of **Ru^{II}(bpy-COOH)** with ^{t}Bu$_2$OMeArO$^{\bullet}$ in acetonitrile. **Figure 3.8B.** Absorbance at 435 nm versus time of the reactions of **Ru^{II}(bpy-COOH)** with ^{t}Bu$_2$OMeArO$^{\bullet}$ in acetonitrile (blue line) and **Ru^{II}(bpy-COOD)** with ^{t}Bu$_2$OMeArO$^{\bullet}$ in acetonitrile with 0.2% MeOD (green line), each superimposed with the second-order fit (black line).

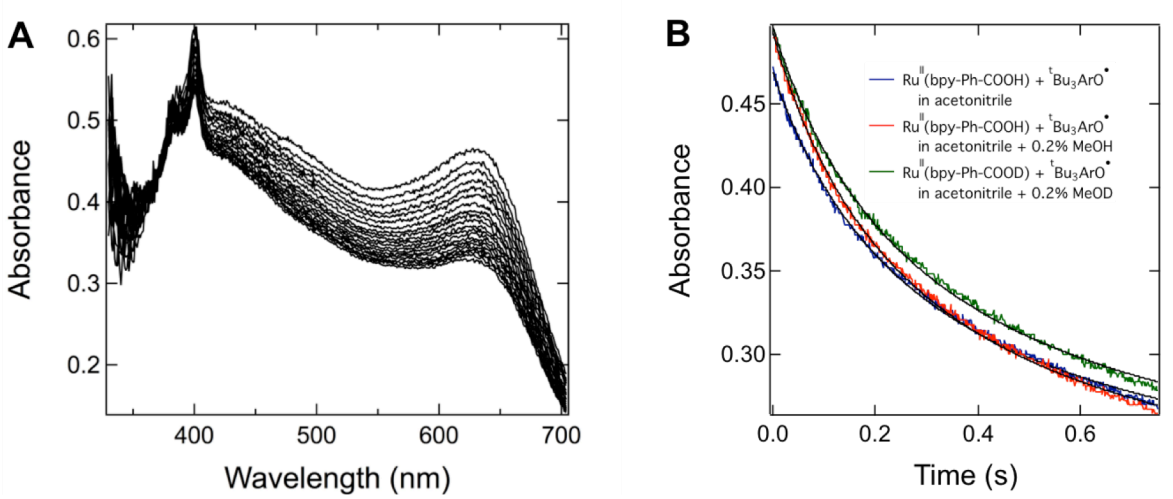

Figure 3.9A. Stacked optical spectra of the reaction of **Ru^{II}(bpy-Ph-COOH)** with $^{t}Bu_3ArO^{\bullet}$ in acetonitrile. **Figure 3.9B.** Absorbance at 630 nm versus time of the reactions of **Ru^{II}(bpy-Ph-COOH)** with $^{t}Bu_3ArO^{\bullet}$ in acetonitrile (blue line), **Ru^{II}(bpy-Ph-COOH)** with $^{t}Bu_3ArO^{\bullet}$ in acetonitrile with 0.2% MeOH (red line), and **Ru^{II}(bpy-COOD)** with $^{t}Bu_3ArO^{\bullet}$ in acetonitrile with 0.2% MeOD (green line), each superimposed with the second-order fit (black line).

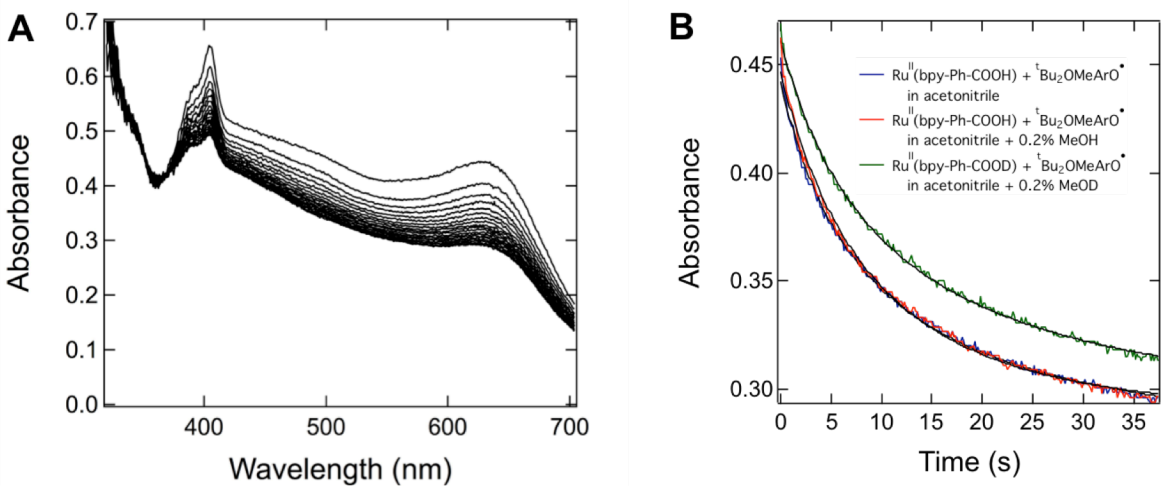

Figure 3.10A. Stacked optical spectra of the reaction of **Ru^{II}(bpy-Ph-COOH)** with $^{t}Bu_2OMeArO^{\bullet}$ in acetonitrile. **Figure 3.10B.** Absorbance at 630 nm versus time of the reactions of **Ru^{II}(bpy-Ph-COOH)** with $^{t}Bu_2OMeArO^{\bullet}$ in acetonitrile (blue line), **Ru^{II}(bpy-Ph-COOH)** with $^{t}Bu_2OMeArO^{\bullet}$ in acetonitrile with 0.2% MeOH (red line), and **Ru^{II}(bpy-Ph-COOD)** with $^{t}Bu_2OMeArO^{\bullet}$ in acetonitrile with 0.2% MeOD (green line), each superimposed with the second-order fit (black line).

3.2.5.4 Comparing Pseudo First-Order and Second-Order Conditions. When fitting the spectral changes of a first order reaction, the initial concentration of the limiting reactant does not need to be accurately known because the half-life is independent of concentration. In contrast, the initial concentration of both reactants in a second-order reaction must be known to achieve accurate fits. Rate constants determined from second-order conditions are therefore more affected by discrepancies between the expected and actual concentrations, and rate constants determined from pseudo first-order fitting are more reliable. One disadvantage, however, of pseudo first order conditions is the possibility of the excess phenoxyl radical participating in interfering side reactions, if present.

To investigate whether excess phenoxyl radical concentrations affected the reaction, the second-order rate constants determined from pseudo first-order and second-order conditions are compared in Table 3.3. For pseudo first-order conditions, the second-order rate constant is determined from the slope of the observed pseudo first-order rate constants versus concentration of excess phenoxyl radical. A slope that is smaller than the true second-order rate constant could be a result of phenoxyl radical concentrations that are smaller than the true concentrations. For example, the actual concentration of the phenoxyl radical stock solution could be larger than the concentration used in the pseudo first-order plots. This an unlikely source of error, however, as it is more likely that the actual concentration of phenoxyl radical would be lower than expected, because phenoxyl radical will decompose if exposed to air. The concentrations of phenoxyl radical solutions were independently measured by UV-vis spectroscopy. Additionally, the concentration of the phenoxyl radical was measured in the stopped-flow apparatus by flushing the stopped-flow lines with the solution of phenoxyl radical and measuring the UV-vis spectrum. Absorbance values measured by these two methods typically did not differ by more than 10%, so

discrepancies in concentration do not explain the large differences in rate constants for the two methods.

Accurate concentrations of reactants must be known to achieve accurate second-order rate constants from second-order fitting. Second-order rate constants and reactant concentrations are inversely related, so a falsely high second-order rate constant could result from a falsely low concentration. For example, the concentration of both **Ru^{II}(bpy-Ph-COOH)** and $^{t}Bu_3ArO^{\bullet}$ would have to be larger by a factor of more than 2 to account for the differences in rate constants measured in the two different conditions. It is unlikely that the actual concentrations of the reactants are higher than the concentrations used when fitting the spectral changes, as the concentrations of both reactants were independently measured by UV-vis spectroscopy as well as by flushing the lines of the stopped-flow and measuring the UV-vis spectrum.

Table 3.3. Second-order rate constants for reactions of **Ru^{II}~(COOH)** with phenoxyl radicals under pseudo first-order or second-order conditions using acetonitrile with no added methanol as the solvent.

Reaction	**Rate Constant, Pseudo First-Order Conditions (M^{-1} s^{-1})**	**Rate Constant, Second-Order Conditions (M^{-1} s^{-1})**
Ru^{II}(bpy-COOH) + $^{t}Bu_3ArO^{\bullet}$	$2.0 \pm 0.4 \times 10^5$	$2.5 \pm 0.4 \times 10^5$
Ru^{II}(bpy-Ph-COOH) + $^{t}Bu_3ArO^{\bullet}$	$1.7 \pm 0.4 \times 10^4$	$5.8 \pm 2.0 \times 10^4$
Ru^{II}(bpy-COOH) + $^{t}Bu_2OMeArO^{\bullet}$	$2.9 \pm 1.0 \times 10^4$	$4.2 \pm 1.5 \times 10^4$
Ru^{II}(bpy-Ph-COOH) + $^{t}Bu_2OMeArO^{\bullet}$	-	$6.5 \pm 2.0 \times 10^2$

As mentioned previously, if phenoxyl radicals react with the **Ru^{III}~(COO)** products of the reaction or impurities, then pseudo first-order conditions are disadvantageous due to the interference of these subsequent or side reactions. One way to limit these side reactions is to monitor the reaction with phenoxyl radical as the limiting reagent. Figure 3.17 and Table 3.8 show the pseudo first-order rate constants determined for reactions of $^{t}Bu_3ArO^{\bullet}$ with varying concentrations of excess **Ru^{II}(bpy-COOH)**. A second-order rate constant of $k_2 = 2.1 \pm 0.6 \times 10^5$ M^{-1} s^{-1} was determined for this reaction, in good agreement with the rate constant determined under pseudo first-order conditions with excess $^{t}Bu_3ArO^{\bullet}$. This suggests that reactions of $^{t}Bu_3ArO^{\bullet}$ with products or other species is not occurring in this reaction. Thus, for reactions with **Ru^{II}(bpy-COOH)**, the rate constants determined by the pseudo first-order method are more reliable and will be used in subsequent analyses.

The large difference in second-order rate constants for the reaction of **Ru^{II}(bpy-Ph-COOH)** with stoichiometric or excess $^{t}Bu_3ArO^{\bullet}$ could be a result of side reactions involving $^{t}Bu_3ArO^{\bullet}$ occurring in the reaction with excess $^{t}Bu_3ArO^{\bullet}$. Pseudo first-order reactions with excess **Ru^{II}(bpy-Ph-COOH)** have not been performed. For reactions with **Ru^{II}(bpy-Ph-COOH)**, the second-order rate constant determined from second-order conditions will be used in further analysis.

3.2.5.5 Eyring Analysis of Reactions of Ru~(COOH) with $^{t}Bu_3ArO^{\bullet}$. The enthalpy of activation ($\Delta H^{\ddagger}$) and entropy of activation ($\Delta S^{\ddagger}$) were determined by monitoring the reactions of **Ru^{II}(bpy-COOH)** and **Ru^{II}(bpy-Ph-COOH)** with $^{t}Bu_3ArO^{\bullet}$ at various temperatures and generating Eyring plots (Figures 3.11). Eyring analysis of the reaction of **Ru^{II}(bpy-COOH)** with $^{t}Bu_3ArO^{\bullet}$ (243-298 K) gives $\Delta H^{\ddagger} = 4.2 \pm 0.5$ kcal mol^{-1} and $\Delta S^{\ddagger} = -20 \pm 2$ cal mol^{-1} K^{-1} at 298 K

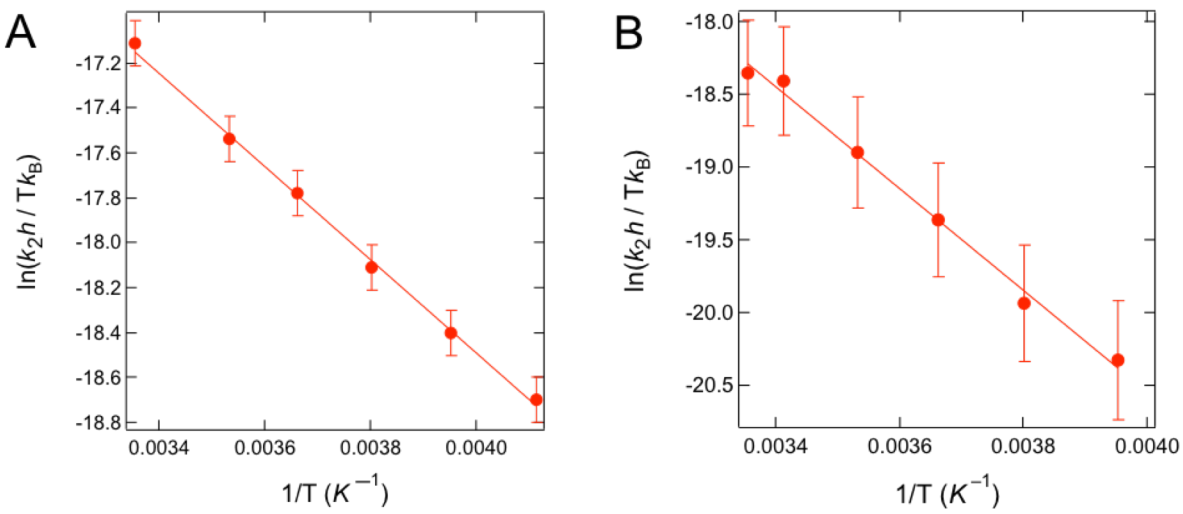

Figure 3.11A. Eyring plot of the reaction of **Ru^{II}(bpy-COOH)** with ^{t}Bu$_3$ArO$^{\bullet}$ from -30 ºC to 25 ºC. **Figure 3.11B.** Eyring plot of the reaction of **Ru^{II}(bpy-Ph-COOH)** with ^{t}Bu$_3$ArO$^{\bullet}$ from -20 ºC to 25 ºC.

(Figure 3.11A). These parameters are in good agreement with the $\Delta G^{\ddagger}$ = 10.2 ± 0.2 kcal mol^{-1} calculated from the second-order rate constant of 2.0 ± 0.4 × 10^5 M^{-1} s^{-1} at 298 K. The activation parameters of $\Delta H^{\ddagger}$ = 6.9 ± 0.3 kcal mol^{-1} and $\Delta S^{\ddagger}$ = -13 ± 1 cal mol^{-1} K^{-1} at 298 K were determined for the reaction of **Ru^{II}(bpy-Ph-COOH)** with ^{t}Bu$_3$ArO$^{\bullet}$ (253-298 K, Figure 3.11B). These parameters are in agreement with the $\Delta G^{\ddagger}$ = 10.9 ± 0.2 kcal mol^{-1} determined from the second-order rate constant of 5.8 ± 2.0 × 10^4 at 298 K. These activation parameters are typical of a bimolecular (associative) reaction.

3.2.6 Reactions of Ru^{II}~COOH with (2,2,6,6-Tetramethylpiperidin-1-yl)oxyl. Nitroxyl radical (2,2,6,6-tetramethylpiperidin-1-yl)oxyl (TEMPO$^{\bullet}$) is a good hydrogen atom acceptor with a relatively weak BDFE(O-H) of 66.5 kcal mol^{-1}. Thus, the reaction of **Ru^{II}(bpy-COOH)** with TEMPO$^{\bullet}$ is uphill (ΔG^{o}_{PCET} is calculated to be +3.0 ± 1 kcal mol^{-1} from BDFE(O-H) values). In order to study the kinetics of this reaction, a ~5000-fold excess of TEMPO$^{\bullet}$ was used to achieve

a reasonable yield of **Ru^{III}(bpy-COO)** and TEMPOH in stopped-flow reactions. **Ru^{III}(bpy-COO)** was formed in 92% yield. The equilibrium constant can be calculated from the initial concentrations of **Ru^{II}(bpy-COOH)** and TEMPO$^{\bullet}$ and the final concentration of **Ru^{III}(bpy-COO)** (assuming this is equal to the final concentration of TEMPOH). The equilibrium constant was found to be $K_{eq} = 2.3 \pm 0.5 \times 10^{-3}$, which corresponds to a $\Delta G^{o}_{PCET} = +3.6 \pm 0.1$ kcal mol^{-1} at 298 K. This is within the large estimated error of the ΔG^{o}_{PCET} calculated from BDFE(O-H) values. The spectral changes were analyzed using a second-order equilibrium model (Equations 3.11 and 3.12), where the ratio k_2/k_{-2} was held constant at the experimentally determined equilibrium constant, $K_{eq} = 2.3 \pm 0.5 \times 10^{-3}$. A second-order rate constant of $k_2 = 0.95 \pm 0.4$ M^{-1} s^{-1} was determined for the reaction of **Ru^{II}(bpy-COOH)** with TEMPO$^{\bullet}$ approaching equilibrium ($\Delta G^{\ddagger} = 17.5 \pm 0.3$ kcal mol^{-1}). The reaction of **Ru^{II}(bpy-COOD)** with TEMPO$^{\bullet}$ in acetonitrile with 0.2% MeOD is slower with a second-order rate constant of $k_{2,MeOD} = 0.29 \pm 0.07$ M^{-1} s^{-1}. The reaction of **Ru^{II}(bpy-COOH)** with TEMPO$^{\bullet}$ in acetonitrile with 0.2% MeOH is $k_{2,MeOH} = 0.81 \pm 0.4$ M^{-1} s^{-1}. Calculating the KIE from the rate constants in acetonitrile with 0.2% MeOH or 0.2% MeOD gives a KIE of 2.8 ± 1.4.

Using the BDFE(O-H) of **Ru^{II}(bpy-Ph-COOH)** determined from reactions with $^{t}Bu_2$OMeArO$^{\bullet}$ (73.8 ± 1 kcal mol^{-1}), the ΔG^{o}_{PCET} of the reaction of **Ru^{II}(bpy-Ph-COOH)** with TEMPO$^{\bullet}$ is uphill by +7.3 ± 1 kcal mol^{-1}. Thus, a large excess of TEMPO$^{\bullet}$ was used to achieve a reasonable yield of **Ru^{III}(bpy-Ph-COO)** and TEMPOH in stopped-flow reactions. The reaction of **Ru^{II}(bpy-Ph-COOH)** with a 3200-fold excess of TEMPO$^{\bullet}$ gave a 81% yield of **Ru^{III}(bpy-Ph-COO)**. The equilibrium constant can be calculated from the initial concentrations of **Ru^{II}(bpy-Ph-COOH)** and TEMPO$^{\bullet}$ and the final concentration of **Ru^{III}(bpy-Ph-COO)** formed, assuming the final concentration of TEMPOH formed is equal to the final concentration of **Ru^{III}(bpy-Ph-**

COO). The equilibrium constant was found to be K_{eq} = 1.9 ± 1.4 × 10^{-3} in this reaction, which corresponds to a ΔG^{o}_{PCET} = +3.7 ± 0.3 kcal mol^{-1} at 298 K. This is significantly different from the ΔG^{o}_{PCET} calculated from BDFE(O-H) values. The spectral changes were analyzed using a second-order equilibrium model (Equations 3.11 and 3.12), where the ratio k_2/k_{-2} was held constant at the equilibrium constant determined from the reaction, K_{eq} = 1.9 × 10^{-3}. A second-order rate constant of k_2 = 1.9 ± 1.7 M^{-1} s^{-1} was determined ($\Delta G^{‡}$ = 17.1 ± 1.3 kcal mol^{-1}). For the reaction of **Ru^{II}(bpy-Ph-COOD)** with $TEMPO^{•}$ in acetonitrile with 0.2% MeOD, a second-order rate constant of $k_{2,MeOD}$ = 0.83 ± 0.74 M^{-1} s^{-1} was determined ($\Delta G^{‡}$ = 17.6 ± 1.2 kcal mol^{-1}). The large estimated uncertainty results from the large differences between the observed equilibrium constants and the equilibrium constants calculated from BDFE values (calculated from pK_a and $E_{1/2}$ values), since the equilibrium constant is integral to the rate constant determination. These rate constants give a KIE of 2.3 ± 1.0.[27]

3.3 Discussion

3.3.1 Comparison of Calculated Bond Dissociation Free Energies and Experimental Equilibrium Constants. The bond dissociation free energy (BDFE(O-H)) of **Ru^{II}(bpy-COOH)** calculated from pK_a and $E_{1/2}$ values is 69.5 ± 1.0 kcal mol^{-1}. This predicts a ΔG^o_{PCET} of +3.0 ± 1 kcal mol^{-1} for the reaction of **Ru^{II}(bpy-COOH)** with TEMPO$^\bullet$. The experimentally measured equilibrium constant of the reaction of **Ru^{II}(bpy-COOH)** with TEMPO$^\bullet$ approaching equilibrium was found to be K_{eq} = 2.3 ± 0.5 × 10^{-3}. A ΔG^o_{PCET} of +3.6 ± 0.1 kcal mol^{-1} can be calculated from the measured equilibrium constant. A BDFE(O-H) of 70.1 ± 0.5 kcal mol^{-1} of **Ru^{II}(bpy-COOH)** can be calculated as well from this measured equilibrium constant and is within the estimated uncertainty of the BDFE(O-H) calculated from pK_a and $E_{1/2}$ values. This experimentally determined equilibrium constant is more precise than the equilibrium constant calculated from pK_a, $E_{1/2}$, and BDFE values and will be used in subsequent discussions. Likewise, the more precise BDFE(O-H) of 70.1 ± 0.5 kcal mol^{-1} for **Ru^{II}(bpy-COOH)** (calculated from the experimentally determined equilibrium constant and the BDFE(O-H) of TEMPOH) will be used henceforth.

The BDFE(O-H) of **Ru^{II}(bpy-Ph-COOH)**, calculated from pK_a and $E_{1/2}$ values, is 72.2 ± 1.0 kcal mol^{-1}. The reactions of **Ru^{II}(bpy-Ph-COOH)** with ^{t}Bu$_2$OMeArO$^\bullet$ and with TEMPO$^\bullet$ both approach equilibrium. From the BDFE(O-H) calculated from pK_a and $E_{1/2}$ values, the reaction of **Ru^{II}(bpy-Ph-COOH)** with ^{t}Bu$_2$OMeArO$^\bullet$ is predicted to have a ΔG^o_{PCET} of -2.2 ± 1.0 kcal mol^{-1}, and the reaction with TEMPO$^\bullet$ is predicted to have a ΔG^o_{PCET} of +5.7 ± 1.0 kcal mol^{-1}. The experimentally measured equilibrium constants for these reactions give ΔG^o_{PCET} at 298 K of -0.63 ± 0.5 kcal mol^{-1} and +3.7 ± 1.0 kcal mol^{-1}, respectively. Calculating the BDFE(O-H) **Ru^{II}(bpy-Ph-COOH)** from these ΔG^o_{PCET} values gives different BDFE(O-H) values of 73.8 ±

0.5 kcal mol^{-1} and 70.2 ± 1.0 kcal mol^{-1}. The source of this significant difference is unknown at this time. For subsequent discussions and calculations, a BDFE(O-H) of 72.0 ± 2.1 kcal mol^{-1} for **Ru^{II}(bpy-Ph-COOH)** will be used, which is the average of the BDFE(O-H) values calculated using the ΔG^{o}_{PCET} determined experimentally.

The **Ru^{II}(bpy-Ph-COOH)** BDFE(O-H) calculated from the experimental TEMPO$^{\bullet}$ reaction equilibrium constant is very close the BDFE(O-H) of **Ru^{II}(bpy-COOH)** (also calculated from the experimental TEMPO$^{\bullet}$ reaction equilibrium constant). This result does not agree with the pK_a values of the two complexes, which clearly indicate that the carboxylic acids of each complex have different acidity. One way to directly measure the difference between the BDFE(O-H) of **Ru^{II}(bpy-COOH)** and the BDFE(O-H) of **Ru^{II}(bpy-Ph-COOH)** would be to titrate a solution of **Ru^{II}(bpy-Ph-COOH)** and aliquots of a solution of **Ru^{III}(bpy-COO)** and monitor the formation of **Ru^{III}(bpy-Ph-COO)** and **Ru^{II}(bpy-COOH)** by UV-vis spectroscopy.

3.3.2 Possible PCET Pathways of Reactions of Ru^{II}~(COOH) Complexes with Hydrogen Atom Acceptors. There are three possible mechanisms by which the ruthenium complexes (Ru^{II}~COOH) could transfer a proton and an electron to a hydrogen atom acceptor (Figure 3.12). A ruthenium complex could transfer a proton to the RO$^{\bullet}$, forming Ru^{II}~COO^{-} and a radical cation ($ROH^{\bullet+}$), followed by electron transfer (ET) to give the final products, Ru^{III}~COO and ROH. This mechanism will be referred to as initial proton transfer (PT). Alternatively, a ruthenium complex could transfer an electron to the hydrogen atom acceptor, forming Ru^{III}~COOH and an oxyanion (RO^{-}), followed by PT to give Ru^{III}~COO and ROH. This mechanism will be referred to as initial ET. Lastly, the proton and electron could transfer in a

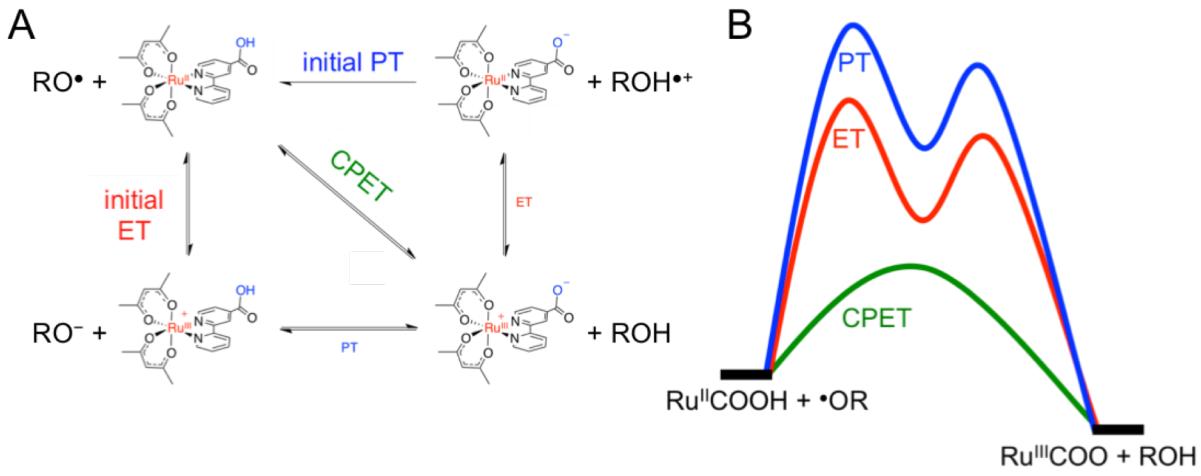

Figure 3.12A. Square scheme depicting the possible PCET pathways and intermediate ruthenium complexes of reactions of **Ru^{II}(bpy-COOH)** with hydrogen atom acceptors. **Figure 3.12B.** Energy diagram depicting the possible PCET pathways of reactions of **Ru^{II}(bpy-COOH)** with hydrogen atom acceptors ($^{\bullet}$OR). Relative energies are arbitrarily assigned in this generalized example.

single kinetic step in a mechanism commonly referred to as concerted proton-electron transfer (CPET).[28]

The free energy of formation of the intermediates formed by the initial PT (ΔG_{PT}^{o}) and initial ET (ΔG_{ET}^{o}) mechanisms can be calculated from the pK_a and $E_{1/2}$ values of the reactants using Equations 3.2 and 3.3.[23] Table 3.4 includes the calculated ΔG_{PT}^{o} and ΔG_{ET}^{o} values for each reaction, as well as the activation energy ($\Delta G^{\ddagger}$) of each reaction for comparison (calculated from k_2). For the reaction of **Ru^{II}(bpy-COOH)** or **Ru^{II}(bpy-Ph-COOH)** with TEMPO$^{\bullet}$, the $\Delta G^{\ddagger}$ is significantly smaller than either ΔG_{PT}^{o} or ΔG_{ET}^{o} (Table 3.4). Thus, these reactions must occur by a CPET mechanism.

Table 3.4. Reaction free energies, rate constants, activation energies, and free energy of formation of intermediates in initial PT and initial ET mechanisms, and kinetic isotope effects for the reactions of **Ru^{II}~COOH** complexes with hydrogen atom acceptors.

Reaction	**Reaction Free Energy, ΔG^{o}_{PCET} (kcal mol^{-1})**	**Rate Constant, k_2 (M^{-1} s^{-1})**	**Activation Energy, $\Delta G^{\ddagger}$ (kcal mol^{-1})**	**Energy of Initial PT, ΔG_{PT}^{o} (kcal mol^{-1})**	**Energy of Initial ET, ΔG_{ET}^{o} (kcal mol^{-1})**	**Kinetic Isotope Effect (KIE)**
Ru^{II}(bpy-COOH) + $^{t}Bu_3ArO^{\bullet}$	-7.0 ± 1.0	2.0 ± 0.4 × 10^5	10.2 ± 0.2	30.0 ± 0.5	7.1 ± 0.5	1.8 ± 0.7
Ru^{II}(bpy-COOH) + $^{t}Bu_2OMeArO^{\bullet}$	-4.3 ± 1.0	2.9 ± 1.0 × 10^4	11.4 ± 0.2	22.1 ± 0.5	10.4 ± 0.5	2.4 ± 0.8
Ru^{II}(bpy-COOH) + $TEMPO^{\bullet}$	+3.6 ± 0.1	0.95 ± 0.4	17.5 ± 0.3	31.4 ± 0.5	36.0 ± 0.5	2.8 ± 1.4
Ru^{II}(bpy-Ph-COOH) + $^{t}Bu_3ArO^{\bullet}$	-5.1 ± 2.1	5.8 ± 2.0 × 10^4	10.9 ± 0.3	32.7 ± 0.3	5.5 ± 0.5	1.1 ± 0.4
Ru^{II}(bpy-Ph-COOH) + $^{t}Bu_2OMeArO^{\bullet}$	-2.4 ± 2.1	6.5 ± 2.0× 10^2	13.6 ± 0.2	24.8 ± 0.3	8.8 ± 0.5	1.1 ± 0.3
Ru^{II}(bpy-Ph-COOH) + $TEMPO^{\bullet}$	+5.5 ± 2.1	1.9 ± 1.7	17.1 ± 1.3	34.1 ± 0.3	34.4 ± 0.5	2.3 ± 1.0

$TEMPO^{\bullet}$ has a strong bias for accepting a net hydrogen atom rather than a single proton or a single electron due to the strong acidity of $TEMPOH^{\bullet+}$ and strong reducing ability of $TEMPO^{-}$. Phenoxyl radicals are also poor proton acceptors (phenol radical cations are very acidic), but they can more easily accept an electron than $TEMPO^{\bullet}$ (phenoxides are much weaker reductants than $TEMPO^{-}$). For reactions of Ru^{II}~COOH with phenoxyl radicals, the ΔG_{PT}^{o} is significantly higher than the observed $\Delta G^{\ddagger}$, therefore the initial PT mechanism is not a possible, like in the reaction of **Ru^{II}(bpy-COOH)** with $TEMPO^{\bullet}$. However, the ΔG_{ET}^{o} is lower than the observed $\Delta G^{\ddagger}$ for every reaction of Ru^{II}~COOH with a phenoxyl radical, and the initial ET mechanism cannot be ruled out for these reactions based on these thermochemical arguments alone.

A primary KIE was measured for both reactions of **Ru^{II}(bpy-COOH)** with a phenoxyl radical, indicating that a PT is involved in the RDS. The initial PT mechanism and the CPET mechanism both involve a PT in the RDS, however, the initial PT mechanism was ruled out for these reactions based on thermochemical arguments. Although an initial ET mechanism is energetically possible, the primary KIE demonstrates the involvement of the proton in the RDS, and consequently a CPET mechanism is likely occurring.

For reactions of **Ru^{II}(bpy-Ph-COOH)** with phenoxyl radicals, the ΔG_{ET}^{o} is calculated to be 4-5 kcal mol^{-1} lower than the observed $\Delta G^{\ddagger}$, so an initial ET mechanism is energetically possible. These reactions also do not exhibit a KIE, so this result does not provide evidence for a CPET mechanism. **Ru^{II}(bpy-Ph-COOH)** is more reducing than **Ru^{II}(bpy-COOH)** by 70 mV, so ΔG_{ET}^{o} for a reaction of **Ru^{II}(bpy-Ph-COOH)** with a particular phenoxyl radical is less positive than ΔG_{ET}^{o} for the analogous reaction of **Ru^{II}(bpy-COOH)**. The rate constant of a reaction of **Ru^{II}(bpy-Ph-COOH)** with a particular phenoxyl radical is smaller than the rate constant of the analogous reaction of **Ru^{II}(bpy-COOH)**. If the mechanism is initial ET, then this is the opposite trend one would expect based on typical free energy relationships. However, the smaller rate constants for the reactions involving **Ru^{II}(bpy-Ph-COOH)** could be due to the longer distance between PT and ET sites. If the mechanism is CPET, the rate constants and ΔG_{PCET}^{o} values for reactions of **Ru^{II}(bpy-COOH)** and **Ru^{II}(bpy-Ph-COOH)** with phenoxyl radicals follow the expected trends based on typical free energy relationships (larger rate constants correlate with more negative ΔG_{PCET}^{o}).

3.3.3 Dependence of Rate Constants on PT/ET Transfer Site Distance. PCET reactions of phenoxyl radicals with **Ru^{II}(bpy-COOH)** are faster than the corresponding reactions with the

more separated **Ru^{II}(bpy-Ph-COOH)**. This trend has been observed with other ruthenium and iron complexes used for PCET distance dependence studies.[29-31] However, the decrease in rate constants over longer PT-ET sites distance is smaller than the decrease observed for other ruthenium complexes with similar distances between PT and ET sites. For reactions of phenols with the Ru(III) terpyridine-carboxylate complexes reported by Manner et al, the rate constants of reactions of the complex with more separation between the PT and ET sites (Ru^{III}(tpy-Ph-COO)) are slower by a factor of 630 to 1500 than the rate constants of the complex with less separation (Ru^{III}(tpy-COO)).[30-32] This trend is observed despite larger driving forces for reactions involving Ru^{III}(tpy-Ph-COO). The rate constants of **Ru^{II}(bpy-Ph-COOH)** with phenoxyl radicals are a factor of 3.4 or 44 slower than the analogous rate constants of **Ru^{II}(bpy-COOH)**. This could be a result of a small dependence of the rate constants on the distance between the PT and ET transfer sites, or it could be associated with the differences in driving force, as will be discussed in Section 3.3.4. Another possibility is that **Ru^{II}(bpy-COOH)** reacts with phenoxyl radicals by a CPET mechanism while **Ru^{II}(bpy-Ph-COOH)** reacts with phenoxyl radicals by an initial ET mechanism, in which case the rate constants' dependence on distance or driving force cannot be compared.

The rate constant of the reaction of **Ru^{II}(bpy-COOH)** with $TEMPO^{\bullet}$ is 0.95 ± 0.4 M^{-1} s^{-1} and the rate constant of the reaction of **Ru^{II}(bpy-Ph-COOH)** with $TEMPO^{\bullet}$ is 1.9 ± 1.7 M^{-1} s^{-1}. Thus, the reaction involving **Ru^{II}(bpy-Ph-COOH)** is faster by a factor of 2. The ΔG^{o}_{PCET} of the reaction of **Ru^{II}(bpy-COOH)** is +3.6 ± 0.1 kcal mol^{-1} and the ΔG^{o}_{PCET} of the reaction of **Ru^{II}(bpy-Ph-COOH)** is +5.5 ± 2.1 kcal mol^{-1}. Therefore, the reaction with a more positive ΔG^{o}_{PCET} has a larger rate constant. This does not agree with typical linear free energy relationships. Additionally, an increase in the rate constant with increased distance between the

PT and ET sites is unexpected. In the Ru(III) terpyridine-carboxylate system, the rate constant of the reaction of the Ru^{III}(tpy-Ph-COO) with TEMPOH is slower than the rate constant of the reaction of Ru^{III}(tpy-COO) with TEMPOH by a factor of 2. Although a decrease in the rate constant with increasing distance is expected, the difference by a factor of 2 is much smaller than the difference by a factor of 630 to 1500 observed for reactions with phenoxyl radicals. Also, t,he reaction of Ru^{III}(tpy-Ph-COO) with TEMPOH has a smaller rate constant despite have a more negative driving force than the reaction of Ru^{III}(tpy-COO) with TEMPOH. It seems in general, PCET reactions involving these separated ruthenium complexes and TEMPO$^{\bullet}$ or TEMPOH have little dependence on distance between the ET and PT transfer sites.

3.3.4 Dependence of Rate Constants on PCET Driving Force. The dependence of rate constants on driving force for sets of reactions with similar substrates has been described by a variety of methods, including Marcus theory.[33] Often used to describe ET reactions, Marcus theory relates the activation barrier to free energy and the intrinsic barrier λ according to Equation 3.4. Marcus theory has also been used to describe CPET reactions with both small organic molecules and metal complexes.[34-40]

$$\Delta G^{\ddagger} = \frac{\lambda}{4}\left(1 + \frac{\Delta G^{\circ\prime}}{\lambda}\right)^2 \tag{3.4}$$

A plot of $\Delta G^{\ddagger}$ versus ΔG^{o}_{PCET} shows reactions of both ruthenium complexes with hydrogen atom acceptors follow a linear trend (Figure 3.13). There are caveats associated with this correlation, however. Correlations between reactions of **Ru^{II}(bpy-Ph-COOH)** with hydrogen atom acceptors can only be made if all of the reactions are occurring by the same mechanism.

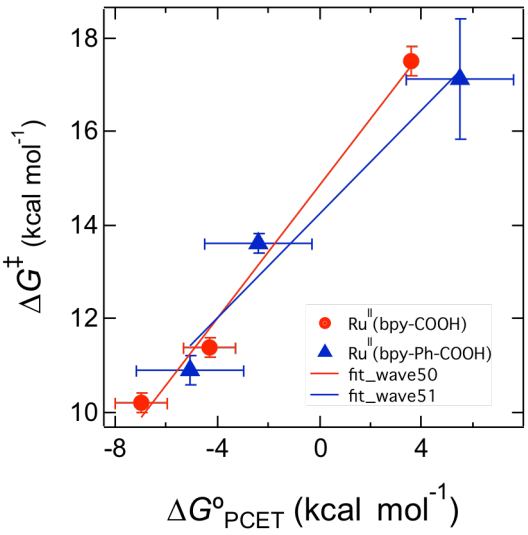

Figure 3.13. Plot of the activation barrier ($\Delta G^{\ddagger}$) versus the PCET reaction free enegy (ΔG^{o}_{PCET}).

Although a CPET mechanism is possible for reactions of **Ru^{II}(bpy-Ph-COOH)** with phenoxyl radicals, there is not conclusive evidence for a CPET mechanism over an initial ET mechanism, and both are possible. Fitting the $\Delta G^{\ddagger}$ values of **Ru^{II}(bpy-COOH)** reactions to a line gives a slope of 0.71 ± 0.07, larger than the 0.5 slope predicted by Marcus theory.[41] A linear fit to the $\Delta G^{\ddagger}$ values for reactions of **Ru^{II}(bpy-Ph-COOH)** with hydrogen atom acceptors gives a smaller slope of 0.55 ± 0.11 The $\Delta G^{\ddagger}$ of reactions of **Ru^{II}(bpy-Ph-COOH)** with phenoxyl radicals are similar in magnitude to the $\Delta G^{\ddagger}$ of reactions of **Ru^{II}(bpy-COOH)** based on their ΔG^{o}_{PCET} values and comparing to the $\Delta G^{\ddagger}$ versus ΔG^{o}_{PCET} trend observed for **Ru^{II}(bpy-COOH)**. It is unusual that the $\Delta G^{\ddagger}$ of reactions of **Ru^{II}(bpy-Ph-COOH)** would be similar to those of **Ru^{II}(bpy-COOH)** at similar driving forces. It is possible that the reactions of **Ru^{II}(bpy-COOH)** with phenoxyl radicals and **Ru^{II}(bpy-Ph-COOH)** with phenoxyl radicals occur by different mechanisms, in which the rate constants cannot be compared and the trends cannot be discussed. However, the reactions of TEMPO$^{\bullet}$ with either **Ru^{II}(bpy-COOH)** or **Ru^{II}(bpy-Ph-COOH)** both

occur by CPET as indicated by thermochemical arguments and measured KIEs. The similarity in CPET the $\Delta G^{\ddagger}$ of these reactions despite large differences in the distance between the PT and ET sites is unusual, and the origin of this strange result is unknown at this time.

3.4 Conclusion

The reactivity of ruthenium bipyridine complexes with separation between the PT and ET sites was investigated. The complex with less separation between the PT and ET sites, **Ru^{II}(bpy-COOH)**, reacts with hydrogen atom acceptors by a CPET mechanism, as suggested by thermochemical arguments, significant KIEs, and dependence of the log(k_2) on PCET driving forces. In contrast, the complex with larger separation between the PT and ET sites, **Ru^{II}(bpy-Ph-COOH)**, reacts with phenoxyl radicals by either a CPET mechanism or an initial ET mechanism. Thermochemical arguments and KIEs close to 1 indicate that initial ET is possible. The reaction of **Ru^{II}(bpy-Ph-COOH)** with TEMPO$^{\bullet}$ occurs by a CPET mechanism, as indicated by thermochemical arguments and the measured KIE. Reactions of **Ru^{II}(bpy-Ph-COOH)** and reactions of **Ru^{II}(bpy-COOH)** with similar PCET driving forces have similar $\Delta G^{\ddagger}$, which is an unexpected result for ET and CPET since a dependence of $\Delta G^{\ddagger}$ on ET distance is usually observed. There is no significant dependence of the PCET rate constants on distance in this system.

3.5 Experimental Section

3.5.1 General Considerations. All manipulations were carried out under nitrogen using glove-box/vacuum line techniques unless otherwise noted. Chemicals were purchased from Aldrich, Alfa-Aesar, EMD, Macron, or Fisher and used as received unless otherwise noted. Solvents used in the glove-box (dimethylformamide (DMF), dichloromethane (DCM), tetrahydrofuran (THF), and pentane) were purchased from Fischer Scientific and were dried using a Seca Solvent System installed by Glass Contour. These solvents were subsequently stored over 4 Å molecular sieves. Anhydrous acetonitrile (MeCN; <10 ppm H_2O) was purchased from Honeywell Burdick & Jackson, sparged with argon, and plumbed from a steel keg directly into a glovebox. Deuterated CD_3CN was purchased from Cambridge Isotope Laboratories, dried over CaH_2, vacuum transferred to P_2O_5, then vacuum transferred to fresh CaH_2 and finally into an empty vessel. Sealed ampules of deuterated DMF-d_7 were purchased from Cambridge Isotope Laboratories and used as received. All other solvents were purchased from Fisher Scientific or EMD Chemicals and used as received. $[Ru^{III}(acac)_2(MeCN)_2][OTf]$ was synthesized following literature procedures.[42]

3.5.2 Spectroscopic Measurements. All samples were prepared under N_2, unless otherwise noted. ^{1}H-NMR spectra were obtained on Bruker Avance spectrometers (Avance-500, DRX-499, Avance-300, and Avance-301), referenced to a residual solvent peak, and reported as δ (number of protons). UV-visible spectra were obtained with a Hewlett-Packard 8453 diode-array spectrophotometer.

3.5.3 Synthesis and Characterization of Ru^{II}(bpy-COOH) and Ru^{II}(bpy-Ph-COOH). The syntheses and characterizations of ruthenium(II) bis(acetylacetonate) 2,2′-bipyridine-4-carboxylic acid (**Ru^{II}(bpy-COOH)**) and ruthenium(II) bis(acetylacetonate) *p*-(2,2′-bipyridyl-4-yl)benzoic acid (**Ru^{II}(bpy-Ph-COOH)**) were described in Chapter 2.

3.5.4 NMR Reactions.

3.5.4.1 Ru^{II}(bpy-COOH) + $^{t}Bu_3ArO^{\bullet}$. A 26 mM solution of **Ru^{II}(bpy-COOH)** in MeCN-d_3 was prepared in a J. Young tube and a ^{1}H-NMR spectrum was taken. A 33 mM solution of $^{t}Bu_3ArO^{\bullet}$ in MeCN-d_3 was prepared and three 200 μL aliquots of this solution were added to the **Ru^{II}(bpy-COOH)** solution. A ^{1}H-NMR spectrum was taken after each addition. Addition of one aliquot (0.5 equivalent) of the $^{t}Bu_3ArO^{\bullet}$ solution resulted in the loss of the diamagnetic **Ru^{II}(bpy-COOH)** signals and formation of a broad, paramagnetic signal at -12 ppm, as well as formation of signals for $^{t}Bu_3ArOH$. After the addition of 1.0 equivalent of the $^{t}Bu_3ArO^{\bullet}$ solution, the broad paramagnetic peak shifted to -22 ppm and the $^{t}Bu_3ArOH$ signals increased in magnitude. The ^{1}H-NMR spectrum did not change after addition of 1.5 equivalents of the $^{t}Bu_3ArO^{\bullet}$ solution. The yield of $^{t}Bu_3ArOH$ was determined to be 100% by integrating the $^{t}Bu_3ArOH$ and **Ru^{II}(bpy-COOH)** signals relative to a hexamethyldisiloxane (HMDSO) internal standard. The identity of the signals for $^{t}Bu_3ArOH$ was confirmed by spiking the sample with $^{t}Bu_3ArOH$, which resulted in an increase in magnitude of the $^{t}Bu_3ArOH$ signals.

3.5.4.2 Ru^{II}(bpy-Ph-COOH) + $^{t}Bu_3ArO^{\bullet}$. A 4.0 mM solution of **Ru^{II}(bpy-Ph-COOH)** in MeCN-d_3 was prepared in a J. Young tube and a ^{1}H-NMR spectrum was taken. A 10 mM solution of $^{t}Bu_3ArO^{\bullet}$ in MeCN-d_3 was prepared and three 100 μL aliquots of this solution were

added to the **Ru^{II}(bpy-Ph-COOH)** solution. A ^{1}H-NMR spectrum was taken after each addition. Addition of one aliquot (0.5 equivalent) of the ^{t}Bu$_3$ArO$^\bullet$ solution resulted in the loss of the diamagnetic **Ru^{II}(bpy-Ph-COOH)** signals and formation of a broad, paramagnetic signal at -11 ppm, as well as formation of signals for ^{t}Bu$_3$ArOH. After the addition of 1.0 equivalent of the ^{t}Bu$_3$ArO$^\bullet$ solution, the broad paramagnetic peak shifted to -21 ppm and the ^{t}Bu$_3$ArOH signals increased in magnitude. The ^{1}H-NMR spectrum did not change after addition of 1.5 equivalents of the ^{t}Bu$_3$ArO$^\bullet$ solution. The yield of ^{t}Bu$_3$ArOH was determined to be 100% by integrating the ^{t}Bu$_3$ArOH and **Ru^{II}(bpy-Ph-COOH)** signals relative to a hexamethylbenzene internal standard.

3.5.4.3 Ru^{II}(bpy-COOH) + ^{t}Bu$_2$OMeArO$^\bullet$. A 16 mM solution of **Ru^{II}(bpy-COOH)** in MeCN-d_3 was prepared in a J. Young tube and a ^{1}H-NMR spectrum was taken. A 0.10 M solution of ^{t}Bu$_2$OMeArO$^\bullet$ in MeCN-d_3 was prepared and an 80 μL aliquot (1.0 equivalent) of this solution was added to the **Ru^{II}(bpy-COOH)** solution. The addition of one aliquot (1.0 equivalent) resulted in the loss of the diamagnetic **Ru^{II}(bpy-COOH)** signals and formation of a broad, paramagnetic peak at -22 ppm in the ^{1}H-NMR spectrum. The formation of signals for ^{t}Bu$_2$OMeArOH was also observed, and the yield of ^{t}Bu$_2$OMeArOH was determined to be 100% by integrating the ^{t}Bu$_2$OMeArOH and **Ru^{II}(bpy-COOH)** versus a HMDSO internal standard. The identity of the ^{t}Bu$_2$OMeArOH was confirmed by spiking the sample with ^{t}Bu$_2$OMeArOH, which resulted in an increase in the magnitude of the ^{t}Bu$_2$OMeArOH signals.

3.5.4.4 Ru^{II}(bpy-Ph-COOH) + ^{t}Bu$_2$OMeArO$^\bullet$. A 4.0 mM solution of **Ru^{II}(bpy-Ph-COOH)** in MeCN-d_3 was prepared in a J. Young tube and a ^{1}H-NMR spectrum was taken. A 34 mM solution of ^{t}Bu$_2$OMeArO$^\bullet$ in MeCN-d_3 was prepared and two 100 μL aliquot of this solution was

added to the **Ru^{II}(bpy-Ph-COOH)** solution. The addition of one aliquot (1.7 equivalents) resulted in the loss of the diamagnetic **Ru^{II}(bpy-Ph-COOH)** signals and formation of a broad, paramagnetic peak at -17 ppm in the ^{1}H-NMR spectrum. After addition of a second aliquot (3.4 equivalents), the broad peak shifted to -19 ppm. The reaction of **Ru^{II}(bpy-Ph-COOH)** with ^{t}Bu$_2$OMeArO$^\bullet$ is in equilibrium, and **Ru^{III}(bpy-Ph-COO)** and ^{t}Bu$_2$OMeArOH are not formed in 100% yield under these conditions. The formation of signals for ^{t}Bu$_2$OMeArOH was also observed, and the yield of ^{t}Bu$_2$OMeArOH was determined to be 80% by integrating the ^{t}Bu$_2$OMeArOH and **Ru^{II}(bpy-COOH)** versus a hexamethylbenzene internal standard.

3.5.5 UV-vis Reactions.

3.5.5.1 Ru^{II}(bpy-COOH) + ^{t}Bu$_3$ArO$^\bullet$. A 2.0 mM stock solution of **Ru^{II}(bpy-COOH)** was prepared. 81 μL of this solution was diluted to 2.0 mL to give a 81 μM solution of **Ru^{II}(bpy-COOH)** and the solution was sealed in a septum-capped cuvette. A 4.8 mM solution of ^{t}Bu$_3$ArO$^\bullet$ was prepared and 1 mL of this solution was sealed in a septum-capped vial. 3.4 μL (0.1 equivalent) aliquots of the ^{t}Bu$_3$ArO$^\bullet$ were added to the **Ru^{II}(bpy-COOH)** and the changes in the UV-vis spectra were monitored (Figure 3.1A). The MLCT bands of **Ru^{II}(bpy-COOH)** gradually disappeared and a new peak at 524 nm was formed as ^{t}Bu$_3$ArO$^\bullet$ was added. After addition of 1.0 equivalent of ^{t}Bu$_3$ArO$^\bullet$, the peaks for ^{t}Bu$_3$ArO$^\bullet$ at 380 and 400 nm began to appear with no other change in the spectra, indicating **Ru^{II}(bpy-COOH)** has reacted completely with ^{t}Bu$_3$ArO$^\bullet$, and additional ^{t}Bu$_3$ArO$^\bullet$ added is in excess. The absorbance at 635 nm was plotted versus equivalents of ^{t}Bu$_3$ArO$^\bullet$ added which shows that the reaction of **Ru^{II}(bpy-COOH)** and ^{t}Bu$_3$ArO$^\bullet$ is immediate and quantitative (Figure 3.1B).

3.5.5.2 Ru^{II}(bpy-Ph-COOH) + $^{t}Bu_3ArO^{\bullet}$. A 1.3 mM stock solution of **Ru^{II}(bpy-Ph-COOH)** was diluted to give a 120 μM solution. This solution was sealed in a septum-capped cuvette. A 1.5 mM solution of $^{t}Bu_3ArO^{\bullet}$ was sealed in a septum-capped vial. 10 μL (0.063 equivalent) aliquots of $^{t}Bu_3ArO^{\bullet}$ were added to the **Ru^{II}(bpy-Ph-COOH)** solution and changes in the UV-vis spectra were monitored (Figure 3.2A). The MLCT bands of **Ru^{II}(bpy-Ph-COOH)** gradually disappeared as $^{t}Bu_3ArO^{\bullet}$ was added. After addition of 1.0 equivalent of $^{t}Bu_3ArO^{\bullet}$, the spectrum of **Ru^{II}(bpy-Ph-COOH)** stopped changing, indicating that **Ru^{II}(bpy-Ph-COOH)** has reacted completely with $^{t}Bu_3ArO^{\bullet}$. The absorbance at 630 nm was plotted versus equivalents of $^{t}Bu_3ArO^{\bullet}$ added which shows that the reaction of **Ru^{II}(bpy-Ph-COOH)** and $^{t}Bu_3ArO^{\bullet}$ is immediate and quantitative (Figure 3.2B).

3.5.5.3 Ru^{II}(bpy-COOH) + $^{t}Bu_2OMeArO^{\bullet}$. A 1.8 mM stock solution of **Ru^{II}(bpy-COOH)** was prepared. 130 μL of this solution was diluted to 2.0 mL to give a 120 μM solution of **Ru^{II}(bpy-COOH)**. This solution was sealed in a septum-capped cuvette. A 15 mM solution of $^{t}Bu_2OMeArO^{\bullet}$ was prepared and 1 mL of this was sealed in a septum-capped vial. 1.6 μL (0.1 equivalent) aliquots of the $^{t}Bu_2OMeArO^{\bullet}$ solution were added to the **Ru^{II}(bpy-COOH)** and the changes in the UV-vis spectra were monitored (Figure 3.3A). The MLCT bands of **Ru^{II}(bpy-COOH)** disappeared and a new peak formed at 524 nm with successive addition of $^{t}Bu_2OMeArO^{\bullet}$. After addition of 1.0 equivalent of $^{t}Bu_2OMeArO^{\bullet}$, formation of peaks for $^{t}Bu_2OMeArO^{\bullet}$ at 390 and 410 were observed with no other change in the spectrum, indicating that **Ru^{II}(bpy-COOH)** has reacted completely with $^{t}Bu_2OMeArO^{\bullet}$ and additional added $^{t}Bu_2OMeArO^{\bullet}$ is in excess. A plot of absorbance at 635 nm versus equivalents of $^{t}Bu_2OMeArO^{\bullet}$ added shows that the reaction of **Ru^{II}(bpy-COOH)** is immediate and quantitative (Figure 3.3B).

3.5.5.4 Ru^{II}(bpy-Ph-COOH) + $^{t}Bu_2$OMeArO$^{\bullet}$. A 1.3 mM stock solution of **Ru^{II}(bpy-Ph-COOH)** was diluted to give a 130 μM solution. This solution was sealed in a septum-capped cuvette. A 3.4 mM solution of $^{t}Bu_2$OMeArO$^{\bullet}$ was sealed in a septum-capped vial. 10 μL (0.13 equivalent) aliquots of $^{t}Bu_2$OMeArO$^{\bullet}$ were added to the **Ru^{II}(bpy-Ph-COOH)** solution and changes in the UV-vis spectra were monitored (Figure 3.4A). The MLCT bands of **Ru^{II}(bpy-Ph-COOH)** gradually disappeared as $^{t}Bu_2$OMeArO$^{\bullet}$ was added. The absorbance at 630 nm was plotted versus equivalents of $^{t}Bu_2$OMeArO$^{\bullet}$ added which shows that the reaction approaches equilibrium (Figure 3.4B).

3.5.5.5 Determination of K_{eq} for the reaction of Ru^{II}(bpy-Ph-COOH) with $^{t}Bu_2$OMeArO$^{\bullet}$. The extinction coefficient of **Ru^{III}(bpy-Ph-COO)** at 630 nm ($\varepsilon_{Ru(III)(bpy\text{-}Ph\text{-}COO)}$ = 1950 M^{-1} cm^{-1}) was calculated from the titration of **Ru^{II}(bpy-Ph-COOH)** with $^{t}Bu_3$ArO$^{\bullet}$. The concentrations of **Ru^{II}(bpy-Ph-COOH)** and **Ru^{III}(bpy-Ph-COO)** were calculated using Equations 3.8 and 3.9, where $A_{630\,nm}$ is the volume-corrected absorbance at 630 nm and b is the pathlength of the cell (1 cm).

$$A_{630\,nm} = \varepsilon_{Ru^{II}(bpy\text{-}Ph\text{-}COOH)} b[Ru^{II}(bpy\text{-}Ph\text{-}COOH)] + \varepsilon_{Ru^{III}(bpy\text{-}Ph\text{-}COO)} b[Ru^{III}(bpy\text{-}Ph\text{-}COO)] \quad 3.6$$

$$[Ru]_{TOTAL} = [Ru^{II}(bpy\text{-}Ph\text{-}COOH)] + [Ru^{III}(bpy\text{-}Ph\text{-}COO)] \quad 3.7$$

$$[Ru^{II}(bpy\text{-}Ph\text{-}COOH)] = \frac{A_{630\,nm} - \varepsilon_{Ru^{III}(bpy\text{-}Ph\text{-}COO)}[Ru]_{TOTAL}}{\varepsilon_{Ru^{II}(bpy\text{-}Ph\text{-}COOH)} - \varepsilon_{Ru^{III}(bpy\text{-}Ph\text{-}COO)}} \quad 3.8$$

$$[Ru^{III}(bpy\text{-}Ph\text{-}COO)] = \frac{A_{630nm} - \varepsilon_{Ru^{II}(bpy\text{-}Ph\text{-}COOH)}[Ru]_{TOTAL}}{\varepsilon_{Ru^{III}(bpy\text{-}Ph\text{-}COO)} - \varepsilon_{Ru^{II}(bpy\text{-}Ph\text{-}COOH)}} \quad 3.9$$

$$K_{eq} = \frac{[^{t}Bu_2OMeArOH][Ru^{III}(bpy\text{-}Ph\text{-}COO)]}{[^{t}Bu_2OMeArO^{\bullet}][Ru^{II}(bpy\text{-}Ph\text{-}COOH)]} \quad 3.10$$

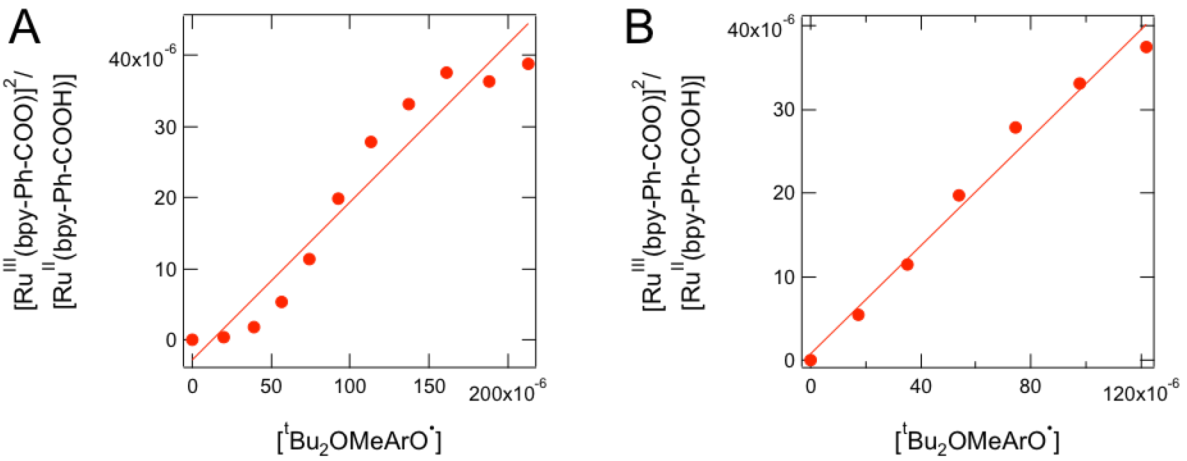

Figure 3.14A. Plot of [**Ru^{III}(bpy-Ph-COO)**]^2/[**Ru^{II}(bpy-Ph-COOH)**] versus [^{t}Bu$_2$OMeArO$^\bullet$]. **Figure 3.14B.** Plot of [**Ru^{III}(bpy-Ph-COO)**]^2/[**Ru^{II}(bpy-Ph-COOH)**] versus [^{t}Bu$_2$OMeArO$^\bullet$], assuming first 20 μL of ^{t}Bu$_2$OMeArO$^\bullet$ is consumed before reacting with **Ru^{II}(bpy-Ph-COOH)**.

Using a mass balance assumption, the concentration of ^{t}Bu$_2$OMeArOH is equal to the concentration of **Ru^{III}(bpy-Ph-COO)**, thus the slope of a plot of [**Ru^{III}(bpy-Ph-COO)**]^2/[**Ru^{II}(bpy-Ph-COOH)**] versus [^{t}Bu$_2$OMeArO$^\bullet$] is equal to $1/K_{eq}$ (Equation 3.10, Figure 3.14A). The K_{eq} was found to be 4.5 ± 0.5. Figure 3.14B shows the same plot, but [^{t}Bu$_2$OMeArO$^\bullet$] has been adjusted assuming the first 20 μL of added ^{t}Bu$_2$OMeArO$^\bullet$ is consumed by another route (perhaps reaction with oxygen). A K_{eq} of 3.1 ± 0.2 was determined from a linear fit to this plot.

3.5.6 Stopped-flow Reactions. Solutions were prepared in dry acetonitrile in the glove box, loaded into syringes with valves, and sealed. The solutions were mixed and the spectral changes

were monitored by rapid-scanning stopped-flow spectrophotometry. The full spectra as a function of time were analyzed with Specfit™ global fitting software.

3.5.6.1 Control Experiments. Solutions of **Ru^{II}(bpy-COOH)**, **Ru^{II}(bpy-Ph-COOH)**, $^{t}Bu_3ArO^{\bullet}$, $^{t}Bu_2OMeArO^{\bullet}$, and $TEMPO^{\bullet}$ were prepared. The solutions were mixed with dry acetonitrile (also loaded into syringes with valves in the glove box and sealed) and the spectra were monitored over time. Each reactant is stable on the time scale its second-order reactions.

3.5.6.2 Second-Order Conditions. For each reaction, the UV-vis spectra of each of these solutions were obtained and the concentrations of each of these solutions were calculated from the absorbance values.

3.5.6.2.1 Ru^{II}(bpy-COOH) + $^{t}Bu_3ArO^{\bullet}$. A 4.1 mM stock solution of $^{t}Bu_3ArO^{\bullet}$ was diluted to give a 63 μM solution. A 3.0 mM stock solution of **Ru^{II}(bpy-COOH)** was diluted to give 10 mL of a 59 μM solution. 10 μL of MeOD was added to 5.0 mL of this solution. The reaction of **Ru^{II}(bpy-COOH)** with $^{t}Bu_3ArO^{\bullet}$ in acetonitrile with no added methanol and with 0.2% MeOD was monitored in sequence. For the reaction of **Ru^{II}(bpy-COOH)** and $^{t}Bu_3ArO^{\bullet}$, the **Ru^{II}(bpy-COOH)** is 93% consumed in 0.75 s. For the reaction of **Ru^{II}(bpy-COOD)** and $^{t}Bu_3ArO^{\bullet}$ in acetonitrile with 0.2% MeOD, the **Ru^{II}(bpy-COOD)** is 90% consumed in 1.5 s. The full spectra as a function of time were analyzed using a second-order reaction model. The spectral changes over time and the fit to the kinetic trace at 450 nm are shown in Figure 3.7. To determine whether 0.2% MeOH had an effect on the reaction, the reaction of **Ru^{II}(bpy-COOH)** with $^{t}Bu_3ArO^{\bullet}$ in acetonitrile with 0.2% MeOH was monitored. The normalized spectral changes

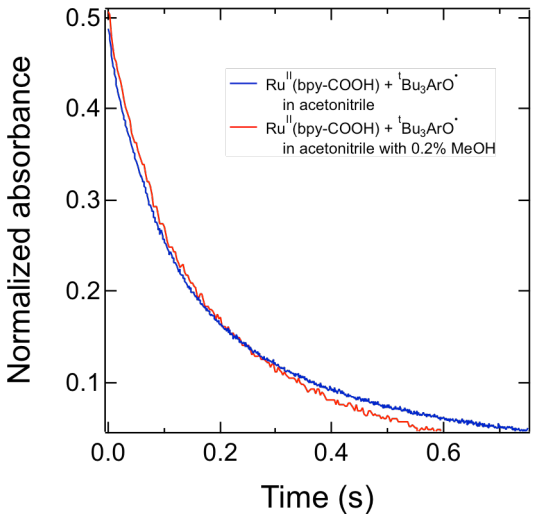

Figure 3.15. Normalized absorbance at 450 nm versus time of the reactions of **Ru^{II}(bpy-COOH)** with $^{t}Bu_3ArO^{\bullet}$ in acetonitrile (blue line) and **Ru^{II}(bpy-COOH)** with $^{t}Bu_3ArO^{\bullet}$ in acetonitrile with 0.2% MeOH (red line).

($A_{normalized} = (A_t - A_i)/(A_f - A_i)$) at 450 nm for the reaction of **Ru^{II}(bpy-COOH)** with $^{t}Bu_3ArO^{\bullet}$ in acetonitrile with no added methanol and with 0.2% MeOH are shown in Figure 3.15.

3.5.6.2.2 Ru^{II}(bpy-Ph-COOH) + $^{t}Bu_3ArO^{\bullet}$. A 1.5 mM stock solution of $^{t}Bu_3ArO^{\bullet}$ was diluted to give a 110 μM solution. A 1.3 mM stock solution of **Ru^{II}(bpy-Ph-COOH)** was diluted and filtered through a pipet filter to give 11 mL of a 120 μM solution. 6 μL of MeOH and 6 μL of MeOD were added to each of two 3.0 mL aliquots of the 120 μM solution of **Ru^{II}(bpy-Ph-COOH)**. The reaction of **Ru^{II}(bpy-Ph-COOH)** with $^{t}Bu_3ArO^{\bullet}$ in acetonitrile with no added methanol, 0.2% MeOH, and 0.2% MeOD was monitored in sequence. The full spectra as a function of time were analyzed with Specfit^{TM} global fitting software using a second-order reaction model. The spectral changes over time and the fit to the kinetic trace at 630 nm are shown in Figure 3.9.

3.5.6.2.3 Ru^{II}(bpy-COOH) + $^{t}Bu_2$OMeArO$^{\bullet}$. A 5.3 mM stock solution of $^{t}Bu_2$OMeArO$^{\bullet}$ was diluted to give a 59 μM solution. A 3.0 mM stock solution of **Ru^{II}(bpy-COOH)** was diluted to give 10 mL of a 50 μM solution. 10 μL of MeOD was added to 5.0 mL of this solution. The reaction of **Ru^{II}(bpy-COOH)** with $^{t}Bu_2$OMeArO$^{\bullet}$ in acetonitrile with no added methanol and acetonitrile with 0.2% MeOD was monitored in sequence. For the reaction of **Ru^{II}(bpy-COOH)** and $^{t}Bu_2$OMeArO$^{\bullet}$, the **Ru^{II}(bpy-COOH)** is 90% consumed in 3.75 s. For the reaction of **Ru^{II}(bpy-COOD)** and $^{t}Bu_2$OMeArO$^{\bullet}$ in acetonitrile with 0.2% MeOD, the **Ru^{II}(bpy-COOD)** is 89% consumed in 10 s. The full spectra as a function of time were analyzed using a second-order reaction model. The spectral changes over time and the fit to the kinetic trace at 435 nm are shown in Figure 3.7. To determine whether 0.2% MeOH had an effect on the reaction, the reaction of **Ru^{II}(bpy-COOH)** with $^{t}Bu_2$OMeArO$^{\bullet}$ in acetonitrile with 0.2% MeOH was monitored. The normalized spectral changes ($A_{normalized} = (A_t - A_i)/(A_f - A_i)$) at 435 nm for the

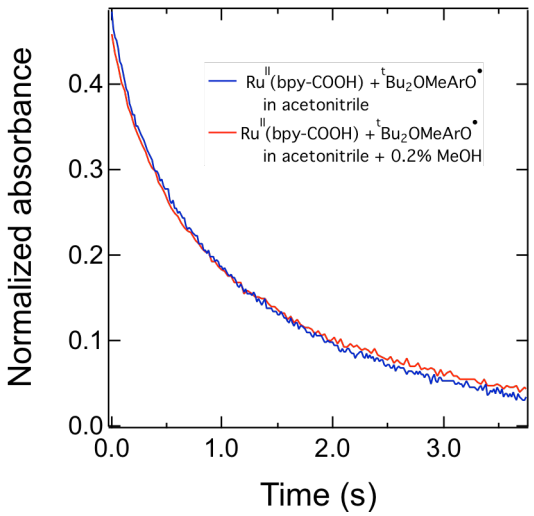

Figure 3.16. Normalized absorbance at 435 nm versus time of the reactions of **Ru^{II}(bpy-COOH)** with $^{t}Bu_2$OMeArO$^{\bullet}$ in acetonitrile (blue line) and **Ru^{II}(bpy-COOH)** with $^{t}Bu_2$OMeArO$^{\bullet}$ in acetonitrile with 0.2% MeOH (red line).

reaction of **Ru^{II}(bpy-COOH)** with $^{t}Bu_2OMeArO^{\bullet}$ in acetonitrile with no added methanol and with 0.2% MeOH are shown in Figure 3.16.

3.5.6.2.4 Ru^{II}(bpy-Ph-COOH) + $^{t}Bu_2OMeArO^{\bullet}$. A 5.3 mM stock solution of $^{t}Bu_2OMeArO^{\bullet}$ was diluted to give a 100 μM solution. A 0.92 mM stock solution of **Ru^{II}(bpy-Ph-COOH)** was diluted and filtered through a pipet filter to give 10 mL of a 120 μM solution. 6 μL of MeOH and 6 μL of MeOD were added to each of two 3.0 mL aliquots of the 120 μM solution of **Ru^{II}(bpy-Ph-COOH)**. The reaction of **Ru^{II}(bpy-Ph-COOH)** with $^{t}Bu_2OMeArO^{\bullet}$ in acetonitrile with no added methanol, 0.2% MeOH, and 0.2% MeOD was monitored in sequence. The full spectra as a function of time were analyzed using a second-order equilibrium reaction model (Equations 3.11 and 3.12). Both the forward and reverse reactions were fit and the ratio k_2/k_{-2} was held constant at the equilibrium constant of the reaction (K_{eq} = 2.9). The spectral changes over time and the fit to the kinetic trace at 630 nm are shown in Figure 3.10.

3.5.6.3 Eyring Analysis. Reactions of ruthenium complexes with $^{t}Bu_3ArO^{\bullet}$ were monitored by variable-temperature stopped-flow spectrophotometry.

3.5.6.3.1 Ru^{II}(bpy-COOH) + $^{t}Bu_3ArO^{\bullet}$. Solutions of **Ru^{II}(bpy-COOH)** (120 μM) and $^{t}Bu_3ArO^{\bullet}$ (180 μM) were prepared. The reaction of **Ru^{II}(bpy-COOH)** with $^{t}Bu_3ArO^{\bullet}$ was monitored at temperatures from -30 ºC to 25 ºC. The measured rate constants at each temperature are given in Table 3.5. Activation parameters for the reaction were determined by performing

$$A + B \xrightarrow{k_2} C + D \qquad (3.11)$$

$$C + D \xrightarrow{k_{-2}} A + B \qquad (3.12)$$

Eyring analysis (Figure 3.11A).

Table 3.5. Eyring parameters for the reaction of **Ru^{II}(bpy-COOH)** with $^{t}Bu_3ArO^{\bullet}$, including reaction temperatures, 1/T values, and second-order rate constants (k_2).

Temperature (K)	1/T (K^{-1})	Second-order rate constant, k_2 (M^{-1} s^{-1})
298	3.4×10^{-3}	2.3×10^{5}
283	3.5×10^{-3}	1.5×10^{5}
273	3.7×10^{-3}	1.1×10^{5}
263	3.8×10^{-3}	7.5×10^{4}
253	4.0×10^{-3}	5.4×10^{4}
243	4.1×10^{-3}	3.8×10^{4}

3.5.6.3.2 Ru^{II}(bpy-Ph-COOH) + $^{t}Bu_3ArO^{\bullet}$. Solutions of **Ru^{II}(bpy-Ph-COOH)** (130 μM) and $^{t}Bu_3ArO^{\bullet}$ (130 μM) were prepared. The reaction of **Ru^{II}(bpy-Ph-COOH)** with $^{t}Bu_3ArO^{\bullet}$ was monitored at temperatures from -20 ºC to 25 ºC. The measured rate constants at each temperature are given in Table 3.6. Activation parameters for the reaction were determined by performing Eyring analysis (Figure 3.11B).

Table 3.6. Eyring parameters for the reaction of **Ru^{II}(bpy-Ph-COOH)** with $^{t}Bu_3ArO^{\bullet}$, including reaction temperatures, 1/T values, and second-order rate constants (k_2).

Temperature (K)	1/T (K^{-1})	Second-order rate constant, k_2 (M^{-1} s^{-1})
298	3.36×10^{-3}	5.8×10^{4}
293	3.41×10^{-3}	6.3×10^{4}
283	3.5×10^{-3}	3.8×10^{4}
273	3.7×10^{-3}	2.4×10^{4}
263	3.8×10^{-3}	1.4×10^{4}
253	4.0×10^{-3}	9.2×10^{3}

3.5.6.4 Pseudo First-Order Conditions. For all reactions under pseudo first-order conditions, the full spectra as a function of time were analyzed using a first-order reaction model.

3.5.6.4.1 Ru^{II}(bpy-COOH) + $^{t}Bu_3ArO^{\bullet}$. A 1.8 mM stock solution of **Ru^{II}(bpy-COOH)** was diluted to give 7 mL of a 180 μM solution. A 5.1 mM stock solution of $^{t}Bu_3ArO^{\bullet}$ was diluted to obtain 3.0 mL solutions with the following concentrations of $^{t}Bu_3ArO^{\bullet}$: 1.8 mM, 2.1 mM, 2.5 mM, 2.8 mM, 3.2 mM, 3.5 mM. The reactions of **Ru^{II}(bpy-COOH)** with solutions of various concentrations of $^{t}Bu_3ArO^{\bullet}$ were monitored. The pseudo-first order rate constants determined at each concentration of $^{t}Bu_3ArO^{\bullet}$ are shown in Table 3.7. A plot of the pseudo-first order rate constants versus concentration of $^{t}Bu_3ArO^{\bullet}$ is shown in Figure 3.5A. The slope is equal to the second-order rate constant, $k = 2.0 \pm 0.4 \times 10^{5}$ M^{-1} s^{-1}.

Table 3.7. Concentrations of $^{t}Bu_3ArO^{\bullet}$ after mixing and pseudo first-order rate constants (k) for the reaction of **Ru^{II}(bpy-COOH)** with $^{t}Bu_3ArO^{\bullet}$.

Concentration of $^{t}Bu_3ArO^{\bullet}$ (mM)	**Pseudo First-order rate constant, k (s^{-1})**
0.90	121
1.05	137
1.25	165
1.4	201
1.6	207
1.75	231

The reactions of $^{t}Bu_3ArO^{\bullet}$ with solutions of various concentrations of **Ru^{II}(bpy-COOH)** were also monitored. A 10.8 mM stock solution of $^{t}Bu_3ArO^{\bullet}$ was diluted to give 10 mL of a 20 μM solution. A 1.7 mM stock solution of **Ru^{II}(bpy-COOH)** was diluted to obtain 2.0 mL solutions with the following concentrations of **Ru^{II}(bpy-COOH)**: 200 μM, 220 μM, and 240 μM. Table 3.8 shows the pseudo first-order rate constants at each concentration of **Ru^{II}(bpy-COOH)**. A plot of the pseudo-first order rate constants versus concentration of **Ru^{II}(bpy-COOH)** gave a second-order rate constant of $2.1 \pm 0.6 \times 10^5$ M^{-1} s^{-1} (Figure 3.17). The y-intercept is -0.12 ± 0.79 s^{-1}.

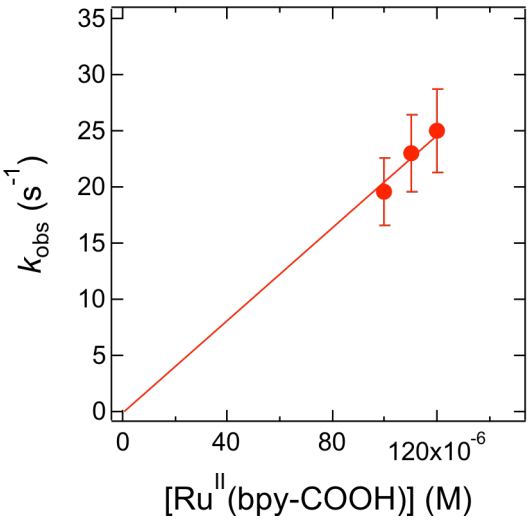

Figure 3.17. Pseudo first-order rate constants, k_{obs}, of the reaction of **Ru^{II}(bpy-COOH)** with $^{t}Bu_3ArO^{\bullet}$ versus concentration of **Ru^{II}(bpy-COOH)**.

Table 3.8. Concentrations of **Ru^{II}(bpy-COOH)** after mixing and pseudo first-order rate constants (k) for the reaction of **Ru^{II}(bpy-COOH)** with $^{t}Bu_3ArO^{\bullet}$.

Concentration of Ru^{II}(bpy-COOH) (mM)	**Pseudo First-order rate constant, k (s^{-1})**
0.10	19.5
0.11	22.9
0.12	25.0

3.5.6.4.2 Ru^{II}(bpy-Ph-COOH) + $^{t}Bu_3ArO^{\bullet}$. A stock solution of **Ru^{II}(bpy-Ph-COOH)** was diluted and filtered through a pipet filter to give 10 mL of a 130 μM solution. A 4.2 mM stock solution of $^{t}Bu_3ArO^{\bullet}$ was diluted to obtain 3.0 mL solutions with the following concentrations of $^{t}Bu_3ArO^{\bullet}$: 1.2 mM, 2.1 mM, 3.0 mM, 3.6 mM. The reactions of **Ru^{II}(bpy-Ph-COOH)** with solutions of various concentrations of $^{t}Bu_3ArO^{\bullet}$ were monitored. The pseudo-first order rate constants determined at each concentration of $^{t}Bu_3ArO^{\bullet}$ are shown in Table 3.9. A plot of the

pseudo-first order rate constants versus concentration of $^{t}Bu_3ArO^{\bullet}$ is shown in Figure 3.5B. The slope is equal to the second-order rate constant, $k = 1.7 \pm 0.4 \times 10^4\ M^{-1}\ s^{-1}$.

Table 3.9. Concentrations of $^{t}Bu_3ArO^{\bullet}$ after mixing and pseudo first-order rate constants (k) for the reaction of **Ru^{II}(bpy-Ph-COOH)** with $^{t}Bu_3ArO^{\bullet}$.

Concentration of $^{t}Bu_3ArO^{\bullet}$ (mM)	**Pseudo First-order rate constant, k (s^{-1})**
0.60	12.4
1.05	19.8
1.5	27.1
1.8	31.4

3.5.6.4.3 Ru^{II}(bpy-COOH) + $^{t}Bu_2OMeArO^{\bullet}$. A 1.8 mM stock solution of **Ru^{II}(bpy-COOH)** was diluted to give 8 mL of a 180 μM solution. A 14 mM stock solution of $^{t}Bu_2OMeArO^{\bullet}$ was diluted to obtain 3.0 mL solutions with the following concentrations of $^{t}Bu_2OMeArO^{\bullet}$: 1.6 mM, 2.0 mM, 2.4 mM, 3.2 mM, 4.0 mM, 4.8 mM. Each solution was loaded and sealed in a syringe with a valve. The reactions of **Ru^{II}(bpy-COOH)** with solutions of various concentrations of $^{t}Bu_2OMeArO^{\bullet}$ were monitored by single-mixing stopped-flow spectrophotometry. The full spectra as a function of time were analyzed with Specfit™ global fitting software using a first-order reaction model. The pseudo-first order rate constants determined at each concentration of $^{t}Bu_2OMeArO^{\bullet}$ are shown in Table 3.10. A plot of the pseudo-first order rate constants versus concentration of $^{t}Bu_2OMeArO^{\bullet}$ is shown in Figure 3.6. The slope is equal to the second-order rate constant, $k = 2.9 \pm 1.5 \times 10^4\ M^{-1}\ s^{-1}$.

Table 3.10. Concentrations of $^{t}Bu_2OMeArO^{\bullet}$ after mixing and pseudo first-order rate constants (k) for the reaction of **Ru^{II}(bpy-Ph-COOH)** with $^{t}Bu_2OMeArO^{\bullet}$.

Concentration of $^{t}Bu_2OMeArO^{\bullet}$ (mM)	**Pseudo First-order rate constant, k (s^{-1})**
0.80	26.4
1.0	32.2
1.2	38.2
1.6	49.5
2.0	61.7
2.4	69.1

Table 3.11. Second-order rate constants for reactions of **Ru^{II}~(COOH)** with phenoxyl radicals determined from the slope of plots of pseudo first-order rate constants versus phenoxyl radical concentration and y-intercepts (Figures 3.5, 3.6).

3.5.6.6 Reactions with TEMPO$^{\bullet}$.

Reaction	**Rate Constant, k_2 (M^{-1} s^{-1})**	**y-intercept, (s^{-1})**
Ru^{II}(bpy-COOH) + $^{t}Bu_3ArO^{\bullet}$	$2.0 \pm 0.4 \times 10^5$	5.1 ± 6.4
Ru^{II}(bpy-COOD) + $^{t}Bu_3ArO^{\bullet}$	$1.2 \pm 0.4 \times 10^5$	1.3 ± 4.9
Ru^{II}(bpy-Ph-COOH) + $^{t}Bu_3ArO^{\bullet}$	$1.7 \pm 0.4 \times 10^4$	0.95 ± 0.81
Ru^{II}(bpy-COOH) + $^{t}Bu_2OMeArO^{\bullet}$	$2.9 \pm 1.0 \times 10^4$	2.2 ± 1.5

3.5.6.6.1 Ru^{II}(bpy-COOH) + TEMPO•. A 0.23 M solution of TEMPO• in acetonitrile was prepared. A 3.0 mM stock solution of **Ru^{II}(bpy-COOH)** in acetonitrile was diluted to give 10 mL of a 48 μM solution. 10 μL of MeOD was added to 5.0 mL of this solution. The UV-vis spectra of each of these solutions were obtained and the concentration of each solution was calculated from the absorbance values. The solutions were each loaded and sealed in syringes with valves. The reactions of **Ru^{II}(bpy-COOH)** with TEMPO• and *in situ* generated **Ru^{II}(bpy-COOD)** with TEMPO• were monitored by single-mixing stopped-flow spectrophotometry. A ~5000-fold excess of TEMPO• is necessary to achieve reasonable yields of **Ru^{III}(bpy-COO)** and TEMPOH. Consequently, the absorbance of TEMPO• at 460 nm predominates the optical spectra throughout the course of the reaction (Figure 3.18A). The optical spectrum of 0.11 M TEMPO• can be subtracted from the initial and final optical spectra of the reaction at 0.076 s and 37.5 s to show the conversion of **Ru^{II}(bpy-COOH)** to **Ru^{III}(bpy-COO)** (Figure 3.18B). For the reaction of **Ru^{II}(bpy-COOH)** and TEMPO•, the **Ru^{II}(bpy-COOH)** is 85% consumed in 30 s. For the

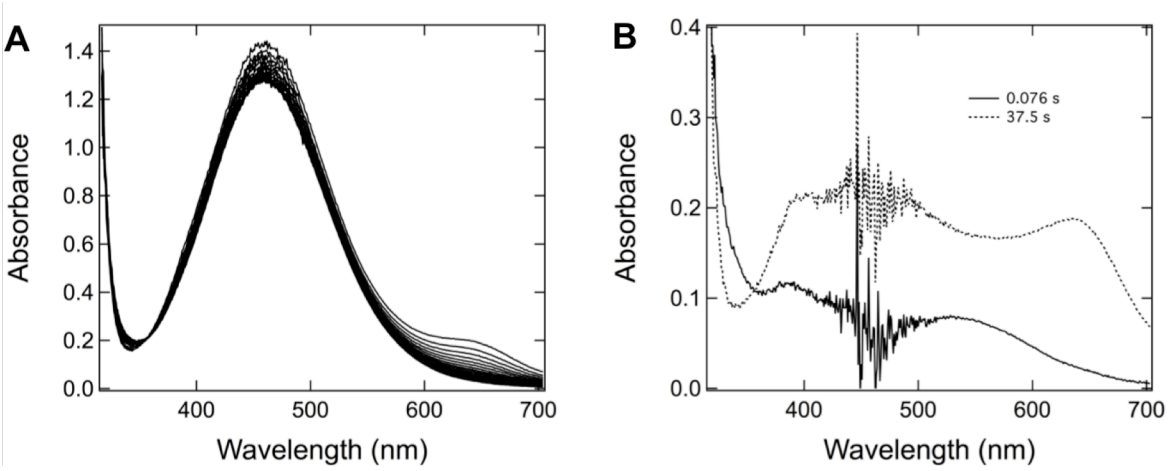

Figure 3.18A. Stacked optical spectra of the reaction of **Ru^{II}(bpy-COOH)** with TEMPO•.
Figure 3.18B. Optical spectra of the reaction of **Ru^{II}(bpy-COOH)** with TEMPO• at 0.076 s and 37.5 s minus the optical spectrum of 0.11 M TEMPO•.

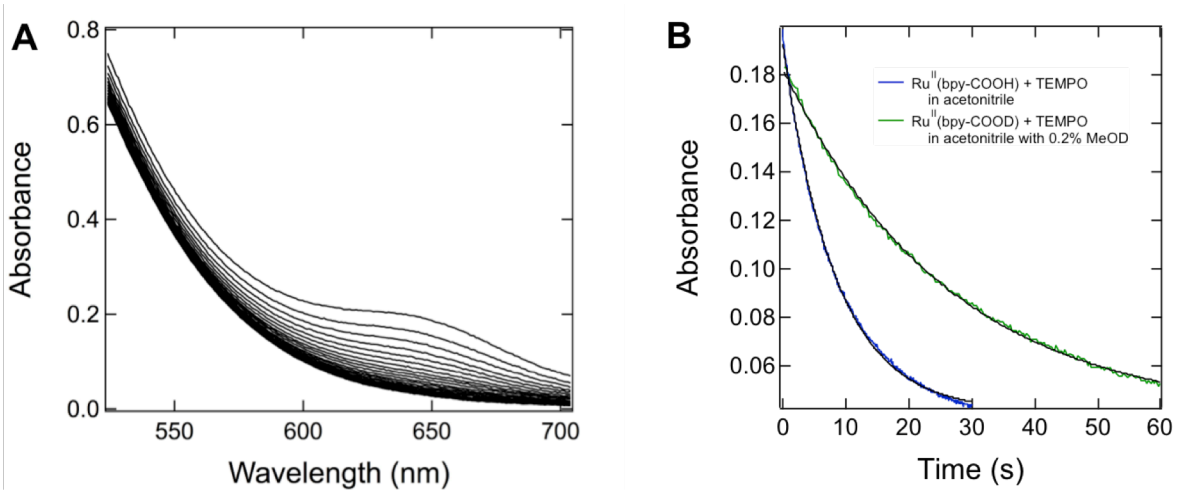

Figure 3.19A. Stacked truncated optical spectra of the reaction of **Ru^{II}(bpy-COOH)** with TEMPO$^{\bullet}$. **Figure 3.19B.** Absorbance at 650 nm versus time of the reactions of **Ru^{II}(bpy-COOH)** with TEMPO$^{\bullet}$ in acetonitrile (blue line) and **Ru^{II}(bpy-COOD)** with TEMPO$^{\bullet}$ in acetonitrile with 0.2% MeOD (green line), each superimposed with the second-order fit (black line).

reaction of *in situ* generated **Ru^{II}(bpy-COOD)** and TEMPO$^{\bullet}$, the **Ru^{II}(bpy-COOD)** is 74% consumed in 60 s.

The truncated spectra (524 nm – 700 nm, see Figure 3.19A) of the reactions as a function of time were analyzed with Specfit^{TM} global fitting software using a second-order equilibrium reaction model (Equations 3.11 and 3.12). Both the forward and reverse reactions were fit and the ratio k_2/k_{-2} was held constant at the equilibrium constant of the reaction (K_{eq} = 0.0022). The spectral changes over time and the fit to the kinetic trace at 650 nm are shown in Figure 3.19.

3.5.6.6.1 Ru^{II}(bpy-Ph-COOH) + TEMPO$^{\bullet}$. A 0.42 M solution of TEMPO$^{\bullet}$ in acetonitrile was prepared. A 0.92 mM stock solution of **Ru^{II}(bpy-Ph-COOH)** in acetonitrile was diluted and filtered through a pipet filter to give 8 mL of a 130 μM solution. The UV-vis spectrum of this solution was obtained and the concentration of the solution was calculated from the absorbance

values. 6 μL of MeOD-d_4 was added to 3.0 mL of this solution. The solutions were each loaded and sealed in syringes with valves. The reactions of **Ru^{II}(bpy-Ph-COOH)** with TEMPO$^{\bullet}$ and *in situ* generated **Ru^{II}(bpy-Ph-COOD)** with TEMPO$^{\bullet}$ were monitored by single-mixing stopped-flow spectrophotometry.

The truncated spectra (524 nm – 700 nm, see Figure 3.18A) of the reactions as a function of time were analyzed with Specfit^{TM} global fitting software using a second-order equilibrium reaction model (Equations 3.11 and 3.12). Both the forward and reverse reactions were fit and the ratio k_2/k_{-2} was held constant at the equilibrium constant of the reaction (K_{eq} = 0.000066). A good second-order equilibrium fit could not be obtained for the reaction of **Ru^{II}(bpy-Ph-COOD)** and TEMPO$^{\bullet}$, but the overlay of the kinetic traces show that the rates of the reaction of **Ru^{II}(bpy-Ph-COOH)** and **Ru^{II}(bpy-Ph-COOD)** are similar (Figure 3.18B). The spectral changes over time and the fit to the kinetic trace at 650 nm are shown in Figure 3.18.

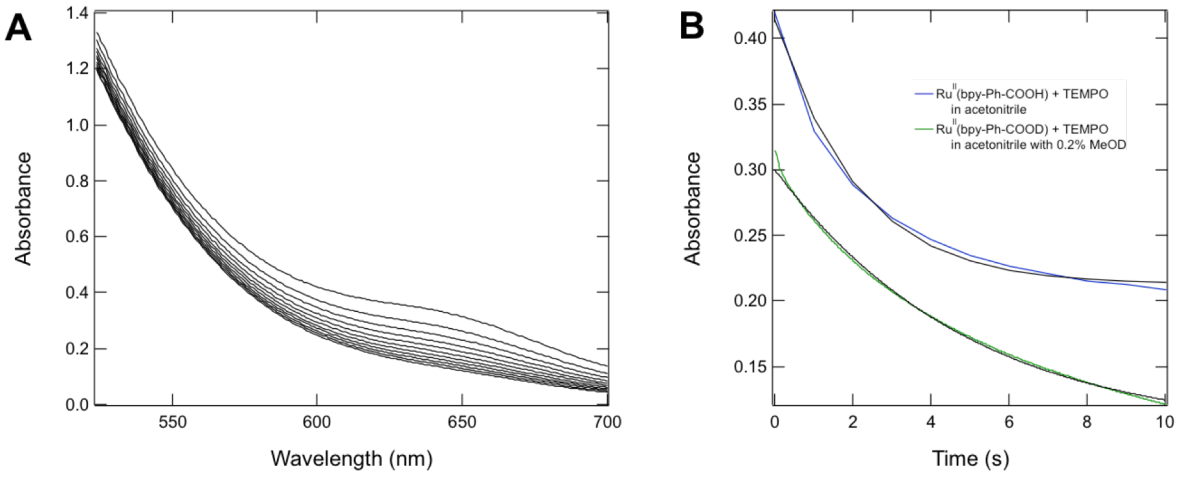

Figure 3.20A. Stacked truncated optical spectra of the reaction of **Ru^{II}(bpy-Ph-COOH)** with TEMPO$^{\bullet}$. **Figure 3.20B.** Absorbance at 650 nm versus time of the reactions of **Ru^{II}(bpy-Ph-COOH)** with TEMPO$^{\bullet}$ in acetonitrile (blue line) superimposed with the first-order fit (black line) and **Ru^{II}(bpy-Ph-COOD)** with TEMPO$^{\bullet}$ in acetonitrile with 0.2% MeOD (green line).

Notes to Chapter 3

(1) Closs, G. L.; Miller, J. R. *Science* **1988**, *240*, 440-447.
(2) Mclendon, G. *Acc. Chem. Res.* **1988**, *21*, 160-167.
(3) Gray, H. B.; Winkler, J. R. *Annu. Rev. Biochem.* **1996**, *65*, 537-561.
(4) Gray, H. B. *Abstr. Pap. Am. Chem. Soc.* **1988**, *195*, 274.
(5) Edwards, P. P.; Gray, H. B.; Lodge, M. T. J.; Williams, R. J. P. *Angewandte Chemie-International Edition* **2008**, *47*, 6758-6765.
(6) Stubbe, J.; Nocera, D.; Yee, C.; Chang, M. *Chem. Rev.* **2003**, *103*, 2167-2201.
(7) Yokoyama, K.; Smith, A. A.; Corzilius, B.; Griffin, R. G.; Stubbe, J. *J. Am. Chem. Soc.* **2011**, *133*, 18420-18432.
(8) Meyer, T. J.; Huynh, M. H. V.; Thorp, H. H. *Angew Chem Int Edit* **2007**, *46*, 5284-5304.
(9) Dempsey, J. L.; Winkler, J. R.; Gray, H. B. *Chem. Rev.* **2010**, *110*, 7024-7039.
(10) Weinberg, D. R.; Gagliardi, C. J.; Hull, J. F.; Murphy, C. F.; Kent, C. A.; Westlake, B. C.; Paul, A.; Ess, D. H.; McCafferty, D. G.; Meyer, T. J. *Chem. Rev.* **2012**, *112*, 4016-4093.
(11) Hammarstrom, L.; Styring, S. *Energy & Environmental Science* **2011**, *4*, 2379-2388.
(12) Zhang, M. T.; Irebo, T.; Johansson, O.; Hammarstrom, L. *J. Am. Chem. Soc.* **2011**, *133*, 13224-13227.
(13) Kuss-Petermann, M.; Wolf, H.; Stalke, D.; Wenger, O. S. *J. Am. Chem. Soc.* **2012**, *134*, 12844-12854.
(14) Chen, J.; Kuss-Petermann, M.; Wenger, O. S. *Chem. Eur. J.* **2014**, *20*, 4098-4104.
(15) Cukier, R. I.; Nocera, D. G. *Annu. Rev. Phys. Chem.* **1998**, *49*, 337-369.
(16) Kirby, J. P.; Roberts, J. A.; Nocera, D. G. *J. Am. Chem. Soc.* **1997**, *119*, 9230-9236.
(17) De Angelis, F.; Fantacci, S.; Selloni, A.; Nazeeruddin, M. K.; Gratzel, M. *J. Am. Chem. Soc.* **2007**, *129*, 14156-14157.
(18) Watson, D. F.; Marton, A.; Stux, A. M.; Meyer, G. J. *J. Phys. Chem. B* **2003**, *107*, 10971-10973.
(19) Qu, P.; Meyer, G. *Langmuir* **2001**, *17*, 6720-6728.
(20) Wang, Z. S.; Yamaguchi, T.; Sugihara, H.; Arakawa, H. *Langmuir* **2005**, *21*, 4272-4276.
(21) Wang, Z. S.; Zhou, G. *J. Phys. Chem. C* **2009**, *113*, 15417-15421.
(22) Hagfeldt, A.; Boschloo, G.; Sun, L. C.; Kloo, L.; Pettersson, H. *Chem. Rev.* **2010**, *110*, 6595-6663.
(23) Warren, J. J.; Tronic, T. A.; Mayer, J. M. *Chem. Rev.* **2010**, *110*, 6961-7001.
(24) Constable, E. C.; Dunphy, E. L.; Housecroft, C. E.; Neuburger, M.; Schaffner, S.; Schaper, F.; Batten, S. R. *Dalton Trans.* **2007**, 4323-4332.
(25) The Ru(II) and Ru(III) complexes are in rapid exchange, thus, a small amount of Ru(II) will shift the location of the Ru(III) signal, making it difficult to distinguish between protonated and deprotonated Ru(III) complexes. The integration of the phenolic proton signal of the phenol indicate that the proton has transferred.

(26) A signal at -22 ppm was also observed in the ^{1}H-NMR spectrum of independently synthesized Ru(III)(bpy-COO) in DMF-d_7, however, a spectrum in MeCN-d_3 was not obtained (see Section 3.5.4.5).

(27) The large estimated uncertainty associated with the second-order rate constants accounts for the large uncertainty associated with the equilibrium constant. However, the ratio of the rate constants of the reaction in acetonitrile with no added methanol and the reaction in acetonitrile with 0.2% MeOD does not change when different equilibrium constants are used to fit the data to a second-order equilibrium reaction model. Thus, the KIE is independent of the equilibrium constant.

(28) Costentin, C.; Evans, D.; Robert, M.; Saveant, J.; Singh, P. *J. Am. Chem. Soc.* **2005**, *127*, 12490-12491.

(29) Warren, J. J.; Menzeleev, A. R.; Kretchmer, J. S.; Miller, T. F.; Gray, H. B.; Mayer, J. M. *J. Phys. Chem. Lett.* **2013**, *4*, 519-523.

(30) Manner, V. W.; Mayer, J. M. *J. Am. Chem. Soc.* **2009**, *131*, 9874-9875.

(31) Manner, V. W. Concerted Proton-Electron Transfer Reactions of Ruthenium and Cobalt Complexes: Studies on Distance Dependence and Spin Effects. PhD, University of Washington, Seattle, WA, 2009.

(32) Manner, V. W.; DiPasquale, A. G.; Mayer, J. M. *J. Am. Chem. Soc.* **2008**, *130*, 7210-7211.

(33) Marcus, R. A.; Sutin, N. *Biochim. Biophys. Acta* **1985**, *811*, 265-322.

(34) Mayer, J. *Annu. Rev. Phys. Chem.* **2004**, *55*, 363-390.

(35) Mayer, J. M. *Acc. Chem. Res.* **2011**, *44*, 36-46.

(36) Mader, E.; Larsen, A.; Mayer, J. *J. Am. Chem. Soc.* **2004**, *126*, 8066-8067.

(37) Waidmann, C. R.; Zhou, X.; Tsai, E. A.; Kaminsky, W.; Hrovat, D. A.; Borden, W. T.; Mayer, J. M. *J. Am. Chem. Soc.* **2009**, *131*, 4729-4743.

(38) Roth, J. P.; Yoder, J. C.; Won, T. J.; Mayer, J. M. *Science* **2001**, *294*, 2524-2526.

(39) Schrauben, J. N.; Cattaneo, M.; Day, T. C.; Tenderholt, A. L.; Mayer, J. M. *J. Am. Chem. Soc.* **2012**, *134*, 16635-16645.

(40) Markle, T. F.; Rhile, I. J.; Mayer, J. M. *J. Am. Chem. Soc.* **2011**, *133*, 17341-17352.

(41) Chou, M. C., C.; Sutin, N. *J. Am. Chem. Soc.* **1977**, *99*, 5615-5623.

(42) Baird, I.; Rettig, S.; James, B.; Skov, K. *Can. J. Chem.* **1999**, *77*, 1821-1833.

Chapter 4

A C-C Bonded Phenoxyl Radical Dimer with a Zero Bond Dissociation Free Energy

4.1 Introduction

Weak chemical bonds have long attracted interest as they test aspects of chemists' intuition regarding the nature of bonding and relationships among bond strength, bond length and other parameters, developed in particular by Pauling.[1-4] Many correlations between these parameters have been proposed. For example, Zavitsas described a linear correlation of C–C bond lengths and bond strengths over a >200 kcal mol^{-1} range.[1] The long-standing Badger's rule relates bond length and force constant, which is closely related to bond strength.[2] We describe here the characterization of a phenoxyl radical dimer with an extremely weak C–C bond.

Phenoxyl radicals are important in biology, in natural and synthetic antioxidant chemistry, and are increasingly studied in radical and proton-coupled electron transfer (PCET) reactions.[8] Phenoxyl radicals that are protected at the 2, 4 and 6-positions, such as 2,6-di-*tert*-butyl-4-methoxy-phenoxyl radical (**^{t}Bu$_2$(MeO)ArO$^\bullet$**), are unusually stable in oxygen-free solutions.[9] In 1955, Mueller and Ley found that the radical content of **^{t}Bu$_2$(MeO)ArO$^\bullet$** is not quantitative by magnetic susceptibility, and proposed equilibrium formation of the 4-4′-bis-cyclohexadienone dimer (**(^{t}Bu$_2$(MeO)ArO)$_2$** (Figure 4.1).[10] Reported here are the X-ray crystal structure of the dimer and dissociation thermochemistry of its weak C-C bond. This study has been previously published.[11]

4.2 Results

4.2.1 Preparation and Characterization of (^{t}Bu$_2$(MeO)-ArO)$_2$. **^{t}Bu$_2$(MeO)ArO$^\bullet$** was prepared by treating 2,6-di-*tert*-butyl-4-methoxyphenol with potassium ferricyanide in a biphasic medium of benzene and 1 M aqueous sodium hydroxide, following a related procedure.[12] The resulting purple oil was crystallized from dry, oxygen-free acetonitrile at -30 °C forming light yellow crystals.[13] An IR spectrum of the isolated dimer crystals, obtained as a KBr pellet, shows two strong IR stretches at 1646 cm^{-1} and 1667 cm^{-1} (Figure 4.2A) The X-ray crystal structure revealed the *para*-coupled dimer (Figure 4.1B).[14] The dimer lies on a crystallographic inversion center in the monoclinic *C*2/*c* space group. To our knowledge, this is the first X-ray crystal structure reported for a *para*-coupled phenoxyl radical dimer.

4.2.2 Determination of the Equilibrium Constant for Dimer Dissociation. The equilibrium constant for dimer dissociation (K_{eq}) at 20 ± 2 °C was determined by solution IR spectroscopy in CCl_4. At low concentrations only the monomer **^{t}Bu$_2$(MeO)ArO$^\bullet$** was observed, while at ≥50 mM the dimer was evident from its bands at 1646 cm^{-1} and 1667 cm^{-1} (Figure 4.2B). The concentrations of **^{t}Bu$_2$(MeO)ArO$^\bullet$** in solutions where both monomer and dimer were present was determined from the relatively weak extinction coefficient at 1292 cm^{-1} (Figure 4.11).[15] The

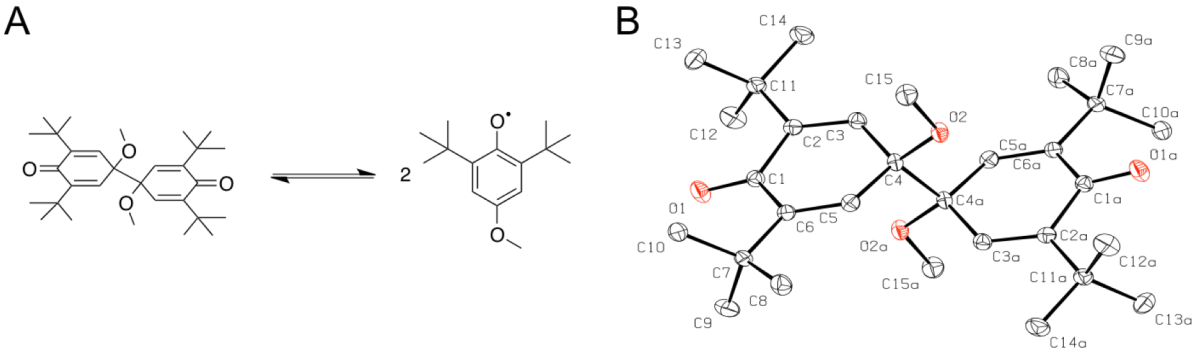

Figure 4.1A. Dissociation of **(^{t}Bu$_2$(MeO)ArO)$_2$** dimer to **^{t}Bu$_2$(MeO)ArO$^\bullet$**. **Figure 4.1B.** ORTEP of the X-ray crystal structure of the dimer.

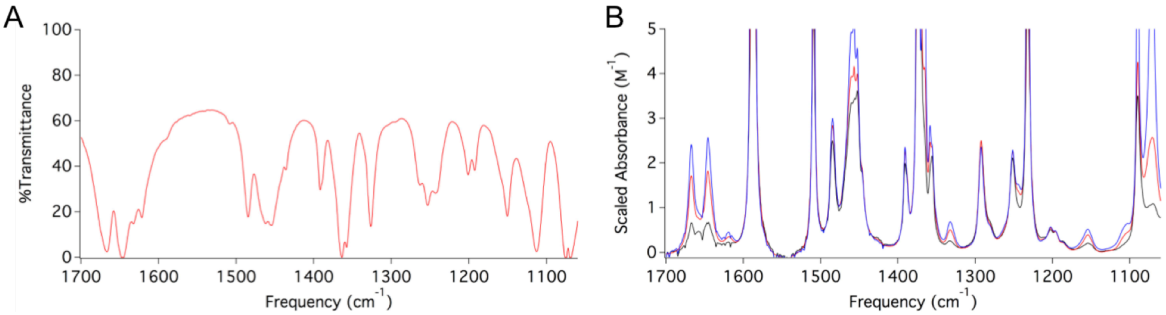

Figure 4.2A. IR transmittance spectrum of solid dimer (as a KBr pellet prepared in a glove box). **Figure 4.2B.** IR spectra of CCl_4 solutions of **^{t}Bu$_2$(MeO)ArO$^\bullet$** at 50 mM (black), 250 mM (red), and 500 mM (blue). The vertical axial is the absorbance divided by the [**^{t}Bu$_2$(MeO)ArO$^\bullet$**] in each solution, determined from the absorbance at 1292 cm^{-1} (Figure 4.11).

dimer concentrations were then calculated using mass balance. Fitting the data to the equilibrium in Figure 4.1 gave K_{eq} = 1.3 ± 0.2 M at 20 °C (Figure 4.13). This corresponds to a free energy of -0.15 ± 0.1 kcal mol^{-1}.

4.2.3 Determination of the Bond Dissociation Enthalpy of the Weak C-C Bond. Equilibrium constants at temperatures from –20 to +20 °C were determined by measuring the optical absorbance of **^{t}Bu$_2$(MeO)ArO$^\bullet$** in CCl_4 solutions (Figure 4.3). For concentrated solutions, 1- or 2-mm pathlength cuvettes were used and the absorbance of **^{t}Bu$_2$(MeO)ArO$^\bullet$** was measured at 605 nm rather than at the peak maximum. A plot of absorbance *vs.* [**^{t}Bu$_2$(MeO)ArO$^\bullet$**] for dilute (<20 mM) solutions of **^{t}Bu$_2$(MeO)ArO$^\bullet$** at 22 ± 1 °C was linear with ε = 44 M^{-1} cm^{-1} at 605 nm (Figure 4.6). At concentrations above 20 mM and at lower temperatures, such Beer's Law plots were non-linear, suggesting loss of **^{t}Bu$_2$(MeO)ArO$^\bullet$** to form the dimer (Figure 4.7). The data are well fit by the equilibrium in Figure 4.1, with the assumption of mass balance (Figure 4.8, Table 4.4). The K_{eq} at 20 °C was found to be 1.4 ± 0.3 M^{-1}, in excellent agreement with the value from the IR study. A van't Hoff plot of the K_{eq} values from –20 to +20 °C (Figure 4.3A; Table 4.4)

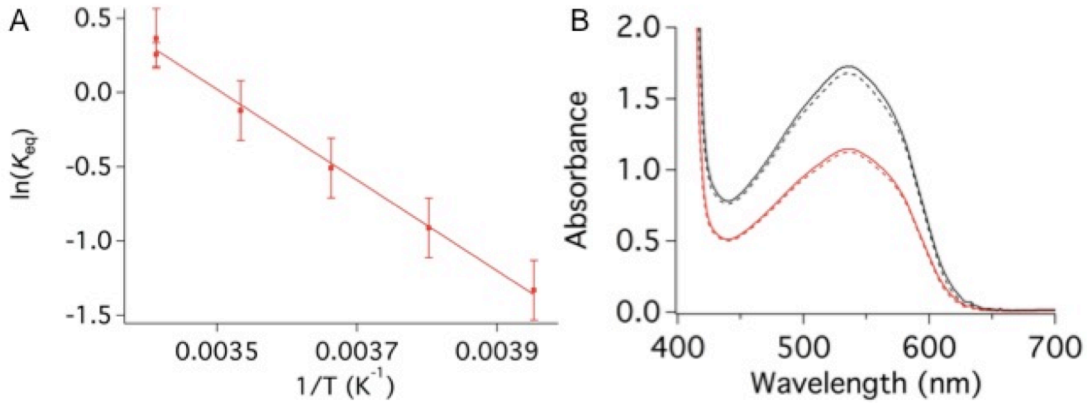

Figure 4.3A. Van't Hoff plot for dissociation of dimer. **Figure 4.3B.** UV-vis spectra of 10 mM (black) and 6 mM (red) **^{t}Bu$_2$OMeArO$^\bullet$** in CCl_4 at 20 °C (solid line) and -20 °C (dashed line).

gives the enthalpy and entropy of dimer dissociation: $\Delta H° = 6.1 \pm 0.5$ kcal mol^{-1} and $\Delta S° = 21 \pm 1$ cal mol^{-1} K^{-1}.

4.2.4 Density Functional Theory Calculations of (^{t}Bu$_2$(MeO)ArO)$_2$. DFT calculations were performed using the M06-2X functional and 6-31G*, 6-31+G**, and 6-31+G(2d,2p) basis sets.[16] The M06-2X functional was chosen because it accounts for long-range non-covalent interactions that can be an important factor in long C-C bonds. All basis sets provided similar results. Larger basis sets gave results in greater agreement with the experimental C4-C4a bond length, BDE, and IR frequencies, in particular. The C4-C4a bond lengths and BDEs provided by calculations using the B3LYP functional were in poor agreement with experiment. Geometry optimization calculations were performed for both the dimer and monomer. The optimized geometries for the dimer and monomer are tabulated (Tables 4.6 and 4.7, respectively) and absolute energies are reported in Table 4.1. A wavefunction stability test (Stable=Opt) indicated that both geometries were stable. Frequency calculations and thermochemical analyses were performed for the dimer and monomer. All geometries were

Table 4.1 Comparison of calculated parameters using M-06/2X with various basis sets and experimental values.

	6-31G*	**6-31+G****	**6-31+G(2d,2p)**	**Experiment**
Absolute Energy of Dimer (Hartrees)	-1471.08523502	-1471.16740116	-1471.23572129	-
Absolute Energy of Monomer (Hartrees)	-735.532518464	-735.574197421	-735.608646282	-
Absolute Energy of Single Point (Hartrees)	-735.475621360	-735.520594749	-735.554665529	-
C4-C4a Bond Length (Å)	1.6104	1.6079	1.6065	1.6055(23)
Zero-point Vibrational Energy of Dimer (kcal mol^{-1})	447.64914	444.10843	443.61766	-
Zero-point Vibrational Energy of Monomer (kcal mol^{-1})	222.95717	221.30382	220.98698	-
Zero-point Vibrational Energy of Single Point (kcal mol^{-1})	220.94276	219.94235	219.68701	-
Sum of electronic and thermal Enthalpies of Dimer (Hartrees)	-1470.332562	-1470.420008	-1470.489101	-
Sum of electronic and thermal Enthalpies of Monomer (Hartrees)	-735.157899	-735.202130	-735.237037	-
Sum of electronic and thermal Enthalpies of Single Point (Hartrees)	-735.103646	-735.150899	-735.185360	-
Bond Dissociation Enthalpy (kcal mol^{-1})	10.5	9.9	9.4	6.1
Stabilization Energy (kcal mol^{-1})	68.1	64.3	64.9	-
Bond Dissociation Free Energy at 293 K (kcal mol^{-1})	-2.0	-1.7	-2.3	-0.15
Total Entropy of Dimer (cal mol^{-1} K^{-1})	226.900	230.781	230.982	-
Total Entropy of Monomer (cal mol^{-1} K^{-1})	134.850	135.238	135.557	-
Force Constant (mDynes/Å)	3.607	3.57	3.59	-

confirmed to be local minima by IR frequency analysis (Table 4.1). The calculated force constant in internal coordinates of the C4-C4a bond of the dimer was determined from the frequency calculation and converted from Hartrees/($a_\circ^2$) to mDynes/Å (Table 4.1). The calculated sums of electronic and thermal enthalpies for the dimer and monomer were used to calculate the bond dissociation enthalpy (BDE) of the C4-C4a bond in the dimer (Table 4.1). The zero-point vibrational energies and calculated Gibbs free energy at 293 K (the temperature of the experiment) are also reported in Table 4.1. To estimate the stabilization energy of the dissociated dimer rearranging to the geometry of the monomer, a single point energy calculation was performed on the monomer with a geometry identical to half of the optimized dimer geometry. This is the geometry of the monomer after the dimer bond dissociation, but before relaxation to the monomer geometry. The absolute energy at this geometry is reported in Table 4.1. The calculated sums of electronic and thermal enthalpies were used to calculate the stabilization energy (Table 4.1).

4.3 Discussion

4.3.1 X-ray Crystal Structure of the Dimer. The bis-cyclohexadienone structure was proposed by Mueller and Ley based on quinone-like stretches at ~1600 cm^{-1} and ~1650 cm^{1} in the solution IR spectrum of **^{t}Bu$_2$(MeO)ArO$^\bullet$**. The X-ray crystal structure reported here verifies that proposal.[10] The metrical data for the structure of **(^{t}Bu$_2$(MeO)ArO)$_2$** (Table 4.2) are consistent with the line structure in Figure 4.1A. The C1–O1 bond length of 1.2227(15) is characteristic of a C=O double bond. The 1.34 Å C2–C3 and C5–C6 bond distances are typical of C=C double bonds, while the C1-C2, C3-C4, C4-C5, and C6-C1 bond distances are slightly longer than 1.47 Å sp^3-sp^2 single bonds. The carbon-carbon bond connecting the two halves of the dimer, C4–C4a, is 1.6055(23) Å, which is much longer than the standard 1.54 Å sp^3-sp^3 bond distance.[17]

The recently reported structure of the 9,10-dialkoxyanthracene radical cation dimer has a 1.637(5) Å C–C bond,[18] and C-C bond lengths of other similar structures range from 1.59 – 1.64 Å.[6,19]

Table 4.2 Comparison of crystallographic and calculated metrical data (Å, °) for **(^{t}Bu$_2$(MeO)ArO)$_2$** and its monomer.

Bond	X-ray Structure	M06-2X/6-31+G(2d,2p)	
		dimer	monomer
C1-O1	1.2227(15)	1.215	1.244
C1-C2	1.5026(16)	1.503	1.470
C2-C3	1.3377(17)	1.335	1.378
C3-C4	1.4955(16)	1.497	1.403
C4-C5	1.4989(16)	1.497	1.411
C5-C6	1.3371(17)	1.335	1.367
C6-C1	1.5005(16)	1.503	1.474
C4-O2	1.4297(14)	1.413	1.342
C4-C4a	1.6055(23)	1.6065	-
Dihedral angle (C2,C3,C4,O2)	142.0	145.9	180.0

4.3.2. Comparison of Experimental and Calculated Parameters. DFT calculations of the dimer (M06-2X/6-31+G(2d,2p)) gave gas-phase bond lengths in close agreement with measured solid-state distances (Table 4.2). The computed C4–C4a bond length is of 1.6065 Å is within 1σ of the measured distance. The calculated gas-phase vibrational frequencies are less close to the measured frequencies (Figures 4.9 and 4.10, Table 4.5). For instance, the C=O/C=C stretching frequencies are calculated to be 1629, two doubly degenerate signals at 1660, and 1690 cm^{-1}, versus 1622, 1632, 1646 and 1667 cm^{-1} both in the solid state (KBr pellet) and in solution (CCl_4) (Table 4.5).

4.3.3 Comparison of the Weak C-C Bond Dissociation Enthalpy to Related Systems. **(^{t}Bu$_2$OMeArO)$_2$** has an extremely weak C–C bond, with a bond dissociation enthalpy (BDE) of 6.1 kcal mol^{-1}. To our knowledge, this is the weakest C–C bond that has been experimentally measured. It is ≥8 kcal mol^{-1} weaker than the BDE estimates of Mahoney and Weiner for less crowded phenoxyl radical dimers.[20] Gomberg's triphenylmethyl radical forms a stronger C–C bond (BDE = 11 kcal mol^{-1}) and is only slightly dissociated in concentrated solutions.[21] Phenalenyl radical dimers with BDEs of 9.5 – 14 kcal mol^{-1} have been described.[22] Scaiano *et al.* have reported BDEs of 15-26 kcal mol^{-1} for dimers of stabilized carbon-centered radicals with similar C–C bond distances.[6] A formally iron(I)-pyridine complex was recently found to undergo reversible coupling to a 4,4'-dimer, with a BDE likely similar to that in Gomberg's dimer.[23] More bulky derivatives such as (4-^{t}BuPh)$_3$C$^{\bullet}$[24] and 2,4,6-^{t}Bu$_3$C$_6$H$_2$O$^{\bullet}$ do not dimerize and therefore must form weaker C–C bonds than **^{t}Bu$_2$(MeO)ArO$^{\bullet}$**.

The C–C bond in **(^{t}Bu$_2$OMeArO)$_2$** is much weaker than would have been expected based on its bond distance of 1.6055(23) Å. A linear correlation between C–C bond length and BDE has been proposed (Figure 4.4A).[1] It would predict a BDE of >50 kcal mol^{-1} for this bond length, or a bond length of >1.7 Å for such a weak C–C bond. Other deviations have been reported and discussed.[25] Also included are recently reported alkanes with long C-C bonds (up to 1.71 Å) but high attractive dispersion forces, which deviate from the correlation in the opposite direction.[7]

The deviation of **(^{t}Bu$_2$OMeArO)$_2$** from this correlation is likely due to the large stabilization energy of the monomeric phenoxyl radical associated with structural rearrangements upon dissociation.[6,22,26] This stabilization energy was computed using a single point calculation of the **^{t}Bu$_2$(MeO)ArO$^{\bullet}$** monomer at the optimized geometry of the dimer.[27] Allowing the two phenoxyl radicals to relax from this point to their equilibrium structures is downhill by 64.9 kcal mol^{-1}.

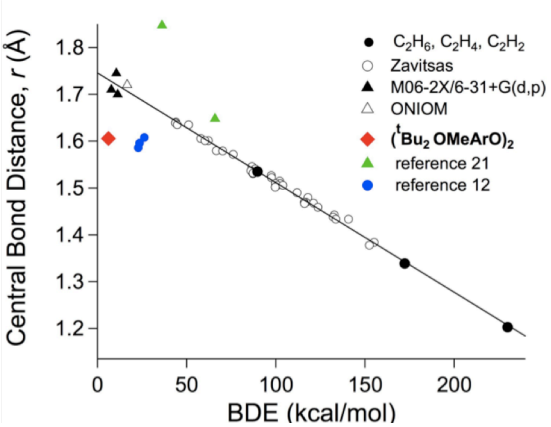

Figure 4.4. Plot of central C–C bond distances *r* (Å) *vs.* bond dissociation enthalpies (BDEs, kcal mol^{-1}), adapted from references[1] with data for **(^{t}Bu$_2$OMeArO)$_2$** added (red diamond). Experimental values from Zavitsas are shown as circles, with C_2H_6, C_2H_4, C_2H_2 highlighted as black circles;[1a] triangles are calculated values;[1b] blue circles and green triangles are from [6] and [7].

Similar arguments and stabilization energies have been described by Scaiano and by Kochi and Head-Gordon for carbon-centered radical dimers.[6,22] The calculated *vertical* bond energy of 74.3 kcal mol^{-1} is only slightly larger than the bond energy predicted from Zavitsas' linear correlation (Figure 4.4). The large stabilization energy is a result of the substantial structural difference between the dimer and monomer, particularly in the high frequency C–C and C–O bonds (Table 4.2).

The force constant of the central C-C bond of **(^{t}Bu$_2$OMeArO)$_2$** was obtained from the DFT calculations. Badger's rule relates bond lengths r_e to force constants k_e according to $r_e = (C_{ij}/k_e)^{1/3} + d_{ij}$ where C_{ij} and d_{ij} are constants for a set of similar bonds.[2,5] The Badger's rule plot in Figure 4.5 shows, remarkably, that the r_e,k_e pair falls right on the line formed by the values for simple hydrocarbons.

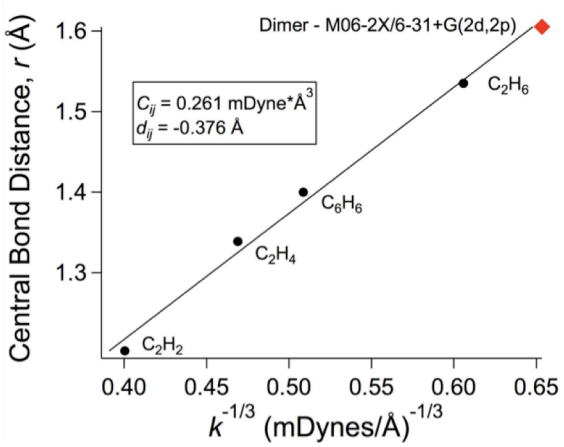

Figure 4.5. Badger's rule plot for the C–C bonds in C_2H_6, C_2H_4, C_2H_2, C_6H_6 (black circles; experimental data[5]) and the central C–C bond in **(^{t}Bu$_2$OMeArO)$_2$** (red diamond; experimental bond distance and calculated force constant (see Table 4.3)).

Table 4.3 Experimental bond lengths and bond dissociation energies (BDEs) and experimental and calculated force constants of C-C bonds in ethane, ethene, ethyne, benzene, and the dimer.

	Bond Length (Å)	**BDE (kcal mol^{-1})**	**Force Constant (mDyne/Å)**
H_3C-CH_3	1.5351[a]	89.68[a]	4.5[b]
H_2C=CH_2	1.339[a]	172.2[a]	9.7[b]
HC≡CH	1.203[a]	229.9[a]	15.6[b]
C_6H_6	1.39[c]		7.6[b]
Dimer C4-C4a bond	1.6055(23)[d]	6.1[e]	3.6[f]

[a]ref[1a]. [b]ref[5]. [c]ref[17]. [d]Crystallographic value. [e]Determined from van't Hoff plot. [f]M06-2X/6-31+G(2d,2p).

Thus the long bond length in **(^{t}Bu$_2$OMeArO)$_2$** correlates with the C–C bond force constant but not its bond dissociation enthalpy (BDE). Therefore the force constant does not correlate with the BDE. The bond length and force constant are both properties of the equilibrium structure of **(^{t}Bu$_2$OMeArO)$_2$** while the BDE also involves the energetics of the phenoxyl radical. The exceptionally weak C–C bond in **(^{t}Bu$_2$OMeArO)$_2$** – with a measured bond dissociation enthalpy of 6.1 kcal mol^{-1} – is due only in part to an intrinsically poor C–C bond. The C–C bond length of

1.6055(23) Å is longer than the typical 1.54 single bond distance, but is not long enough to explain the bond weakness. The low BDE is in large part due to be the substantial reorganization of the phenoxyl radical. This causes the substantial deviation from the suggested bond length/bond strength correlation.

4.4 Conclusion.

The 2,6-di-*tert*-butyl-4-methoxy-phenoxyl radical is shown to dimerize in solution and in the solid state. The X-ray crystal structure for the dimer, the first for a *para*-coupled phenoxyl radical, reveals a bond length of 1.6055(23) Å for the C4–C4′ bond. This is significantly longer than typical C–C bonds. Solution equilibrium studies using both optical and IR spectroscopies show that the K_{eq} for dissociation is 1.3 ± 0.2 M at 20 °C, indicating a C–C bond dissociation free energy of –0.15 ± 0.1 kcal mol^{-1}. Van't Hoff analysis gives an exceptionally small bond dissociation enthalpy (BDE) of 6.1 ± 0.5 kcal mol^{-1}. To our knowledge, this is the weakest BDE measured for a C–C bond. This very weak bond shows a large deviation from the correlation of C–C bond lengths and strengths, but the computed force constant follows Badger's rule.

4.5 Experimental Section.

4.5.1 General Considerations. All manipulations were carried out under nitrogen using glove-box/vacuum line techniques unless otherwise noted. Potassium ferricyanide, diethyl ether, and anhydrous carbon tetrachloride were purchased from Aldrich and used as received. Benzene, sodium hydroxide, and potassium bromide were purchased from EMD Millipore, Macron Chemical, and Fisher, respectively, and used as received. Anhydrous acetonitrile (MeCN; <10 ppm H2O) was purchased from Honeywell Burdick & Jackson, sparged with argon, and plumbed from a steel keg directly into a glovebox. 2,6-di-*tert*-butyl-4-methoxyphenol was

purchased from Aldrich and recrystallized from ethanol before use. Elemental analysis was performed by Complete Analysis Laboratories, Inc.

4.5.2 Spectroscopic Measurements. All samples were prepared under N_2, unless otherwise noted. UV-visible spectra were obtained with a Hewlett-Packard 8453 diode-array spectrophotometer. IR spectra were obtained using a Bruker Tensor 27 spectrophotometer.

4.5.3 Synthesis and Characterization of the Dimer. The synthesis of 2,6-di-*tert*-butyl-4-methoxyphenoxyl radical (**^{t}Bu$_2$OMeArO$^\bullet$**) was performed following literature procedures.[12] 10.8 g (0.0328 mol) of potassium ferricyanide was added to a frozen, degassed biphasic mixture of ^{t}Bu$_2$OMeArOH in benzene (0.11 M, 120 mL) and sodium hydroxide in water (1 M, 45 mL) under a N_2 atmosphere. The solution was left to stir for 2 hours at room temperature. The water layer was then removed with a syringe and the benzene layer was removed *in vacuo*. The product was extracted into diethyl ether and isolated by filtration and removal of solvent *in vacuo*, resulting in a purple oil. The spectra of this material matched the previously reported values. **^{t}Bu$_2$OMeArO$^\bullet$** was dissolved in dry acetonitrile to give a deep purple solution, from which pale yellow crystals formed in the dark at -30 °C over days. The identity of the crystals as the dimer (**^{t}Bu$_2$OMeArO$^\bullet$**)$_2$ was confirmed by X-ray crystallography and elemental analysis. Anal. (Calc.) C: 76.47 (76.55) H: 9.91 (9.85).

4.5.4 Determination of K_{eq} by UV-vis Measurements. A 0.10 M stock solution of **^{t}Bu$_2$OMeArO$^\bullet$** in carbon tetrachloride (CCl_4) was prepared in the glove box. The stock solution was diluted to give concentrations between 2 mM and 0.1 M and transferred to Kontes or septum-capped cuvettes. A 1-mm pathlength Kontes cuvette was used for concentrations above 0.08 M and a 2-mm pathlength Kontes cuvette was used for concentrations from 0.04-0.06 M. Variable temperature UV-vis spectra were obtained using a Hewlett-Packard 8453 diode array

spectrophotometer with a Unisoku sample holder with a temperature controller. The absorbance at 605 nm was monitored in order to access higher **^{t}Bu$_2$OMeArO$^\bullet$** concentrations. Figure 4.6 shows a Beer's Law plot of the absorbance at 605 nm for dilute solutions of **^{t}Bu$_2$OMeArO$^\bullet$** in CCl_4 at room temperature. An extinction coefficient of $\varepsilon_{605\ nm} = 44 \pm 5\ M^{-1}\ s^{-1}$ was determined. Figure 4.7 shows the deviation from Beer's Law for solutions of **^{t}Bu$_2$OMeArO$^\bullet$** at higher concentrations and lower temperatures. The absorbance values have been corrected for the different baselines of the different pathlength UV-vis cuvettes. The equilibrium constant for the dissociation of the dimer was determined by plotting the monomer concentration measured by UV-vis spectroscopy versus the [total]/[monomer] where [total] is the concentration of monomer if it was 100% dissociated (Equation 4.1, Figure 4.8). This relationship assumes a mass balance and that no precipitate is formed. Table 4.4 shows the slope and y-intercept values of the linear fit and the K_{eq} values for each temperature.

$$K_{eq} = \frac{[\text{monomer}]^2}{[\text{dimer}]} \tag{4.1}$$

$$[\text{total}] = [\text{monomer}] + 2[\text{dimer}] \tag{4.2}$$

$$\frac{[\text{total}]}{[\text{monomer}]} = \frac{2}{K_{eq}}[\text{monomer}] + 1 \tag{4.3}$$

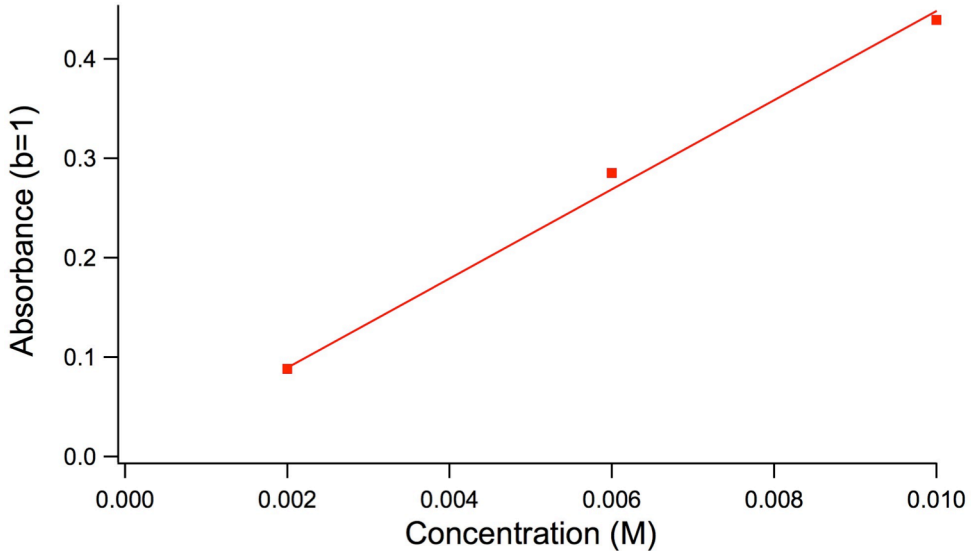

Figure 4.6. Beer's Law plot of ^{t}**Bu$_2$OMeArO$^{\bullet}$** absorbance at 605 nm. The cell pathlength, b, was 1 cm for these solutions.

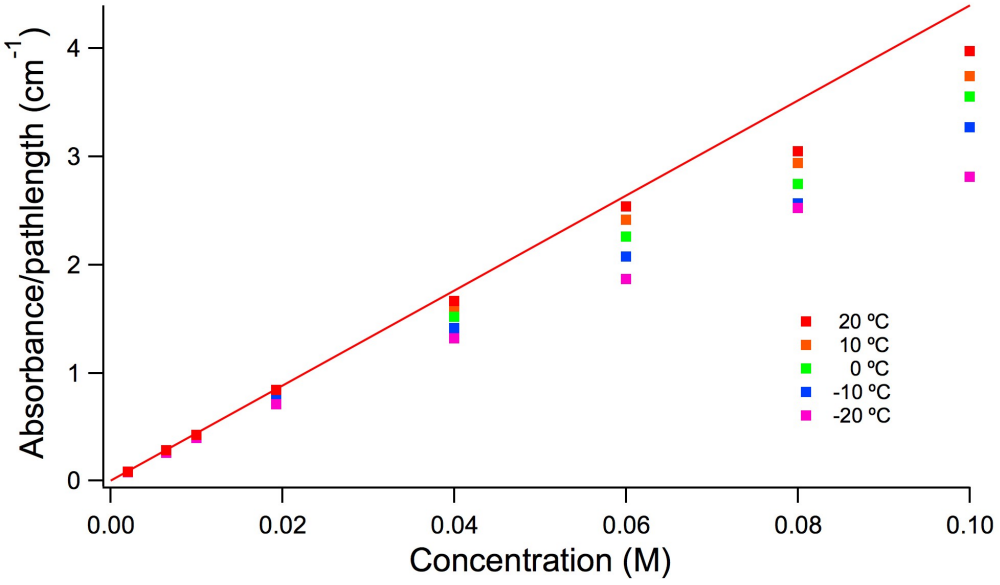

Figure 4.7. Deviation from Beer's Law of solutions of ^{t}**Bu$_2$OMeArO$^{\bullet}$** at various temperatures. The slope of the red line is the ε_{605nm} determined from Figure 4.6.

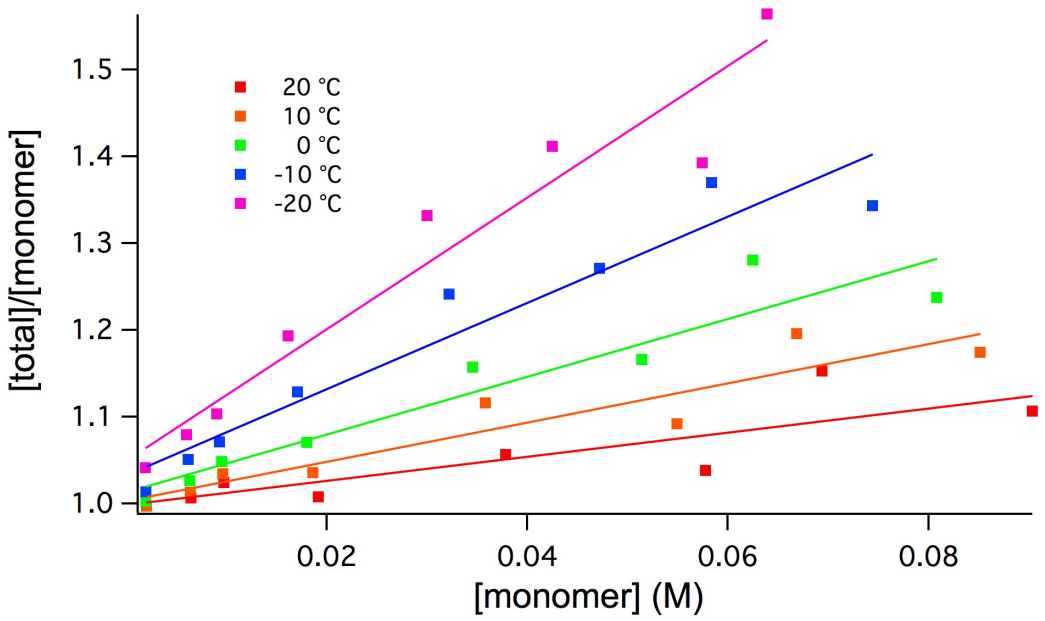

Figure 4.8. Plot of [monomer] vs. [total]/[monomer] for K_{eq} determination at temperatures 20 °C, 10 °C, 0 °C, -10 °C, and -20 °C.

Table 4.4. Slope and y-intercepts of the linear fits to the [total]/[monomer] vs. [monomer] plots and K_{eq} values for dimer dissociation each temperature.

Temperature (°C)	Slope (M^{-1})	y-intercept	K_{eq} (M^{-1})
20	1.4 ± 0.4	1.00 ± 0.02	1.44 ± 0.3
10	2.3 ± 0.3	1.00 ± 0.02	0.89 ± 0.2
0	3.3 ± 0.5	1.01 ± 0.02	0.60 ± 0.09
–10	5.0 ± 0.6	1.03 ± 0.02	0.40 ± 0.05
–20	7.6 ± 0.8	1.05 ± 0.03	0.26 ± 0.03

4.5.5 IR Methods for Characterization and Determination of K_{eq}. IR spectra were obtained using a Bruker Tensor 27 spectrophotometer. Background scans were collected after purging the sample chamber with nitrogen for 5 minutes. Sample scans were taken at 2 second intervals while purging with nitrogen. For each sample, the sample scan in which the carbon dioxide stretch near 3600 cm^{-1} was substracted out by the background was used.

4.5.5.1 Solid-state IR. A potassium bromide pellet of the dimer was prepared in the glove box and quickly removed to obtain an IR spectrum (Figure 4.2A).

4.5.5.2 Solution IR. Solutions of **^{t}Bu$_2$OMeArO$^\bullet$** in CCl_4 were prepared and transferred to a PTFE-capped solution IR cell. A Beer's Law plot was generated for the absorbance of **^{t}Bu$_2$OMeArO$^\bullet$** at 1292 cm^{-1} at low concentrations (40 – 90 mM) for which the dimer IR signals are small (Figure 4.11). The extinction coefficient at 1292 cm^{-1} was used to calculate the [**^{t}Bu$_2$OMeArO$^\bullet$**] because the dimer has a relatively small extinction coefficient at this wavelength. Beer's Law plots for the absorbance of the dimer at 1646 cm^{-1} and 1667 cm^{-1} were also generated (Figure 4.12). The dimer concentrations used in the Beer's Law plots were calculated using the experimentally determined [**^{t}Bu$_2$OMeArO$^\bullet$**] and assuming a mass balance. The extinction coefficients at 1646 cm^{-1} and 1667 cm^{-1} were used to calculate the actual [dimer]. The equilibrium constant for dimer dissociation (K_{eq}) was determined by plotting [**^{t}Bu$_2$OMeArO$^\bullet$**]^2 vs. [dimer] (Figure 4.13). The K_{eq} was determined to be 1.29 ± 0.03 M.

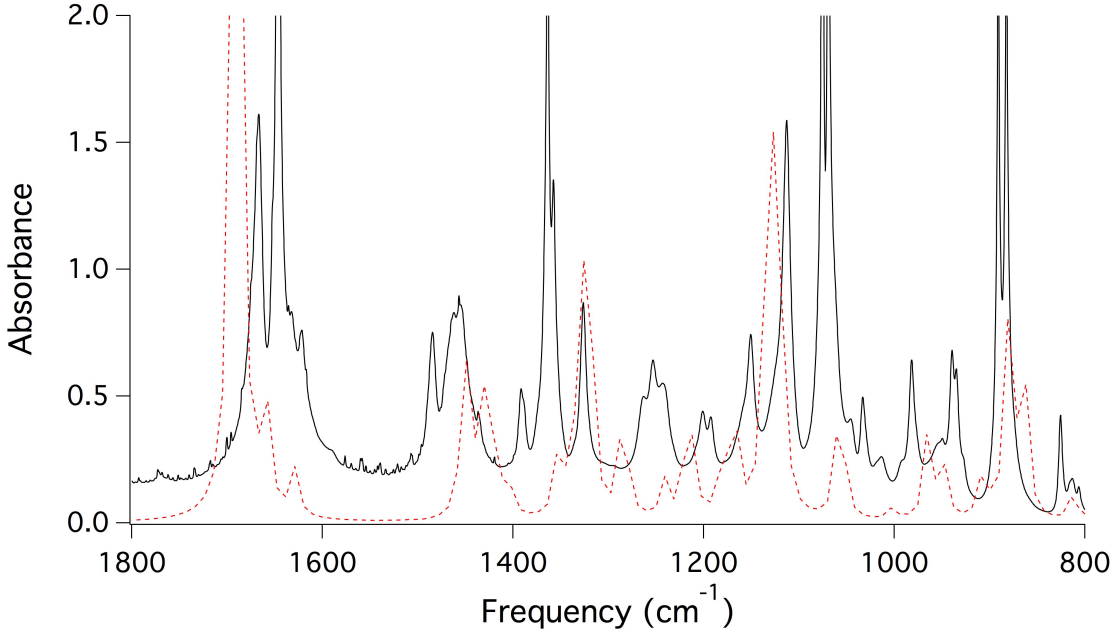

Figure 4.9. Solid state IR spectrum of dimer (black solid line) and IR frequencies calculated using M06-2X/6-31+G(2d,2p) (red dashed line). A scaling factor of 0.947 for the M06-2X functional from the NIST database was applied to the calculated IR frequencies.

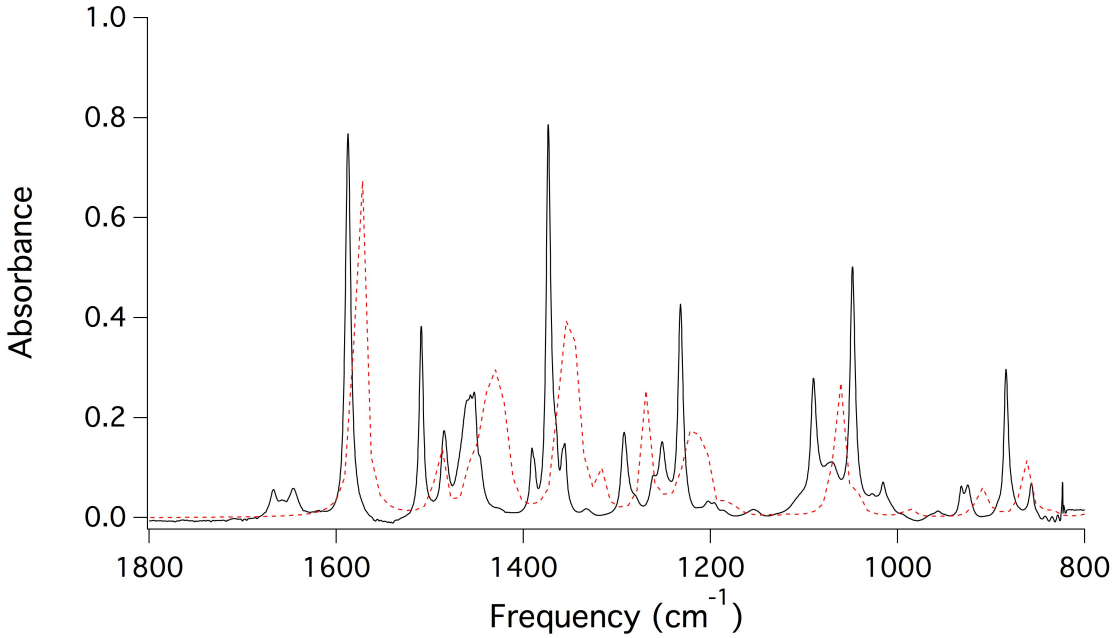

Figure 4.10. Solution IR spectrum of **^{t}Bu$_2$OMeArO$^\bullet$** in CCl_4 (black solid line) and IR frequencies calculated using M06-2X/6-31+G(2d,2p) (red dashed line). A scaling factor of 0.947 for the M06-2X functional from the NIST database was applied to the calculated IR frequencies.

Table 4.5. Selected IR frequencies and assignments calculated using M06-2X with different basis sets and selected experimental IR frequencies.

Basis Set	**Calculated Frequencies (cm^{-1})**				
M06-2X/ 6-31G*	1640	1671.2	1671.4	1711	1031
M06-2X/ 6-31+G**	1633	1663.51	1663.53	1698	1033
M06-2X/ 6-31+G(2d,2p)	1629	1659.68	1659.75	1690	1032
Assignment[a]	C2=C3/C5=C6 asymmetric stretch	Mixed C2=C3/C5=C6/ C1=O1 stretch	Mixed C2=C3/C5=C6/ C1=O1 stretch	C1=O1 asymmetric stretch	C4-C4a symmetric stretch
Experiment[b]	1622, 1632, 1646, 1667				-

[a]From M06-2X calculations. [b]Experimental C=C/C=O IR frequencies have not been explicitly assigned. The C4-C4a stretching frequency may be IR inactive.

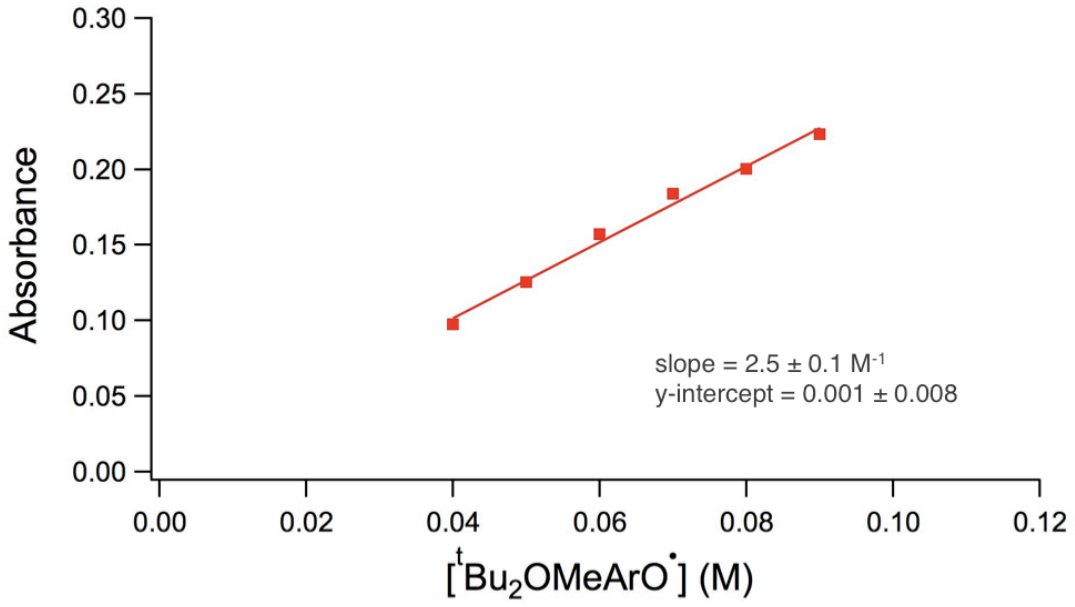

Figure 4.11. Beer's Law plot of **^{t}Bu$_2$OMeArO$^\bullet$** absorbance at 1292 cm^{-1}.

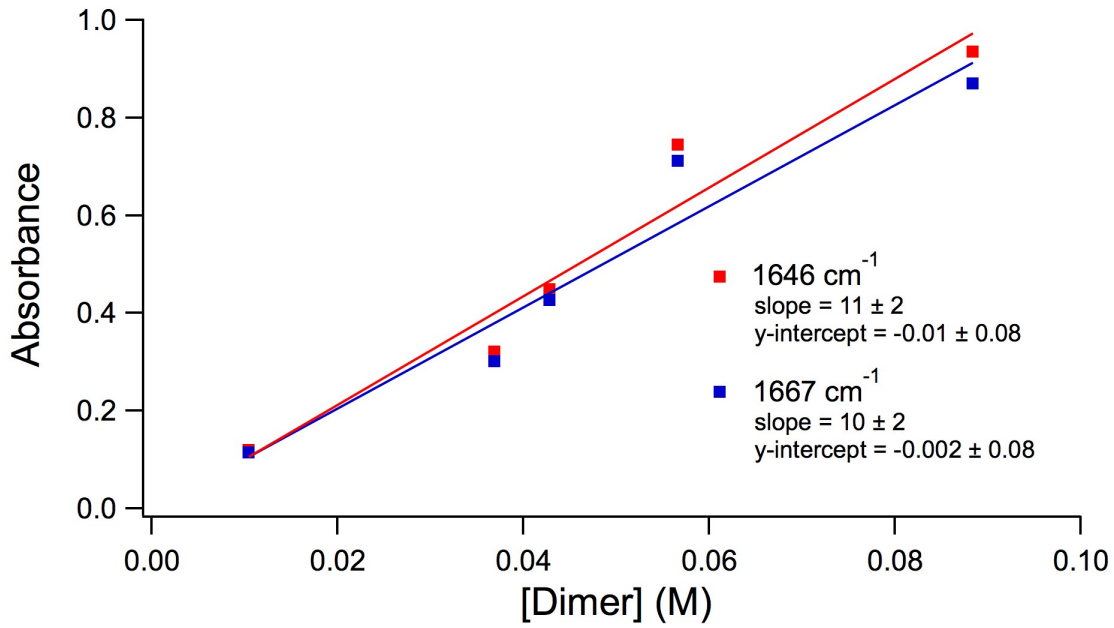

Figure 4.12. Beer's Law plot of dimer absorbance at 1646 cm^{-1} and 1667 cm^{-1}.

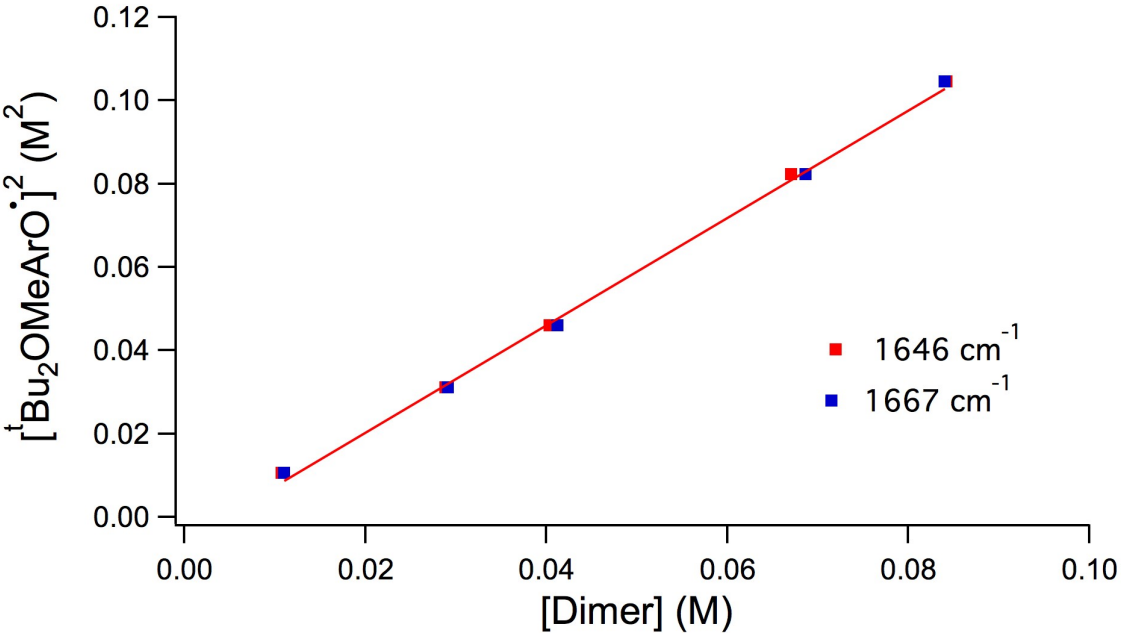

Figure 4.13 Plot of [^{t}**Bu$_2$OMeArO$^{\bullet}$**]^2 vs. [dimer].

4.5.5 DFT Calculations. All calculations were performed using Gaussian 09, Revision A.02.[16]Calculations were performed using the M06-2X functional and 6-31G*, 6-31+G**, and 6-31+G(2d,2p) basis sets.[16]

Table 4.6. Optimized geometry of dimer in Cartesian coordinates (M06-2X/6-31+G(2d,2p)).

Center Label	Atomic Number	Coordinates (Å)		
		X	Y	Z
O1	8	4.25002	-0.00001	-0.87194
O2	8	-0.40544	0.00002	1.74447
C1	6	3.21538	-0.00001	-0.23487
C2	6	2.57273	-1.29105	0.18852
C3	6	1.3083	-1.24731	0.6149
H3	1	0.78088	-2.14233	0.92753
C4	6	0.48024	0	0.64387
C5	6	1.3083	1.24731	0.61488
H5	1	0.78089	2.14233	0.92749
C6	6	2.57274	1.29104	0.18851
C7	6	3.37588	2.58332	0.07654
C8	6	2.60526	3.76234	0.67943
H8A	1	1.67548	3.96098	0.13875
H8B	1	3.22108	4.6623	0.61662
H8C	1	2.36548	3.59284	1.73316
C9	6	3.64458	2.89968	-1.40623
H9A	1	2.70107	2.99124	-1.9519
H9B	1	4.24578	2.12374	-1.87613
H9C	1	4.1765	3.85249	-1.48288
C10	6	4.70618	2.44818	0.8373
H10A	1	5.25475	3.39231	0.78271
H10B	1	5.33172	1.66368	0.41451
H10C	1	4.52476	2.22468	1.89257
C11	6	3.37586	-2.58334	0.07653
C12	6	3.64454	-2.89968	-1.40625
H12A	1	2.70104	-2.99121	-1.95191
H12B	1	4.17645	-3.8525	-1.48292
H12C	1	4.24576	-2.12374	-1.87614
C13	6	4.70616	-2.44823	0.83728
H13A	1	5.3317	-1.66372	0.41451

H13B	1	5.25473	-3.39236	0.78266
H13C	1	4.52474	-2.22476	1.89257
C14	6	2.60522	-3.76237	0.6794
H14A	1	2.36543	-3.59287	1.73313
H14B	1	3.22105	-4.66232	0.61659
H14C	1	1.67545	-3.961	0.13871
C15	6	0.22967	-0.00004	3.00662
H15A	1	0.85303	-0.89062	3.14291
H15B	1	-0.56529	0.00018	3.75061
H15C	1	0.85341	0.8903	3.14281
O1a	8	-4.25004	0.00002	0.87195
O2a	8	0.40543	-0.00004	-1.74446
C1a	6	-3.21538	0.00001	0.23489
C2a	6	-2.57273	1.29105	-0.18851
C3a	6	-1.3083	1.2473	-0.6149
H3a	1	-0.78089	2.14232	-0.92753
C4a	6	-0.48025	-0.00001	-0.64386
C5a	6	-1.30832	-1.24732	-0.61487
H5a	1	-0.78091	-2.14234	-0.92748
C6a	6	-2.57276	-1.29104	-0.1885
C7a	6	-3.3759	-2.58333	-0.07653
C8a	6	-2.60525	-3.76234	-0.67943
H8Aa	1	-1.67547	-3.96096	-0.13875
H8Ba	1	-3.22107	-4.6623	-0.61662
H8Ca	1	-2.36548	-3.59282	-1.73316
C9a	6	-3.64459	-2.8997	1.40623
H9Aa	1	-2.70108	-2.99125	1.9519
H9Ba	1	-4.24581	-2.12378	1.87614
H9Ca	1	-4.1765	-3.85252	1.48287
C10a	6	-4.70619	-2.4482	-0.8373
H10Aa	1	-5.25475	-3.39234	-0.78273
H10Ba	1	-5.33175	-1.66372	-0.4145
H10Ca	1	-4.52476	-2.22468	-1.89257
C11a	6	-3.37585	2.58335	-0.07654
C12a	6	-3.6445	2.89975	1.40623
H12Aa	1	-2.70098	2.99125	1.95188
H12Ba	1	-4.17636	3.85259	1.48288
H12Ca	1	-4.24574	2.12385	1.87616
C13a	6	-4.70616	2.44825	-0.83728
H13Aa	1	-5.33173	1.66379	-0.41447
H13Ba	1	-5.2547	3.39241	-0.78269
H13Ca	1	-4.52476	2.22474	-1.89255
C14a	6	-2.60519	3.76234	-0.67946

H14Aa	1	-2.36543	3.59282	-1.73318
H14Ba	1	-3.22098	4.66232	-0.61665
H14Ca	1	-1.6754	3.96095	-0.13879
C15a	6	-0.22968	0.00002	-3.00661
H15Aa	1	-0.85305	0.8906	-3.14291
H15Ba	1	0.56528	-0.00019	-3.7506
H15Ca	1	-0.85342	-0.89032	-3.1428

Table 4.7. Optimized geometry of monomer in Cartesian coordinates (M06-2X/6-31+G(2d,2p)).

Center Label	**Atomic Number**	**Coordinates (Å)**		
		X	**Y**	**Z**
C1	6	-0.22514	-0.81255	-0.00001
C2	6	1.15377	-0.30234	0
C3	6	1.36616	1.05896	-0.00002
C4	6	0.28518	1.95296	-0.00003
C5	6	-1.04741	1.48916	-0.00002
C6	6	-1.33839	0.15373	0.00001
C7	6	2.31589	-1.29151	0.00001
H3	1	2.37222	1.44863	-0.00002
O2	8	0.4182	3.28885	-0.00005
H5	1	-1.81996	2.24629	-0.00002
C11	6	-2.77474	-0.35992	0.00003
O1	8	-0.44776	-2.03627	0.00004
C8	6	3.67221	-0.57706	-0.00002
C9	6	2.25084	-2.17376	1.26147
C10	6	2.25082	-2.17382	-1.2614
H9A	1	3.10709	-2.85415	1.27
H9B	1	2.3002	-1.55736	2.16348
H9C	1	1.33529	-2.76075	1.285
H8A	1	4.46691	-1.32648	0.00001
H8B	1	3.80627	0.04577	-0.88912
H8C	1	3.80628	0.04584	0.88904
H10A	1	3.10706	-2.85422	-1.26991
H10B	1	1.33526	-2.76081	-1.28488
H10C	1	2.30016	-1.55747	-2.16344
C12	6	-3.02637	-1.20775	1.26124
C13	6	-3.78494	0.79197	0.00001

C14	6	-3.02639	-1.20781	-1.26113
H12A	1	-4.06842	-1.54023	1.27063
H12B	1	-2.37953	-2.08242	1.28633
H12C	1	-2.854	-0.61356	2.16318
H13A	1	-4.79539	0.37698	0.00004
H13B	1	-3.68494	1.42178	0.88823
H13C	1	-3.68497	1.42173	-0.88825
H14A	1	-4.06844	-1.5403	-1.27049
H14B	1	-2.85404	-0.61366	-2.1631
H14C	1	-2.37955	-2.08247	-1.2862
C15	6	1.7213	3.84396	-0.00014
H15A	1	1.58427	4.9224	-0.00022
H15B	1	2.27396	3.54432	0.89412
H15C	1	2.27389	3.54417	-0.89441

4.5.6 Badger's Rule and Bond Length/Bond Strength Correlations. Badger's rule relates bond lengths to force constants according to equation 1,

$$r_e = (C_{ij}/k_e)^{\frac{1}{3}} + d_{ij} \tag{4.4}$$

where C_{ij} and d_{ij} are constant for a specific set of i-j bonded atoms.[2] The calculated force constant (k) of the C4-C4a bond in the phenoxyl radical dimer was compared to the force constants of typical C-C bonds in ethane, ethene, ethyne, and benzene (Table 4.2). The bond lengths were plotted versus $k^{-1/3}$ to determine whether the C4-C4a dimer bond follows the same linear relationship proposed by Badger (Equation 4.4) as the C-C bonds in ethane, ethene, ethyne, and benzene (Figure 4.5).[2] The $k^{-1/3}$ values of the C4-C4a dimer bond is in good agreement with the trend predicted by the ethane, ethene, ethyne, and benzene C-C bonds.

4.5.7 Crystallographic Information. A colorless plate, measuring 0.35 x 0.20 x 0.02 mm^3 was mounted on a glass capillary with oil. Data was collected at -173 °C on a Bruker APEX II single crystal X-ray diffractometer, Mo-radiation.

The crystal-to-detector distance was 40 mm and exposure time was 10 seconds per degree for all sets. The scan width was 0.5°. Data collection was 99.9% complete to 25° in ϑ. A total of

46501 (merged) reflections were collected covering the indices, h = -13 to 13, k = -24 to 24, l = -19 to 19. 3524 reflections were symmetry independent and the R_{int} = 0.0480 indicated that the data was good (average quality 0.07). Indexing and unit cell refinement indicated a C - centered monoclinic lattice. The space group was found to be C 2/c (No.15).

The data was integrated and scaled using SAINT, SADABS within the APEX2 software package by Bruker.[28]

Solution by direct methods (SHELXS, SIR97[29]) produced a complete heavy atom phasing model consistent with the proposed structure. The structure was completed by difference Fourier synthesis with SHELXL97.[30,31] Scattering factors are from Waasmair and Kirfel.[32] Hydrogen atoms were placed in geometrically idealised positions and constrained to ride on their parent atoms with C---H distances in the range 0.95-1.00 Angstrom. Isotropic thermal parameters U_{eq} were fixed such that they were $1.2U_{eq}$ of their parent atom Ueq for CH's and $1.5U_{eq}$ of their parent atom U_{eq} in case of methyl groups. All non-hydrogen atoms were refined anisotropically by full-matrix least-squares.

Table 4.8: Crystallographic data.

Empirical formula	C30 H46 O4	
Formula weight	470.67	
Temperature	100(2) K	
Wavelength	0.71073 Å	
Crystal system	Monoclinic	
Space group	C 2/c	
Unit cell dimensions	a = 10.2918(9) Å	α= 90°.
	b = 18.727(2) Å	β= 94.587(4)°.
	c = 14.6697(12) Å	γ = 90°.
Volume	2818.3(5) $Å^3$	
Z	4	
Density (calculated)	1.109 Mg/m^3	
Absorption coefficient	0.071 mm^{-1}	
F(000)	1032	
Crystal size	0.30 x 0.15 x 0.14 mm^3	
Theta range for data collection	2.17 to 28.40°.	
Index ranges	-13<=h<=13, -24<=k<=24, -19<=l<=19	
Reflections collected	46501	
Independent reflections	3524 [R(int) = 0.0480]	
Completeness to theta = 25.00°	99.9 %	
Max. and min. transmission	0.9901 and 0.9789	
Refinement method	Full-matrix least-squares on F^2	
Data / restraints / parameters	3524 / 0 / 161	
Goodness-of-fit on F^2	1.078	
Final R indices [I>2sigma(I)]	R1 = 0.0490, wR2 = 0.1359	
R indices (all data)	R1 = 0.0575, wR2 = 0.1472	
Largest diff. peak and hole	0.567 and -0.301 $e.Å^{-3}$	

Notes to Chapter 4

(1) (a) Zavitsas, A. A. *J. Phys. Chem. A* **2003**, *107*, 897-898. (b) Dames, E.; Sirjean, B.; Wang, H. *J. Phys. Chem. A* **2010**, *114*, 1161-1168.

(2) (a) Badger, R. M. *J. Chem. Phys.* **1934**, *2*, 128-131. (b) Badger, R. M. *J. Chem. Phys.* **1935**, *3*, 710-714. (c) For a recent application, see Green, M. T. *J. Am. Chem. Soc.* **2006**, *128*, 1902–1906.

(3) Pauling, L. *The Nature of the Chemical Bond*; 3d ed.; Cornell University Press: Ithaca, N.Y., 1960.

(4) Brown, I. D.; Shannon, R. D. *Acta Crystallographica Section A* **1973**, *A 29*, 266-282.

(5) Robinson, E. A. L., M. W. *Can. J. Chem.* **1963**, *41*, 2988-2995.

(6) Frenette, M.; Aliaga, C.; Font-Sanchis, E.; Scaiano, J. C. *Org. Lett.* **2004**, *6*, 2579-2582.

(7) .

(8) (5) (a) Collman, J. P.; Decreau, R. A.; Sunderland, C. J. *Chem. Commun*. **2006**, 3894-3896. (b) Schrauben, J. N.; Hayoun, R.; Valdez, C. N.; Braten, M.; Fridley, L.; Mayer, J. M. *Science* **2012**, 336, 1298-1301. (c) Lyons, C. T.; Stack, T. D. P. *Coord. Chem. Rev.* **2013**, 257, 528-540. (d) Lucarini, M.; Pedulli, G. F. *Chem. Soc. Rev.* **2010**, 39, 2106-2119. (e) Markle, T. F.; Tronic, T. A.; DiPasquale, A. G.; Kaminsky, W.; Mayer, J. M. *J. Phys. Chem. A* **2012**, 116, 12249-12259.

(9) Altwicke.Er *Chem. Rev.* **1967**, *67*, 475-&.

(10) Muller, E.; Ley, K. *Chemische Berichte-Recueil* **1955**, *88*, 601-614.

(11) Wittman, J. M. H., R.; Kaminsky, W.; Coggins, M. K.; Mayer, J. M. *J. Am. Chem. Soc.* **2013**, *135*, 12956-12959.

(12) Manner, V. W.; Markle, T. F.; Freudenthal, J. H.; Roth, J. P.; Mayer, J. M. *Chem. Commun.* **2008**, 256-258.

(13) Crystals were grown by Rebecca Hayoun.

(14) X-ray crystallography was performed by Werner Kaminsky and Michael K. Coggins. The X-ray crystal structure was solved by Werner Kaminsky and Michael K. Coggins.

(15) Webster, R. D. *Electrochem. Commun.* **2003**, *5*, 6-11.

(16) Gaussian 09, Revision A.1, M. J. Frisch, G. W. Trucks, H. B. Schlegel, G. E. Scuseria, M. A. Robb, J. R. Cheeseman, G. Scalmani, V. Barone, B. Mennucci, G. A. Petersson, H. Nakatsuji, M. Caricato, X. Li, H. P. Hratchian, A. F. Izmaylov, J. Bloino, G. Zheng, J. L. Sonnenberg, M. Hada, M. Ehara, K. Toyota, R. Fukuda, J. Hasegawa, M. Ishida, T. Nakajima, Y. Honda, O. Kitao, H. Nakai, T. Vreven, J. A. Montgomery, Jr., J. E. Peralta, F. Ogliaro, M. Bearpark, J. J. Heyd, E. Brothers, K. N. Kudin, V. N. Staroverov, R. Kobayashi, J. Normand, K. Raghavachari, A. Rendell, J. C. Burant, S. S. Iyengar, J. Tomasi, M. Cossi, N. Rega, J. M. Millam, M. Klene, J. E. Knox, J. B. Cross, V. Bakken, C. Adamo, J. Jaramillo, R. Gomperts, R. E. Stratmann, O. Yazyev, A. J. Austin, R. Cammi, C. Pomelli, J. W. Ochterski, R. L. Martin, K. Morokuma, V. G. Zakrzewski, G. A. Voth, P. Salvador, J. J. Dannenberg, S. Dapprich, A. D. Daniels, Ö. Farkas, J. B. Foresman, J. V. Ortiz, J. Cioslowski, and D. J. Fox, Gaussian, Inc., Wallingford CT, 2009.

(17) Haynes, W. M. *CRC Handbook of Chemistry and Physics*; 93 ed.; CRC Press: Baco Raton, FL, 2012.
(18) Chen, X. W., X.; Zhou, Z.; Li, Y.; Sui, Y.; Ma, J.; Wang, X.; Power, P. P. *Angew Chem Int Edit* **2013**, *52*, 589-592.
(19) (a) Li, P. C.; Wang, T. S.; Lee, G. H.; Liu, Y. H.; Wang, Y.; Chen, C. T.; Chao, I. *J. Org. Chem.* **2002**, *67*, 8002-8009. (b) Shi, Z. W.; Li, Y. Z.; Li, Y.; Lu, G. Y.; Liu, S. H. *Acta Cryst. E* **2004**, *60*, O2275-O2277. (c) Ehrenber, M. *Acta Cryst.* **1967**, *22*, 482. (d) Mori, Y.; Niwa, A.; Maeda, K. *Acta Crystallogr.* **1995**, *B51*, 61-65. (e) Lam, Y.; Lee, G.-H.; Liang, E. *Bull. Chem. Soc. Jpn.* **2001**, *74*, 1033-1034.
(20) Mahoney, L. R.; Weiner, S. A. *J. Am. Chem. Soc.* **1972**, *94*, 585-&.
(21) (a) Neumann, W. P.; Uzick, W.; Zarkadis, A. K. *J. Am. Chem. Soc.* **1986**, *108*, 3762-3770. (b) Gomberg, M. *Chem. Rev.* **1924**, *1*, 91-141.
(22) (a) Zaitsev, V.; Rosokha, S. V.; Head-Gordon, M.; Kochi, J. K. *J. Org. Chem.* **2006**, 71, 520-526. (b) Small, D.; Rosokha, S. V.; Kochi, J. K.; Head-Gordon, M. *J. Phys. Chem. A* **2005**, 109, 11261-11267.
(23) (a) Dugan, T. R.; Bill, E.; MacLeod, K. C.; Christian, G. J.; Cowley, R. E.; Brennessel, W. W.; Ye, S.; Neese, F.; Holland, P. L. *J. Am. Chem. Soc.* **2012**, *134*, 20352-20364. (b) See also Frazier, B. A.; Wolczanski, P. T.; Lobkovsky, E. B.; Cundari, T. R. *J. Am. Chem. Soc.* **2009**, *131*, 3428-3429.
(24) Colle, T. H. L., E. S. *J. Am. Chem. Soc.* **1979**, *101*, 1810-1814.
(25) Kaupp, M.; Metz, B.; Stoll, H. *Angewandte Chemie-International Edition* **2000**, *39*, 4607.
(26) (a) Sanderson, R. T. *Chemical Bonds and Bond Energy*; 2d ed.; Academic Press: New York, 1976. (b) Cremer, D.; Wu, A. N.; Larsson, A.; Kraka, E. *Journal of Molecular Modeling* **2000**, *6*, 396-412.
(27) Related DFT studies of phenoxyl radical dimerizations have used the B3LYP funcitional,30a,b but in this system the M06-2X functional provided much better agreement with experiment. (a) Asatryan, R.; Davtyan, A.; Khachatryan, L.; Dellinger, B. *J. Phys. Chem. A* **2005**, *109*, 11198-11205. (b) Sangha, A. K.; Parks, J. M.; Standaert, R. F.; Ziebell, A.; Davis, M.; Smith, J. C. *J. Phys. Chem. B* **2012**, *116*, 4760-4768.
(28) Bruker (2007) APEX2 (Version 2.1-4), SAINT (version 7.34A), SADABS (version 2007/4), BrukerAXS Inc, Madison, Wisconsin, USA.
(29) (a) Altomare, A.; Burla, C.; Camalli M.; Cascarano L.; Giacovazzo C.; Guagliardi A.; Moliterni A.G.G.; Polidori G.; Spagna R. *J. Appl. Cryst.* **1999**, 32, 115-119; (b) Altomare, A., Cascarano, G., Giacovazzo, C., Guagliardi, A., *J. Appl. Cryst.* **1993**, 26, 343.
(30) Sheldrick, G. M. SHELXL-97: Program for the Refinement of Crystal Structures 1997 University of Gottingen, Germany.
(31) Mackay, S.; Edwards, C.; Henderson, A.; Gilmore, C.; Stewart, N.; Shankland, K.; Donald, A.; MaXus: a computer program for the solution and refinement of crystal structures from diffraction data. University of Glasgow, Scotland, 1997.
(32) Waasmaier, D.; Kirfel, A. *Acta Crystallographica Section A* **1995**, *51*, 416-431.

VITA

Jessica Wittman was born in Bozeman, MT and grew up in Helena, MT. She received her B.S. in Chemistry from Montana State University in Bozeman where she worked on bioinorganic undergraduate research projects with Prof. Robert Szilagyi and Prof. Trevor Douglas. She then moved to the University of Washington for grad school and joined the group of Prof. Jim Mayer. After finishing her PhD, she will begin teaching chemistry at community colleges in the Seattle area.